Improving Charge Separation and Transfer in Semiconducting Nanocrystalline Materials

By

Madeleine J Fort

Submitted to the Faculty of the

Graduate School of Vanderbilt University

for the degree of

DOCTOR OF PHILOSOPHY

in

Interdisciplinary Materials Science

May 12th, 2023

Nashville, Tennessee

Approved:

Janet Macdonald, Ph.D.

Piran Kidambi, Ph.D.

Sandra Rosenthal, Ph.D.

Timothy Hanusa, Ph.D.

Gregory Walker, Ph.D.

Dedication

To my wonderful family and friends, thank you for the world.

Acknowledgements

The work of this thesis was financially supported by the Department of Chemistry at Vanderbilt University, National Science Foundation, and the Vanderbilt Institute of Nanoscale Science and Engineering. Portions of this work were funded by the TNSCORE NSF EPS 1004083 and the Australian Research Council Discovery Project DP190103158.

First thanks must go to Dr. Janet Macdonald. She welcomed me into her group, encouraged me to keep going when the science felt impossible, and educated me in the ways of chemistry. The last few years have been hard on all of us; thank you for steering us through the rapids and teaching us how to paddle. Your boundless curiosity for your field and courage have been a great source of inspiration. I am privileged to have been able to work in your lab. I must also thank Dr. Piran Kidambi, Dr. Timothy Hanusa, Dr. Sandra Rosenthal, and Dr. Greg Walker for serving on my committee and their support over the years.

To my other members of the Macdonald Lab, past and present, you have all been incredible. Emil and Andrew, thank you for helping an engineer let loose in a chemistry lab. Jordan, you taught me how to use a Schlenk line and were an incredible mentor. Evan, thank you for starting all this crazy cobalt stuff. Nathan and Chris, it has been an honor. I can't imagine having gone through this whole grad school thing with anyone else. Danielle, you are an incredible chemist and friend, I'm so glad you joined us. Jeremy, you amaze me with your command over iron sulfides. Lexie, you astound me with the complexities of what you unravel. Andrey, you have done and will do amazing things. Let's go climbing sometime. Tony, it's been a blast (too literally), but you may need to slow down so the rest of us don't look bad. Pete, you are doing great work; you know you're allowed to sleep? Emma, I can't wait to see what incredible things you do.

Dr. Keri Tallman and Dr. James Mcbride, there have been many times when, stymied by a synthesis or struggling to use the TEM, you have answered my prayers. I can't imagine having tried to do science in your absence. My most heartfelt thanks for the hours you put into helping those around you.

I would like to extend thanks to a select few persons from my undergraduate institution. Dr. Rebecca Christianson, thank you for showing me how incredible materials could be. Dr. Diana Dabby, thank you for never giving up on me. I wouldn't have made it through condensed matter without you. Dr. Rehana Patel, thank you for telling me I should probably go to grad school. Dr. Maruta Vitols, thank you for reminding me to laugh sometimes. Most importantly, thank you to Dr. Sherra Kerns, without you I would never have found materials or gone to Vanderbilt. At the crux of my career in STEM, I found you, and am

so grateful for it. Other mentors mentions must include Ms. Catron, Ms. Pretz, and Jay. The three of you kept me asking questions and gave me the joy of science.

Alex, Holiday, Seb, Henry, MK, and Clint, you are all such amazing friends. The last nine years we may have lived far apart from each other, but you are the closest friends I could ever have. Matt and Kelly, you are incredible friends. You have made this grad school experience so much better. Tonnar, I don't know if I could have done this last year without you. If anyone was ever meant to get a PhD, it's you. Joe and Gina, truly the universe smiled upon me meeting Eric midway up a juniper tree when I was five. Your support, kindness, and example have carried me through many rough patches and brought so much love and laughter. Eric, few people find a brother at the ripe age of five, thank you for two decades of camaraderie, even if it does include getting yelled at about pigeons.

Mom and Dad, I can't believe that through some chance of grace or fortune I have parents as wonderful as you. There is no way to adequately acknowledge the sacrifices you made to get me here and the level of support you have given me. Jury is still out on if I wouldn't rather go into art, architecture, or history, but the knowledge that you would support me has kept me going through some of the darker times. I love you so much, thank you for giving me unconditional love and support. Though they are not with us, thank you Grandma Marilyn, Grandpa Howard, and Grandma Ruth. I hope I made you proud. Apollo, I'll see you in the window again someday.

Chapter 1

Introduction

1.1 Powering the Planet

Current population and economic growth demand a rapid increase in the amount of produced energy per year. It is expected that we will need 27TW by 2050 and 43TW by 2100.[2–4] There are few routes to generating the amount of power necessary to meet energy needs, and even fewer in a carbon-neutral manner. One of these routes may be nuclear fission, but it is undesirable for several reasons. Uranium resources are sufficient to produce only 100TW of electricity. If 10TW-yr of electricity were produced using nuclear fission of uranium, global supplies of uranium would run out within the first decade of usage. Not only would uranium used at this rate be useful for less than ten years, but uranium sources would be depleted during most of the ramp up to producing enough reactors to generate 10TW per year.[2] Fossil fuels can support a 25-30TW/yr for at least several centuries, but not in an economically feasible way and not in a way that avoids climate catastrophe.[3]

The sunlight that strikes the earth in one hour is more energy than was consumed in all of 2001 (4.3×10^{20}J vs 4.1×10^{20}J).[2] The failure to exploit the solar system's largest nuclear reactor at this point is largely due to a lack of inexpensive solar cells, a fledgling understanding of solar-to-fuel catalysis, and a dearth of ways to store that energy.[3,5] The cost of silicon solar cells has dropped precipitously in the past two decades.[6–8] Advances in battery technologies have made electric vehicles a reality and may lead to large-scale storage capacity.[9] To take full advantage of solar energy's potential, however, the need for solar cells that are cheaper, lighter, flexible, more aesthetically pleasing, and with higher efficiencies remains.[10]

1.2 Colloidal Nanoparticles and Quantum Dots

The advent of semiconductors has fundamentally altered the world. Every feature of modern life has been touched by the computing revolution.[11] For the great majority of semiconductor usage, it is appropriate to think of these semiconductors as a bulk, large-scale, material. Even the tiny computer chips now used would be considered a bulk material (although the transistors that make up the actual computing aspect certainly cannot be). The desire to pack more transistors into a

wafer combined with the continuing discoveries of quantum physics led to the nano-revolution. What the nano-revolution demonstrated was the existence of a special set of rules governing objects based on their size. Phenomena such as superparamagnetism and surface plasmon resonance evolving from the quantum mechanical coupling of several hundred to several thousand atoms were observed for the first time at the nanoscale.[12]

In bulk semiconductors, the electrical and optical properties are governed by composition, crystal structure, and dopants, following the rule of "form is function".[13] An extension of this rule is seen in quantum confinement. Quantum confinement arises when a charge carrier is constrained to a body with a length scale similar to the de Broglie wavelength.[14] This is more often thought of in terms of the Bohr exciton radius of the material. Quantum confinement is observed when a semiconductor crystal is made with a dimension on the length scale of two times the Bohr exciton radius or less. Quantum confinement may also be thought of as constraining the electron to a region comparable to the de Broglie wavelength of the electron in that material.[14] Quantum confined structures are defined by how many dimensions can have a freely moving electrons. These may include quantum wells, wires, and dots (2D, 1D, and 0D respectively). Quantum dots (QDs) have a severely discretized density of states (DOS) that begins to appear molecular in nature. The degree of confinement is controlled by whether the crystal is smaller than neither radius, one charge carrier radius, or both radii. Each of these regimes has different photophysical characteristics.[15] Cadmium selenide (CdSe) QDs are considered to be strongly confined, having the radius of the dots smaller than the Bohr radii of both electron and hole charge carriers.

As the dots become smaller, the increased confinement leads to a larger bandgap and a commiserate blue shifting of the emission and absorption of these dots. This shift is principally seen in the conduction band of the QD due to the larger electron Bohr radius.[16] Many QDs are made of core-shell structures. The shell structures will passivate surface defects and localize one or both charge carriers to the core. Type I QDs, such as CdSe/ZnS, localize both charge carriers to the core. Type II, such as CdTe/CdSe, QDs will localize one charge carrier to the core.[17]

1.3 Solar Cell Efficiencies

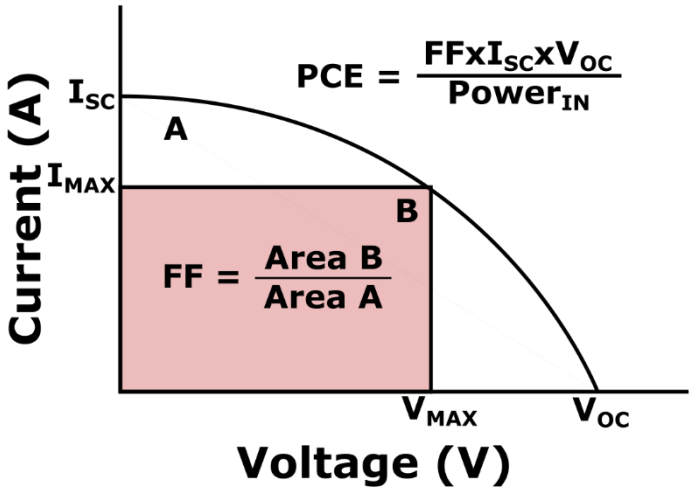

Figure 1.1: An example IV curve. The fill factor (FF) is shown as the red area B divided by the total area inside the curve (A). Area B is defined as the largest square able to fit under the curve.

Solar cell efficiency is determined by the ratio of harvested energy over input power. This can be calculated by using an IV curve such as that seen in Figure 1.1. The amount of power and the spectrum of that power is standardized, usually to mimic solar radiation. AM 1.5 is the standard spectrum filter for solar radiation. Solar cell efficiency is calculated by using the following equation:

$$\eta = \frac{V_{OC} I_{SC} FF}{P_{IN}} \tag{1.1}$$

where V_{OC} is the open circuit voltage, I_{SC} is the short circuit current, FF is the fill factor, P_{IN} is the input power, and η is efficiency. P_{IN} is usually standardized at 100mW/cm^2, and all other values can be observed from an I-V curve. On an IV curve such as that shown in Figure 1.1, I_{SC} is the maximum current at zero voltage, V_{OC} is the maximum voltage at zero current, and fill factor is the relative squareness of the curve.

1.3 The Scope of this Dissertation

The focus of this dissertation is to examine the underlying materials science of nanocrystalline semiconducting materials, particularly in relation to the separation and transfer of charge. Chapter 2 discusses some of the applications of the quantum dot. An understanding of Marcus theory is developed and the concept of Auger-assisted transfer is introduced. The history of dye sensitized solar cells and recent developments in the electrolyte are explained. It is shown that for all the advancement in this technology, the hole extraction rate is still lagging behind the electron extraction rate by as much as six orders of magnitude. A brief overview of hydrogen production by water splitting is given where the slow extraction of the hole (three to four orders of magnitude) is introduced. Chapter 3 discusses the effect of reorganization energy on electron transfer rates from quantum dots. A framework in Marcus theory is developed to demonstrate why transfer processes are so dependent upon the reorganization energy of the acceptor. Chapter 4 provides a detailed look into the history of the field of pyrite photovoltaics and attempts to understand the poor performance observed. The underlying chemistry of the system is examined to further determine if there is a route to better performance. Lastly, the use of pyrite in dye sensitized solar cells and batteries is explored. Chapter 5 addresses the attempts at understanding the surface via surface treatments with unsymmetric ligands and exciton-delocalizing ligands. Preliminary results suggest that the effects of this treatment are unclear, and indicate that the means to measure these effects are beyond the capabilities available. The use of pyrite in high temperature batteries is briefly discussed and the mode and temperature of the phase transition accompanying this use is shown via heated in-situ x-ray diffraction.

Chapter 2

Applications and Background of Charge Transfer

2.1 Quantum Dots and Charge Extraction

Quantum dots (QDs) and other colloidal quantum confined semiconductors have been the subjects of extensive research and numerous applications since their discovery. Their varied uses include bioimaging and sensing, solar cells, solar concentrators, displays, lighting, lasing, quantum information, and photocatalysis to name but a few.[13,14,18–33] The popularity of QDs is due in large part to the narrow linewidths, bright emissions, tunable Stokes shift, functionalizable surface chemistry, and ease of altering charge transport properties.[14,29,34] QDs were synthesized, and continue to be synthesized, by colloidal methods.[35,36] Recent developments allow for the synthesis of quantum dots via molecular beam epitaxy (MBE) and metal organic chemical vapor deposition (MOCVD).[37,38] The desire to make brighter, more stable, and non-blinking dots has been a major impetus towards improved colloidal chemistry.[39–47]

Nearly all solar energy harvesting strategies rely on the separation and extraction of charge carriers. In order to extract charge, either an electron or a hole must be transferred from the absorbing medium. This process is effectively completing a circuit or doing both halves of a redox reaction. Bulk transfer occurs between a donor and acceptor that are in spatially delocalized systems with a continuum of states (bands). Molecular charge transfer models assume that the donor and acceptor electronic states that are discretized and localized in space (molecular orbitals). Marcus theory has so far been applicable in many nanoparticulate systems; there is evidence, however, that strongly confined systems undergo a different process. Due to the intermediate density of states, there is evidence that QDs and other nanoparticles follow neither molecular nor bulk charge transfer models.

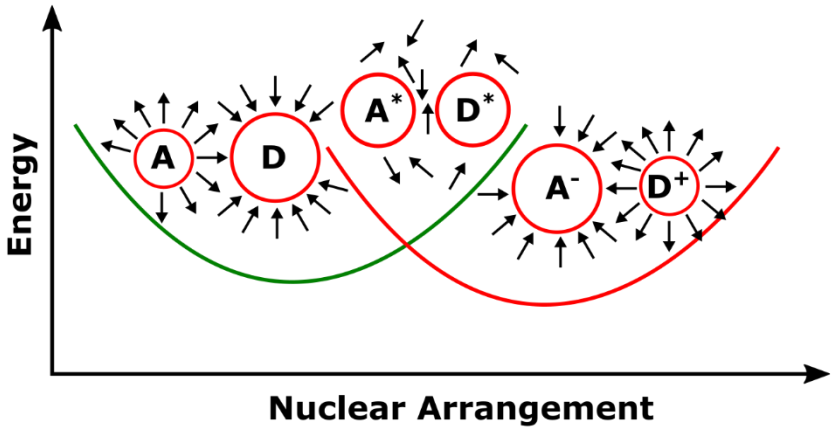

Figure 2.1: Marcus theory of charge transfer. The parabolas represent the potential energy surface for when the electron is on the donor (green) and when it moves to the acceptor (red) and arrows representing the dipole moment in the surrounding solvent. The nuclear arrangement coordinate includes the inner sphere (rearrangement within the donor and acceptor molecules) and outer sphere (solvent).

For the sake of simplicity, the following will be described for electron transfer. In the two state Marcus model, it is understood that electron transfer is much faster than nuclear fluctuations. This effectively means that the electron cannot relax unless it transfers when the donor and acceptor are isoenergetic.[48–51] This relaxation occurs where the curves cross in Figure 2.1. The nuclear coordinate encompasses both the inner sphere reorganization of both the donor and acceptor as well as the outer sphere reorganization of the solvent dipoles. The energetic requirement for this process is the reorganization energy and shown as λ.

The thermodynamic driving force ($-\Delta G_0$) of the reaction can be understood as the potential difference in states between the donor and acceptor. The case shown in Figure 2.1 would be a small driving force. If the minima of the two parabolas were the same energy, the driving force would be zero. As the driving force is increased, rate of electron transfer is increased. The regime where the increasing the driving rate leads to an increase in transfer is called the normal region and it is defined as where $-\Delta G_0 < \lambda$. This region is visible in Figure 2,1 where the red parabola crosses the green to the right of the minima. As $-\Delta G_0$ increases, the right-hand parabola drops increasing the rate of transfer rapidly. When $-\Delta G_0 = \lambda$, the transfer occurs at its fastest and is called the barrierless region. This occurs where the red parabola crosses the green at the minima of the green parabola.

As further increases in the driving force occur ($-\Delta G_0 > \lambda$), the rate of transfer slows. This may be understood as the red parabola crossing the green further to the left than the minima. Further explanation of Marcus theory and its implications may be found in chapter 3.

Marcus theory accurately describes charge transfer for molecules, but struggles in the case of QDs and potentially other nanoparticles. Recent studies have found that in certain cases, it is possible that instead of following Marcus theory, transfer from nanoparticles instead follows Auger assisted charge transfer.[52–54] Auger assisted transfer occurs excess energy is used to promote a hole further into the valence band upon electron transfer instead of going into molecular vibrations.

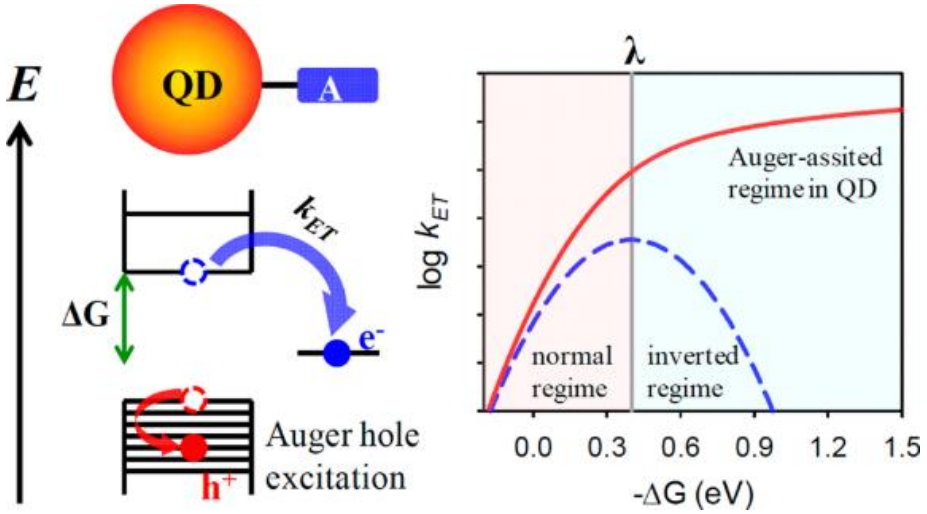

Figure 2.2: Auger assisted charge transfer from quantum dots to a molecular acceptor. The energetic diagram shown on the left shows the transfer of the electron to the acceptor and the driving force of the reaction with a concomitant promotion of the hole to a lower energy. The right shows the electron transfer rate as a function of driving force in the case of Marcus transfer and in the Auger-assisted regime.

The possibility of Auger-assisted transfer opens new possibility to the designers of charge transfer systems. It is possible to tune the reorganization energy of the acceptor without fear of entering the inverted region and dampening charge transfer. Auger-assisted transfer is a significant departure from Marcus transfer too because it is possible to reach many orders of magnitude increased transfer rates as indicated in Figure 2.2.

2.2 Dye Sensitized Solar Cells

Dye-sensitized solar cells (DSSCs) represent an attractive alternative to traditional photovoltaics. They have the potential to be inexpensive to produce. Cell production can be performed with non-toxic naturally occurring materials such as plant dyes. While synthetic metal-based dyes have so far had the highest level of efficiency, cells are often made using the dye molecules from blackberry juice, grape skin, rosella (a relative of the hibiscus plant), and many natural substances.[55–57] By replacing glass electrodes with metal sheets or polymers, it is possible to make flexible cells in a roll-to-roll fashion, making the prospect of printable solar cells a reality.[58,59] These cells have a high tunability and perform well in low-light conditions.[60] The functionality in low light situations is an answer to the "cloudy day" concern over utilization of solar power. Additionally, DSSCs potentially could operate indoors, a necessity in the "internet of things" era. Compared with traditional silicon cells, there is less of a dependence on the ambient temperature.[61] In silicon solar cells, the silicon is both the source of photoelectrons and the material through which separated charges travel. In DSSCs, the semiconductor and dye are separate from each other as visible in Figure 2.3. The wider bandgap TiO_2 acts only as a charge transporter for electrons injected from the dye as well as creating a one-directional junction such that holes cannot be transferred to the TiO_2. This difference permits DSSC efficiency to be less temperature-reliant; carrier concentration within the semiconductor is less critical and the cells have higher recombination rates.[62,63] DSSCs have been shown to have only negligible drops in efficiency between 20°C and 50°C.[64] Accelerated tests showed that after 1000 hours under thermal stress at 80°C in the dark and light soaking at 60°C there was inconsequential device degradation.[65] Furthermore, DSSCs are less dependent on the incident light angle than crystalline silicon cells meaning it is possible to avoid expensive actuated solar farms. This allows them to fill a niche left by traditional photovoltaics and provide a more stable power output over the course of a day. The transparency and color can be tuned which opens the possibility of including DSSCs in a more aesthetically pleasing manner for building integrated photovoltaics. The integration most looked forward to at this time is the replacement of normal window glass.[61]

The first DSSC used chlorophyll extracted from spinach as the dye.[63,66] At the time, zinc oxide was the wide bandgap semiconductor of choice. Improvements in porosity was necessary to improve efficiency upwards of 1% as device architecture moved away from a monolayer of dye molecules. This led to the development of nanoporous titanium dioxide (TiO2) and 7% efficiency. This cell, also known as the Grätzel cell for its inventor, was first developed in 1988 but didn't reach

7% efficiency until 1991.[60] Since that time, research into the DSSC has grown exponentially. Even early cells showed traits distinctive of DSSCs with a higher efficiency in diffuse simulated daylight and high stability lasting higher than five million turnovers.[60] Very rapidly, Grätzel and coworkers pushed efficiencies to 10%. Interest has grown exponentially. In 2014, 2500 articles were published on DSSCs, including 55 on aqueous DSSCs.[67] The recent push into aqueous DSSCs, which have efficiencies upwards of 5.64%, makes lower an already minimal toxicity cell. Additionally, this makes the fouling of the cell by water less of an immediate concern to the outdoor stability of these cells. In relation to Chapter 3, most of these stable aqueous cells use [Co(bipy)$_3$] as a redox mediator.[67,68]

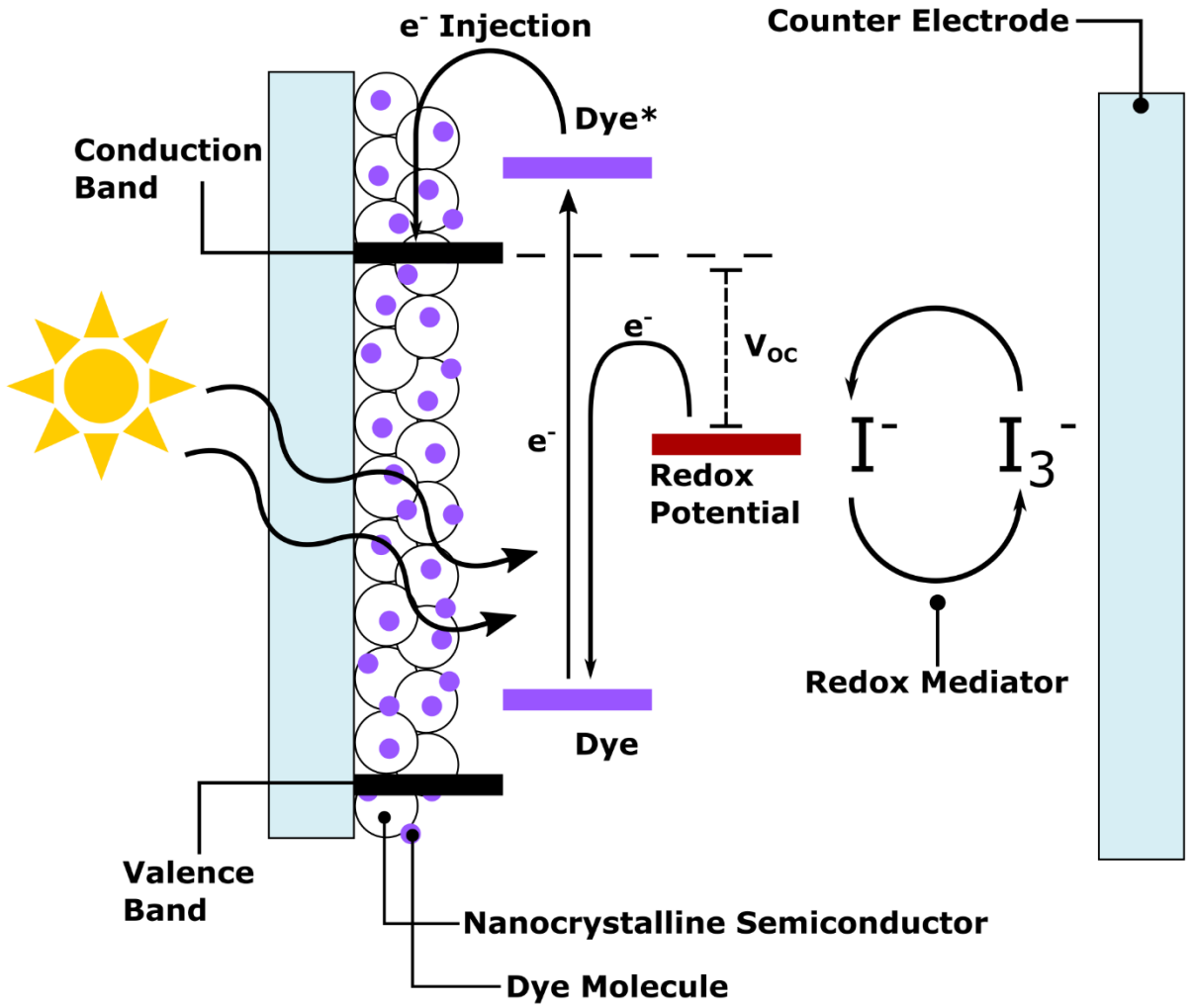

Figure 2.3: DSSC structure and electron transfer diagram.

Traditional electrolytes usually involve a redox couple dissolved in an organic solvent, although solid electrolytes are also being developed.[69] Redox shuttles operate to transfer electrons from the counter electrode back to the dye, completing the electrochemical circuit. There are several constraints on the redox shuttles in order for the cell to function properly. The shuttle must be able to reduce the dye cation prior to recombination of the dye hole with electrons in the photoanode. Additionally, the oxidized shuttle must be prevented from intercepting electrons from

the photoanode. Satisfying both criteria has made the identification of potentially effective redox shuttles very difficult.

It has become increasingly apparent that the nature of the electrolyte is paramount importance to modern cells. The most common electrolyte is the iodide/tri-iodide couple (I^-/I_3^-). As of 2008, all of the DSSCs made with an efficiency higher than 4% used a (I^-/I_3^-) redox shuttle.[70] This couple has its advantages, yet the drawbacks are numerous. The reduction potential of this couple is low enough that more than half a volt is often lost. In addition, the iodide couple is often corrosive towards the electrodes, decreasing the effective lifetime from one to five years down to a matter of hours.[59] Many alternative electrolytes have been developed including $(SCN)_2/SCN^-$, $(SeCN)_3/SeCN^-$, Br^-/Br_3^-, sulphur-based systems, copper complexes, ferrocene derivatives, nitroxide radicals, ruthenium complexes, and cobalt complexes.

The largest step forward in the use of cobalt redox mediators came from the development of Yella's 12% efficiency DSSC. Yella et al. used cobalt trisbipyridylcobalt$[Co(bipy)_3]^{3/2+}$ as the redox mediator and produced higher efficiencies than the iodide couple in the same system. It was theorized that a large reason why the efficiency was limited to 12% came from the internal reorganization energy of the $[Co(bipy)_3]^{3/2+}$.[71] $[Co(bipy)_3]^{3/2+}$ was theorized to suffer from high reorganization energy due to low-spin to high spin transition that occurs upon going from Co(III) to Co(II). Highly labile complexes with weak ligand fields are in a high spin state. $[Co(bipy)_3]^{3/2+}$ has a slow electron self-exchange rate $\sim 10 M^{-1}s^{-1}$ indicative of an internal reorganization energy ~1.8eV derivable from the Equation 3.2. $[Co(bipy)_3]^{3/2+}$ has suffered issues of stability regarding its own lifetime and originally corrosion of electrodes.[72,73]

Strategies to exploit lower reorganization energy complexes, specifically designed not to go through a spin transition have met with some success.[71] An unoptimized cell made with cobalt bis(trithiacyclononane) $[Co(ttcn)_2]^{3+/2+}$ saw comparable efficiency to $[Co(bipy)_3]^{3/2+}$. The reorganization energy of this complex is comparable to the $[Co(ClMeN_3S_3sar)]^{3/2+}$ that was the subject of work from chapter 3.

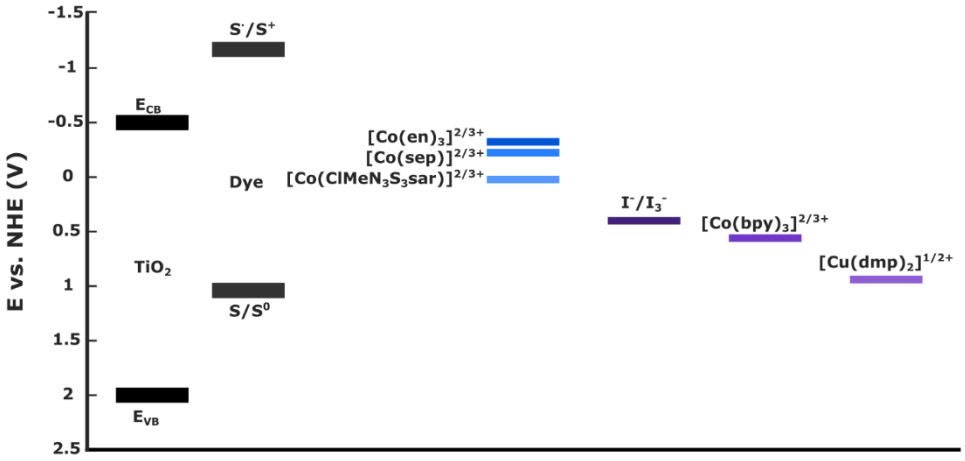

Figure 2.4: Potentials of the valence and conduction bands of TiO_2, excited and ground states of a standard dye, and the redox potentials of three of the most used redox mediators in purple. The redox potentials in blue are those used in chapter 3.

$[Co(bipy)_3]^{3/2+}$ is far from the only metal complex employed as an electrolyte. Copper based complexes are recently being used, in large part due to their appropriate reduction potentials and often a lack of spin-state changes. The most prevalently found in literature of these copper complexes is bis(2,9-dimethy-1,10-phenanthroline) copper ($[Cu(dmp)_2]^{1/2+}$which has been shown to yield moderate efficiencies in a liquid cell DSSC. In a solid-state cell, $[Cu(dmp)_2]^{1/2+}$ was even shown to have a PCE of 8.2% under full sun irradiance.[74] Further developments of copper electrolytes have led to an extraordinary 11% efficiency for solid state cells using the copper electrolyte Cu(4,4',6,6'-tetramethyl-2,2'-bipyridine)$_2$(bis(trifluoromethylsulfonyl)imide)] ($[Cu(tmby)_2](TFSI)]$).[75] This cell showed electron injection times of 25ps but regeneration as slow as 3.2μs. The hole extraction time, another way of understanding regeneration, was $1.28x10^6$ times slower. To increase the efficiency of DSSCs, hole extraction must be made faster.

2.3 Splitting Water with Semiconductors

As the global demand for energy continues to rise, the need for renewable energy sources has become more apparent. One source of portable fuel that could replace gasoline and similar carbon emitting fuels is hydrogen, produced by splitting water molecules.[2] This follows the

reaction:

$$2H_2O \rightarrow 2H_2 + O_2$$

Which is comprised of the half reactions:

$$2H_2O \rightarrow O_2 + 4H^+ + 4e^-$$

$$4H^+ + 4e^- \rightarrow 2H_2$$

Semiconductors have been used for half a century to conduct electrochemical photolysis.[76,77] Nanoheterostructures have allowed the conversion efficiency to reach an extraordinary 100%, i.e. for every incident photon one H2 is produced.[78] Cadmium chalcogenides are frequently used in this process, as they have necessary valence band and conduction band levels to allow photolysis of water using visible light and exceptionally high molar absorptivities in the UV to visible regions. The creation of CdSe@CdS heterostructures greatly increased the efficiency of hydrogen evolution, only further improved by the addition of Pt or other metal tips to opposite ends of these nanorods (NRs) as a co-catalyst.[79,80] In a dot in rod CdSe@CdS system, the CdS acts as an antenna for harvesting light.[81] The electron and hole will migrate to the core CdSe and carry out transfers from there.[81] Conversely, in the Pt-tipped heterostructure, ultrafast hole trapping encourages efficient electron transfer from the NR to the Pt tips, avoiding recombination and increasing the hydrogen production efficiency.[81] Physical separation, such as that offered by pulling the electron to the tip, prevents recombination from outcompeting the hydrogen evolution. The key efficiency-limiting step, at this point in heterostructure-catalyzed hydrogen evolution, is the rate of hole transfer from the heterostructure to oxidize the water.[82] In general, hole removal is three to four times slower than electron transfer from the tip to reduce the protons to hydrogen gas.[54,83–90]

While the incredible quantum efficiency of 100% may seem to have no room for improvement, this value was only obtainable at a pH above 15.[78] This extreme pH makes the implementation of such systems difficult. Furthermore, the rod heterostructure also undergoes photocorrosion under prolonged irradiation, requiring sacrificial donors.[77,78,91] Changing the system to include a second cocatalyst can provide the CdS rod with the photochemical stability required.[92]

Using transition metal catalysts as redox mediators is a strategy that has been employed previously.[25,93–97] Other strategies have employed size dependence of the semiconductor, in this case a CdTe QD.[98] Recently, the Amirav lab has begun to tune the width of the rod in a

nanoheterostructure.[99] The barrier to tunneling is proportional to the length the electron or hole must tunnel through. The Amirav lab found that there was an optimal number of monolayers covering the CdSe core such that there was still localization, passivation, and confinement but the barrier to tunneling was at a minimum.[99]

Chapter 3

Minimizing the Reorganization Energy of Cobalt Redox Mediators Maximizes Charge Transfer Rates from Quantum Dots

3.1 Introduction

Quantum confined semiconductor nanocrystals, also known as quantum dots (QDs), are widely used in photovoltaics, hydrogen generation, light emission, and probes for biological samples.[13,32,34,94,100] Their highly tunable band gap, band edges, and emission properties, large Stokes shift, greater ability for surface functionalization, and high degree of photostability make quantum dots ideal subjects for experimentation.[29,101,102] QDs are becoming ubiquitous across many fields of study, however, there are still many fundamental questions about their behavior which have yet to be answered.

Many applications of QDs require the separation and extraction of charge.[103] Increasing the rate of charge transfer is key to improving the efficiency and sensitivity of several of the aforementioned applications. QD fluorescence quenching in the presence of an electron acceptor is an indirect way to observe charge transfer kinetics. While observing a change in fluorescence intensity of the QDs is almost trivial, the determination of what mode caused that change and what factors contributed is challenging.[40,46] Not only are there a large number of possible charge and energy transfer pathways, including non-radiative recombination, radiative energy transfer, charge transfer, and radiative recombination, but there is significant evidence that, due to the intermediate density of states between that of the bulk and a molecule, hole and electron transfer from quantum dots does not necessarily follow bulk transfer nor molecular transfer models.[53,54]

For nanocrystals, molecular charge transfer models are often applied despite limitations. In molecular charge transfer, the Marcus Electron Transfer Theory has been shown to describe the relationship between driving force and transfer rates.[48] The high accuracy of the predictions is, in large part, due to the inclusion of the reorganization energy (λ) to the model. Reorganization energy is the shift in nuclear coordinates upon the transfer of charge and includes (inner sphere) vibrational shifts (such as changing bond lengths) in both the donor and acceptor species as well as (outer sphere) movements in the surrounding solvent.[50]

In the Marcus model, there are three regions dictated by the relationship between driving force (ΔG) and reorganization energy. Where $-\Delta G < \lambda$, the system is in the normal region and an increase in driving force leads to higher charge transfer rates. Where $-\Delta G \approx \lambda$, the system is at the peak transfer rate, called the barrierless region. Lastly, when $-\Delta G > \lambda$, the system is in the inverted region and further increases in driving force should lower the transfer rate. With this heavy dependence of transfer rates on the relationship of the reorganization energy to driving force, it is odd that so little attention has been given to using reduced reorganization energy to improve charge transfer rates from quantum dots and in other photoelectrochemical systems. Understanding the precise nature of this relationship for electron transfer (ET) mechanisms can lead to greater efficiencies in solution redox mediated processes, especially in dye and quantum dot-sensitized solar cells, and photoelectrochemical water splitting.

Chelated cobalt complexes as acceptors provide an opportunity to examine charge transfer from quantum dots in a technologically relevant way. Cobalt complexes have been studied as efficient redox mediators for a variety of charge transfer applications including protein electron transfer, Dye Sensitized Solar Cells (DSSCs), and H_2 generation.[82,104–109]

In one example, a tethered cobalt complex accepted photogenerated electrons from CdTe QDs on the picosecond timescale, and also acted as an active catalyst center for reducing water to H_2.[110]

In dye sensitized solar cells, cobalt complexes are less corrosive redox mediators than the traditional tri-iodide/iodide couple and the electrochemical potentials are better placed energetically to provide a larger open circuit voltage in the device.[111] Cobalt complexes were used with porphyrin sensitized solar cells to produce an efficiency of 12% and outperformed the iodide couple.[112] Various attempts have been made to improve upon the 12% efficiency, and researchers have identified high reorganization energies of the dyes and the cobalt redox complexes as limiting factors. [105,71,113,114] It is thought that a large component of this high reorganization energy comes from the transition from low-spin Co(III) to high-spin Co(II) prompting the search for and use of complexes which do not undergo this transition.[71] Here, we demonstrate the power of carefully designed ligand cage environments around the cobalt center to minimize reorganization energy, and increase charge transfer rates by several orders of magnitude.

In this work, cadmium chalcogenide quantum dots were used as charge donors because their optical properties are well studied. Since they are much larger than a molecule, the reorganization energy of QDs can be assumed to be negligible, allowing the influence of the

reorganization of the acceptor to be isolated.[115] While it would seem that Marcus theory would already dictate the precise effect, many studies ignore or simply estimate the internal reorganization energy of the charge acceptor. Often, only the reorganization energy due to the

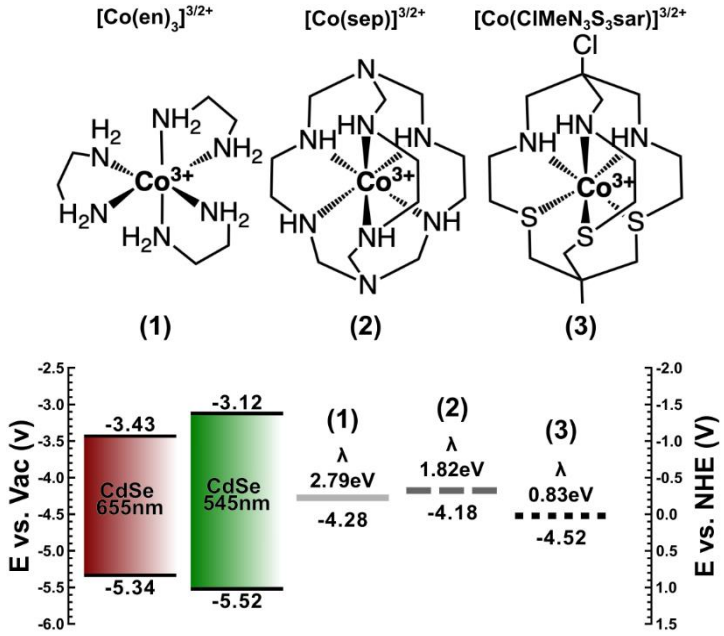

Figure 3.1: Internal reorganization energies and reduction potentials of the studied cobalt complexes and estimated band positions for idealized CdSe QDs.

solvent is considered significant when calculating the transfer rates. Studies have shown that solvent reorganization energy of molecular acceptors can be modestly manipulated by using less polar solvents to improve charge transfer, yet many applications will dictate that aqueous conditions be used.[116] For this reason, we chose to only study aqueous conditions here.

Internal reorganization of a charge acceptor can be very consequential, and even larger than the solvent reorganization energy. It is unexplored whether minimization of the internal (inner sphere) reorganization energy can be employed as an effective strategy to improve function in applications that require charge transfer from quantum dots.

Table 3.1: Properties of Cobalt Redox Mediators

	$K_{AA}M^{-1}s^{-1}$	$\lambda_i[\lambda]$ (eV) [b]	E^o(V) [c]
$[Co(en)_3]^{3/2+}$	$2.0x10^{-5}$ [a]	2.79 [3.24]	-0.224
$[Co(sep)]^{3/2+}$	5.1[b]	1.82 [2.28]	-0.323
$[Co(ClMeN_3S_3sar)]^{3/2+}$	10^4 [c]	0.83 [1.27]	0.022

Here we study photoinduced charge transfer from QDs to three cobalt complex ions: tris(ethylenediamine)cobalt(III/II) abbreviated as $[Co(en)_3]^{3/2+}$ (**1**), and the caged complexes (sepulchrate)cobalt(III/II) abbreviated as $[Co(sep)]^{3/2+}$ (**2**), and (1-chloro-8-methyl-3,13,16-trithia-6,10,19-triazabicyclo[6.6.6]icosane)cobalt(III/II) abbreviated as $[Co(ClMeN_3S_3sar)]^{3/2+}$ (**3**) (Figure 1, Table 1).[104,117] These three cobalt complexes were chosen because they have similar electrochemical reduction potentials that are within 350 mV, but have very different reorganization energies spanning nearly 2 eV. These structurally similar amine-chelated complexes are also less prone to ligand exchange than monodentate ligated complexes. Marcus theory is employed to predict the electron transfer rates from green and red fluorescent cadmium chalcogenide quantum dots, to include both effects of reorganization energy and driving force. The predicted trends are shown experimentally though steady state and time resolved photoluminescence. The results highlight the dominant role of the complexes' different reorganization energies on altering the charge transfer rates by 3-4 orders of magnitude, over the role of driving force. The experimental results suggest that Auger-Assisted charge transfer, is a potentially an active charge transfer mechanism that is not commonly included in Marcus predictions.

3.2 Experimental Methods

3.2.1 Materials

Tris(ethylenediamine)cobalt(III)chloride dihydrate (MQ 100), Lithium carbonate (≥99%), thioglycolic acid (≥99%), ammonium hydroxide (28.0-30.0% NH_3 basis) and Formaldehyde solution (37 wt% with methanol stabilizer) were purchased from Sigma-Aldrich. QDs were acquired from ThermoFisher Scientific as Qdot 545ITK carboxyl quantum dots and 655ITK carboxyl quantum dots. The QDs came as solutions at 8 μM in 50 mM borate buffer and stored at

4°C. Additional borate buffer was prepared by adding 0.618 g of boric acid to 0.1g of NaOH and 9 mL of water, sonicating until solubilized, and then filling to 10 mL. Support solutions for further dilution of the quantum dots were prepared from 300 µL of 1 mM borate buffer added to 300 µL of 15.4 2 mM thioglycolic acid in 6 mL of deionized water. Thioglycolic acid was needed to stabilize the QDs in solution and prevent aggregation. Borate buffer was necessary to maintain the solution at a sufficiently basic pH, as thioglycolic acid is known to dissociate from the surface at low pH [aldana]. *In lieu* of borate buffer, removing atmospheric CO_2 from the solutions with freeze-pump-thaw cycles also provided a sufficiently high pH to stabilize the aqueous QD solutions. However, it was difficult to retain those strict conditions throughout the experiments, and instead borate buffer provided better reproducibility. The optical density of the green QDs initially was 0.03 and for the red QD 0.045.

QDs were acquired from ThermoFisher Scientific as Qdot 545ITK carboxyl quantum dots and 655ITK carboxyl quantum dots. The QDs came as solutions at 8 µM in 50 mM borate buffer and were stored at 4°C. Support solutions for further dilution of the quantum dots were prepared from 300 µL of 1 mM borate buffer added to 300 µL of 15.4 2 mM thioglycolic acid in 6 mL of deionized water. Synthesis of $[Co(ClMeN_3S_3sar)][ClO_4]_3$ can be found in reference [104].

3.2.2 Steady State Spectroscopy

Fluorimetry was performed on an ISS PC1 photon counting spectrofluorometer using a 300 W Xe arc lamp as the excitation source. The solutions were stirred during measurement. Photoluminescence was measured with a 1 s integration time and a 1 mm slit width. UV-vis absorption spectra were measured using a Jasco 670 Spectrometer with an aqueous solution of borate buffer, and thioglycolic acid in the same concentrations as the measurement solution as a reference. Quartz cuvettes were used to mitigate any possible absorbance in the UV. Utmost rigor was required cleaning the glassware between experiments to remove trace cobalt; the cuvettes and flasks were filled with aqua regia followed by 5-10 rinses with water, blank solution, and then deionized water. The excitation wavelength used for these dots was 400 nm in order to fit into a low point in the absorbances of the Co complexes. Data of experiments using QDs emitting at 545 nm were normalized by dilution using mass. Data of experiments using QDs emitting at 655 nm were normalized for dilution by subtracting a control of diluted QDs. Core sizes were determined using the first excitonic peak in accordance with the work of Yu et. al.[110] HOMO and LUMO values of the QDs were estimated by core size.[118] Titrations were performed through 50 µL additions of 100 µM solutions of $[Co(sep)]^{3/2+}$ and $[Co(en)_3]^{3/2+}$. Titrations of $[Co(ClMeN_3S_3sar)]^{3/2+}$ were performed using 10 µL additions of a 1 mM solution. Addition of $[Co(ClMeN_3S_3sar)]^{3/2+}$ was halted once

fluorescence dropped below the detection limit of the instrument.

3.2.3 Time-Resolved Photoluminescence

Measurements were performed using a custom-built epi-fluorescence microscope. Samples were excited under wide-field illumination using a 405 nm PicoQuant pulsed diode laser with a repetition rate of 2.5 MHz. The beam was reflected with a 420 nm long pass (LP) dichroic filter (Omega Optics, 3RD420LP) into an inverted objective (Olympus UPLSAPO, apochromatic, water immersion, 1.2 N.A., 60x) and brought into focus at the sample. Fluorescence from the focal region was collected by the same objective, passed through the dichroic filter and an additional 450 or 500 nm LP dichroic filter, and then focused through a 150 μm aperture onto a single-photon avalanche photodiode (SPAD, Micro Photon Devices PD-050-0TC). A time-correlated single photon-counting unit (TCSPC, PicoHarp 300, ~35 ps) was used to generate a histogram of photon arrival times. The obtained PL decay curves were fitted using a tri-exponential function:

$$I(t) = \sum_{i=1}^{3} A_i e^{\frac{-t}{\tau_i}} \quad (6)$$

where the fit parameters τ_i and A_i are the photoluminescence decay times and amplitudes, respectively. The amplitude-weighted average decay time, τ_{avg}, was calculated to approximate the radiative lifetime component, τ_r.

3.2.4 Quantum Dot Characterization

Transmission Electron Microscopy (TEM) and Energy Dispersive X-ray spectroscopy (EDS) of the QDs were obtained with a FEI Technai Osiris digital 200kV S/TEM system. The TEM samples were prepared by drop-casting a dilute solution of QDs on a carbon coated copper grid and were dried at room temperature in air followed by vacuum overnight. The cores of the red emitting QDs were identified to be CdSe@CdS core@shell. Zinc was not detected. The green emitting QDs cores were ZnCdSeS alloy.

The hydrodynamic radii were determined using a Malvern Nano Zetasizer operating with DLS. A solution of QDs was prepared and then quenched with $[Co(ClMeN_3S_3sar)]^{3+}$ until there was no fluorescence, as the laser used for DLS was within the absorbance of the red QDs. The red emitting dots had an approximate organic shell thickness of 0.3 nm. The green had an organic shell thickness of 2.2 nm. The tunneling dampening coefficient between the two QDs was calculated and were found to be similar.

3.2.5 Cyclic Voltammetry

Cyclic voltammetry measurements were carried out with a three-electrode configuration of glassy carbon working electrode, Ag/AgCl reference electrode, and Pt mesh counter electrode. They

were recorded with a Gamry Series G300 with PHE200 software package. Measurements were done in 0.1M KCl in water. The analyte, solvent, and supporting electrolyte were bubbled with nitrogen for 30 min prior to measurement. The measurement was carried out in a nitrogen environment. In the case of the $[Co(en)_3]Cl_3$, measurements were also performed with the addition of 10 μM ethylenediamine to prevent dissociation of the Co(II) complex. Three cycles were performed for each with a scan rate of $30mVs^{-1}$ and a step size of 0.05 mV.

3.3 Results and Discussion

The electrochemical properties and the reduction potentials of the three $Co^{3/2+}$ complexes were measured by cyclic voltammetry (Table 1). When plotted against the approximate band edges of red and green fluorescing CdSe QDs, the reduction potentials of the three cobalt complexes, $[Co(ClMeN_3S_3sar)]^{3/2+}$, $[Co(en)_3]^{3/2+}$ and $[Co(sep)]^{3/2+}$ sit within the band gap of the QDs (Figure 1) and span about 350 mV. The driving force for electron transfer from the conduction band of a QD to one of these complexes therefore follows as:

$$[Co(sep)]^{3+} < [Co(en)_3]^{3+} < [Co(ClMeN_3S_3sar)]^{3+}$$

The trend is reversed for the driving force for hole transfers from the QD valence band to Co^{2+} ions. The three chosen cobalt complexes have massively different reported self-exchange rates covering nine orders of magnitude (Table 1). The more rigid cage structure of $[Co(sep)]^{3/2+}$ limits movement of the ligand shell and has a much faster self-exchange rate ($5.1\ M^{-1}s^{-1}$) than $[Co(en)_3]^{3/2+}$($2.0 \times 10^{-5}\ M^{-1}s^{-1}$). While most Co(II)hexaamine complexes are high spin, the Co(II) and Co(III) forms of $[Co(ClMeN_3S_3sar)]^{3/2+}$ are both low spin, which further limits the demand for structural changes in the ligand sphere upon changing oxidation state. The self-exchange rate constant for $[Co(ClMeN_3S_3sar)]^{3/2+}$ has not been reported but the rate constant for the closely related N-capped analog (where N– replaces C–Cl) has been determined to fall in the range 4.5×10^3 to $2.2 \times 10^4\ M^{-1}s^{-1}$.[114,119]

The reorganization energies of the three $Co^{3/2+}$ complexes were estimated from their previously reported self-exchange rates k_f (Table 1). Based on the Marcus Microscopic Model:

$$k_f = K_{P,O}\nu_n\kappa_{el}exp\left(-\Delta G_f/RT\right) \quad (1)$$

Where ΔG_f is the activation energy for the reduction of species O, $K_{P,O}$ is the equilibrium constant between precursor P and species O (which we assume here to be 1), ν_n is the nuclear frequency

factor (s^{-1}), and κ_{el} is the electronic transmission coefficient. To calculate the reorganization energy, several assumptions were made; κ_{el} is considered adiabatic and to be unity as the reacting species are close together and there is strong coupling. ν_n is assumed to be 10^{11} $M^{-1}s^{-1}$.[120] Taking this into account, we can solve for ΔG_f, and further approximate a relationship to the reorganization energy (λ):

$$\Delta G_f = -RTlog\left(k_f/\nu_n\right) \approx \frac{\lambda}{4} \quad (2)$$

The reorganization energy is made of both the inner sphere reorganization of the bonds of the molecule, λ_i, and the surrounding solvent, λ_s.

$$(\lambda = \lambda_i + \lambda_s) \quad (3)$$

The solvent reorganization energy was approximated to be 0.45 eV consistent with previous literature[121]to give approximate internal reorganization energies (Table 1). Solvent reorganization energy can be calculated according to:

$$\lambda_s = \frac{\Delta q^2}{4\pi\epsilon_o}\left(\frac{1}{n^2} - \frac{1}{\epsilon}\right)\left(\frac{1}{d_D} + \frac{1}{d_A} - \frac{2}{R}\right) \quad (4)$$

In this expression, Δq is the change in overall charge, in this case the charge of one electron, n is the refractive index of the solvent, 1.333 for water, ε is the dielectric constant, 78.4 for water at 25°C, d_D is the diameter of the donor, d_A is the diameter of the acceptor and R is the distance over which electron transfer occurs. The second bracketed term is essentially the thickness of the solvent layer between the donor and acceptor. Moving forward we assume that this thickness is approximately the same during self-exchange as with exchange between QDs and the cobalt complexes.

The nine orders of magnitude variation in self-exchange rate for the three complexes equates to a variation in internal reorganization energy spanning approximately two electron volts. While $[Co(en)_3]^{3/2+}$ was calculated to have an internal reorganization energy of 2.79 eV, the internal reorganization energy for caged $[Co(sep)]^{3/2+}$ was 1.82 eV and even smaller for the mixed donor cage $[Co(ClMeN_3S_3sar)]^{3/2+}$ at 0.83 eV. The above method of calculating reorganization energy and values given the self-exchange rates gives results that are in good agreement with literature.[121] It can be imagined that the internal reorganization energy is caused by the expansion and contraction of the ligand environment upon changing the *d*-orbital occupancy of the cobalt center.

With these reorganization energies and driving forces (ΔG) now in hand, the rates of photoinduced electron transfer from the quantum dots to the cobalt complexes were predicted

using the Marcus model (Figure 2).

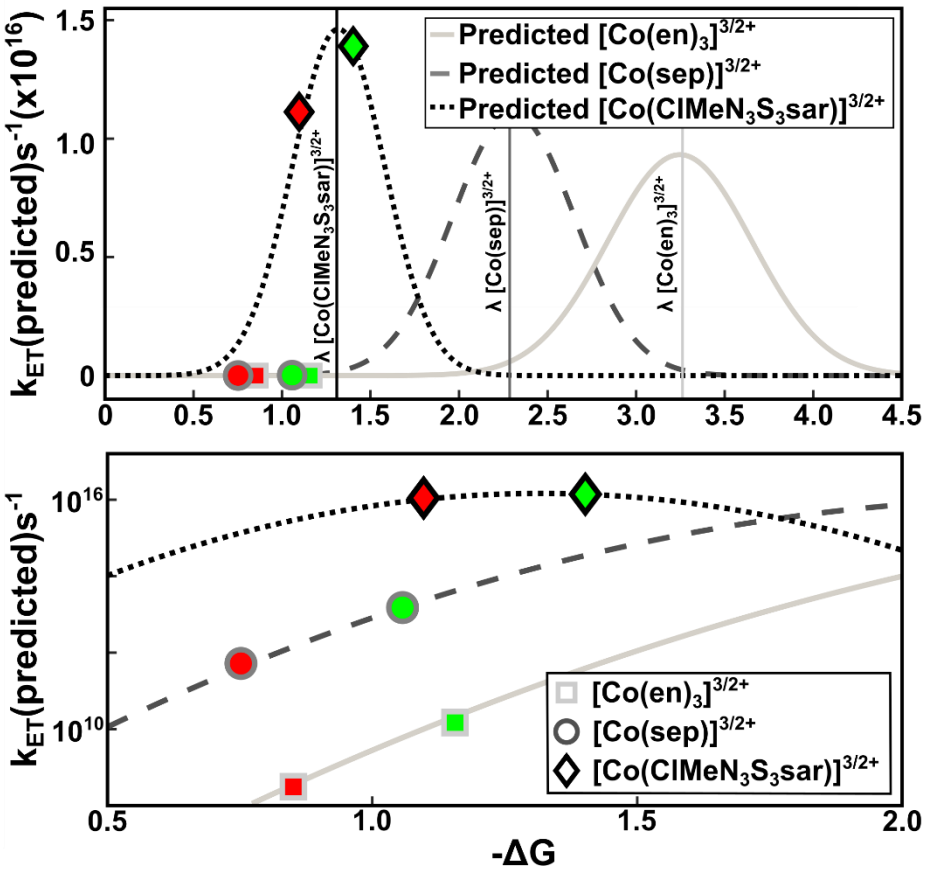

Figure 3.2: Predictions of the electron transfer rates against driving force according to standard Marcus ET theory for each of the cobalt complexes (lines) and with the specific green and red emitting cadmium chalcogenide QDs employed (colored markers). The bottom graph is on a log scale for clarity

$$k'_{ET} = \frac{2\pi}{\hbar}\frac{1}{\sqrt{4\pi\lambda k_B T}}\exp\left[-\frac{(\lambda+\Delta G)^2}{4\lambda k_B T}\right] \quad (5)$$

This simplified version includes two important assumptions that preclude direct quantitative comparison with the experiments that follow; the barrier for tunnelling and the electronic coupling (H_{DA}) is assumed to be similar for all three of the complexes to each of the QDs. Variations in shelling between batches of QDs cause these factors to differ from the assumptions due to differences in barrier height. While additional scaling from these factors is likely, much can be learned from the modeled trends, and from experimental comparison within single batches of dots. In the Marcus model, the reorganization energy presents a barrier to electron transfer, causing the rate of ET to increase with driving force. A remarkable aspect of the model is that when the driving

force exceeds the reorganization energy, the rate should decrease in what is known as the Marcus

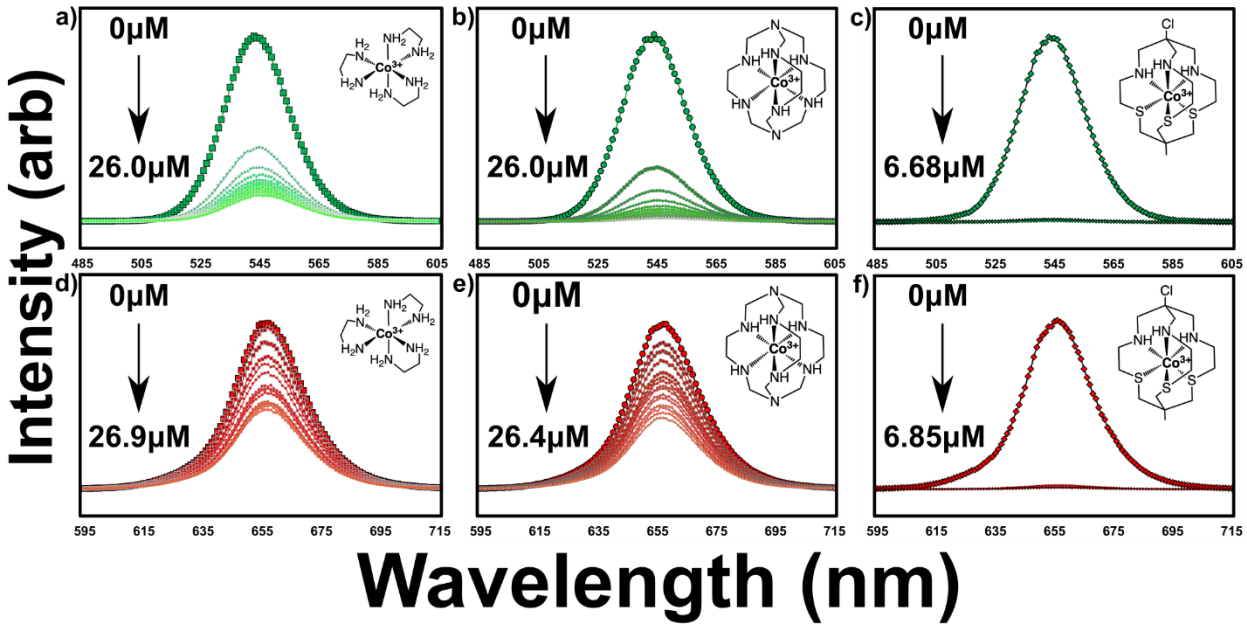

Figure 3.3: Steady state fluorescence measurements of green 545 nm (a-c) and red 655 nm (d-f) emitting fluorescent QDs in the presence of cobalt complex ions a) $[Co(en)_3]^{3/2+}$ (0-26.0μM) b) $[Co(sep)]^{3/2+}$ (0-26.0μM) c) $[Co(ClMeN_3S_3sar)]^{3/2+}$ (0-6.68μM) d) $[Co(en)_3]^{3/2+}$ (0-26.9μM) e) $[Co(sep)]^{3/2+}$(0-26.4μM) f) $[Co(ClMeN_3S_3sar)]^{3/2+}$ (0-6.85μM)

inverted region. This behavior is not always seen in quantum dots, likely due to Auger-Assisted electron transfer.[52,54]

The prediction is that the electron transfer rates from the conduction band of QDs to $[Co(ClMeN_3S_3sar)]^{3/2+}$ should vastly outstrip the rates for $[Co(sep)]^{3/2+}$ and $[Co(en)_3]^{3/2+}$ by at least two orders of magnitude when the driving force is smaller (red QDs) and up to six orders of magnitude when the driving force is larger (green QDs). While charge transfer from the conduction band of green and red emitting QDs to $[Co(ClMeN_3S_3sar)]^{3/2+}$ has the largest driving force of the three complexes, the reason for the high rates is more because of the very low internal reorganization energy which completely changes the shape of the curve (Figure 2). In turn, the $[Co(sep)]^{3/2+}$ should be faster than the $[Co(en)_3]^{3/2+}$ again, not due to the driving force, which is smaller for the $[Co(sep)]^{3/2+}$, but rather because of the smaller reorganization energy of the caged $[Co(sep)]^{3/2+}$ compared to $[Co(en)_3]^{3/2+}$.

Charge transfer from the conduction band of idealized red and green emitting CdSe QDs to

$[Co(sep)]^{3/2+}$ and $[Co(en)_3]^{3/2+}$ are in the Marcus normal regime. In contrast, because $[Co(ClMeN_3S_3sar)]^{3/2+}$ has such a low reorganization energy, the driving force is comparable in energy. As a consequence, electron transfer from red QDs to $[Co(ClMeN_3S_3sar)]^{3+}$ is in the normal regime, but is very close to the barrierless, and even slightly into the inverted regime for the green.

The effects of reorganization energy of the acceptor on the kinetics of charge or electron transfer were characterized by titrating solutions of red and green emitting cadmium chalcogenide QDs with these different cobalt complexes. The quantum dot fluorescence and subsequent quenches were monitored (Figure 3).

For both colors of dots, the $[Co(ClMeN_3S_3sar)]^{3/2+}$ caused the most intense quenching of the three complexes. It is favored to have the fastest charge transfer of the three complexes due to its largest electrochemical driving force and minimal reorganization energy. Stern-Volmer plots were generated and their linear trends suggest either dynamic or static quenching, but not a transition between the two (Figure 4). We assume all three complexes undergo the same type of quenching. The slopes provide a more quantitative analysis of the fluorescence quench. $[Co(ClMeN_3S_3sar)]^{3/2+}$ quenched the green emitting CdSe@ZnS QDs ~10 times more strongly than $[Co(sep)]^{3/2+}$ and ~60 times more than $[Co(en)_3]^{3/2+}$ (Figure 4a inset). $[Co(ClMeN_3S_3sar)]^{3/2+}$ quenched the red emitting CdSe@CdS QDs ~260 times more strongly than $[Co(sep)]^{3/2+}$ and ~338 times more than $[Co(en)_3]^{3/2+}$ (Figure 4b inset).

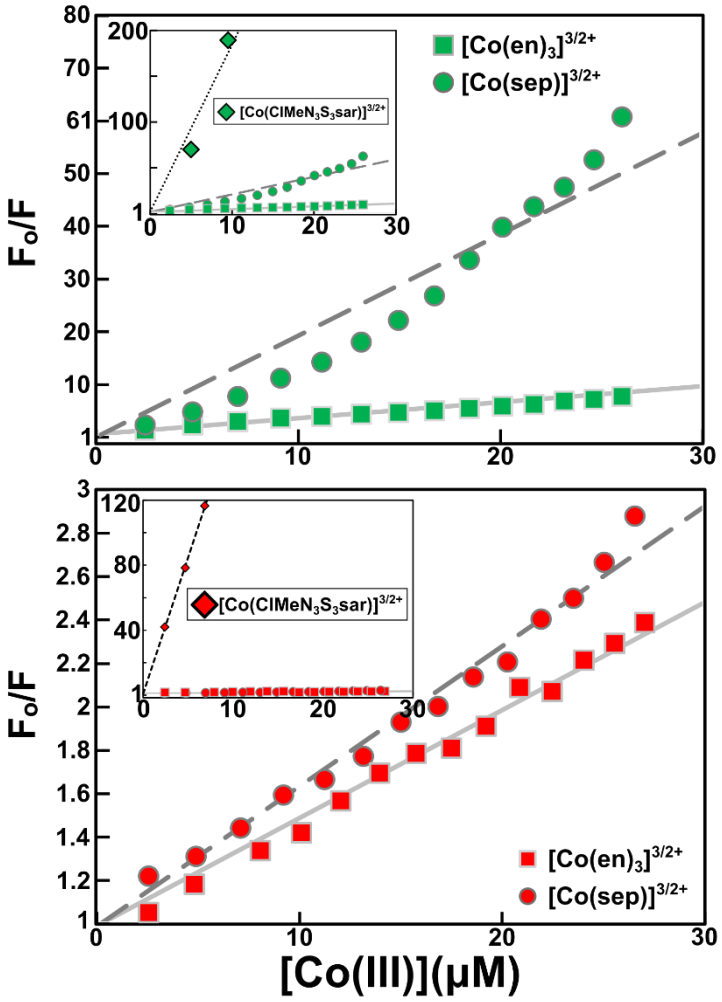

Figure 3.4: Stern Volmer plots of fluorescence where F_o is the initial summed fluorescence and F is the fluorescence in the presence of the indicated concentration of Co. a) QDs emitting at 545nm; b) QDs emitting at 655nm. Insets are on a higher scale and include $[Co(ClMeN_3S_3sar)]^{3+}$.

The comparison of $[Co(sep)]^{3/2+}$ vs. $[Co(en)_3]^{3/2+}$ highlights the importance of reorganization energy in electron transfer rates and how it can actually dominate over other trends. The driving force for charge transfer favors the $[Co(en)_3]^{3/2+}$ by 0.24 V to be faster, and yet $[Co(sep)]^{3/2+}$ has a much higher quench rate than $[Co(en)_3]^{3/2+}$ by a factor of ~6.3 for the green dots (Figure 4a) and by ~1.3 for the red dots. $[Co(sep)]^{3/2+}$ has a much smaller reorganization energy barrier than $[Co(en)_3]^{3/2+}$ by 1.95V. It is the reorganization energy barrier that explains the quenching rates rather than driving force in this experiment.

The experimental quenching trends (Figure 4) match the trends seen in the calculated rates (Figure 2), yet closer inspection shows the experiments the $[Co(en)_3]^{3/2+}$ outperforming prediction when comparing complexes in sheer orders of magnitude. Parasitic absorption by the cobalt complexes was ruled out, as it was minimal (e (400 nm, $M^{-1}cm^{-1}$) $[Co(en)_3]^{3/2+}$ = 25.5 $[Co(sep)]^{3/2+}$ = 14.1, $[Co(ClMeN_3S_3sar)]^{3/2+}$ = 391, QDs = $\sim 10^5$)[110](Supporting information).The most likely source of error is the assumption that the orbital overlap H_{DA} with the QD and all three complex ions is the same. Secondly, the experiments also capture any other non-Marcus quenching processes and intermediate steps (such as charge transfer to a surface state) that may complicate direct comparison to the Marcus predictions.

We considered the possibility that Forster Resonant Energy Transfer (FRET) was a secondary non-radiative route for energy transfer that could complicate the interpretation for charge transfer. FRET and other resonant transfer mechanisms are dependent upon the degree of spectral overlap between the donor (QD) and the acceptor (Co^{3+}) as well as the distance between them. Using the experimental fluorescence spectra of the QDs and the absorbance spectra of the cobalt complexes, the overlap was calculated to be minimal, with the largest value of $\sim 1x10^{12}$ J $mol^{-1}cm^{-1}$ nm^4 for the green dots with the cobalt complexes. The spectral overlap is then used in calculating the distance under which FRET is likely, R_o. This calculation takes into account the quantum yield of the donor QDs (~85%) and the $1/d^6$ distance dependance of the FRET process. It was determined that the R_o for this system between 1.6 and 2.6 nm. Since the green 545 nm emitting QDs have the highest amount of overlap but also an organic shell greater than 2.5 nm (Supporting Information), FRET processes are likely very minimal in these experiments.

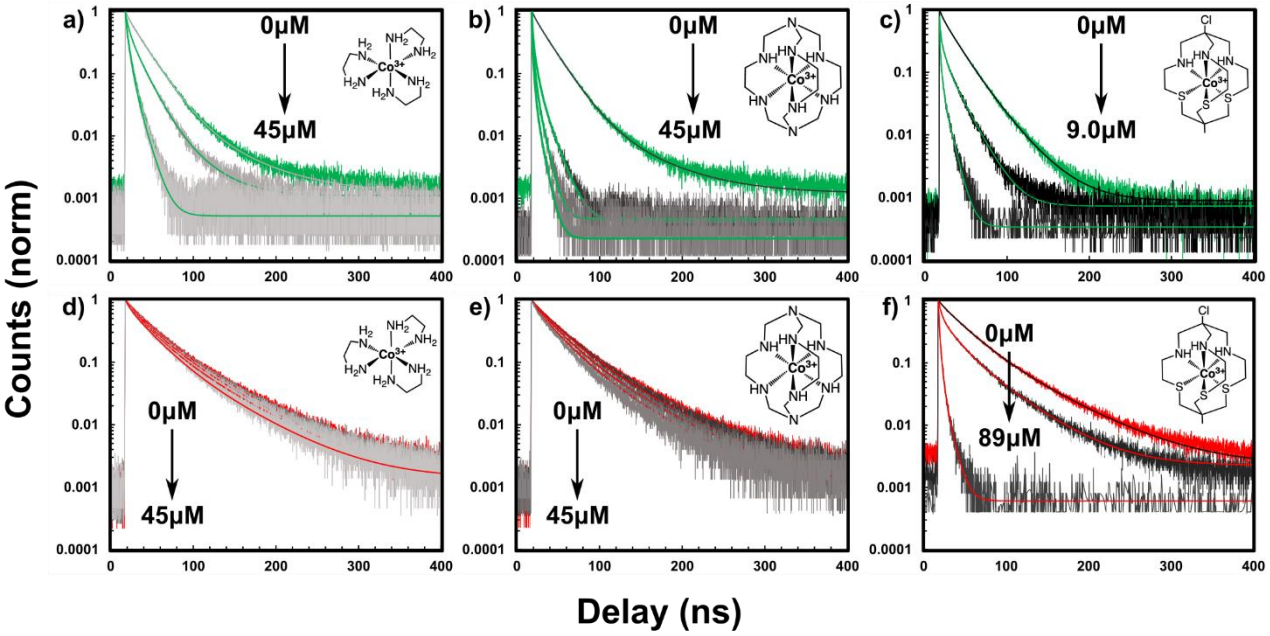

Figure 3.5: Time-resolved photoluminescence analysis of (top) green emitting (545 nm) and (bottom) red emitting (655 nm) CdSe@ZnS QDs in the presence of a) $[Co(en)_3]^{2/3+}$ (0-45 μM) b) $[Co(sep)]^{2/3+}$ (0-45μM) c) $[Co(ClMeN_3S_3sar)]^{2/3+}$ (0-9.0μM) d) $[Co(en)_3]^{2/3+}$ (0-45 μM) e) $[Co(sep)]^{2/3+}$(0-45μM) f) $[Co(ClMeN_3S_3sar)]^{2/3+}$ (0-98μM).

Nanosecond lifetime fluorescence measurements were taken of the QDs with increasing concentrations of the cobalt complexes (Figure 5) and were each fit with a tri-exponential decay function (Supporting Information). For both of the QDs measured without cobalt, each of the three decay components were matched to likely excitonic pathways according to previous literature precedent. The fastest component, ~3 ns, is typically attributed to exciton carrier trapping at defects in the core of the material. The slowest component, ~60 ns, is attributed to carrier trapping at nanocrystal surface defects. The intermediate-length component is attributed to direct, band edge, radiative recombination of the exciton. The green dots have a faster band edge radiative lifetime of ~20 ns than that of the red dots at ~27 ns, which makes sense because of the greater overlap between the hole and electron wave functions for the smaller, green emitting QDs. Overall, the average lifetime for the green QDs was faster than the red QDs, with 19.8 ns and 36.8 ns, respectively.

The addition of the cobalt complexes in all cases decreased the average lifetimes, suggesting that the charge transfer is comparable or faster than the average lifetimes of the QDs (Figure 6). The trends in the change in average lifetime follow the predicted trends from Marcus theory when reorganization energy is considered. The effect of the reorganization energy is far more pronounced for the green QDs over the red QDs due to the larger driving force for electron transfer from the raised QD conduction band to the cobalt complexes. For both red and green emitting QDs, the

addition of $[Co(en)_3]^{3/2+}$ decreased the average lifetime, but the effect was greater for $[Co(sep)]^{3/2+}$ and even more so for $[Co(ClMeN_3S_3sar)]^{3/2+}$. The near vertical decays seen at short times for the $[Co(ClMeN_3S_3sar)]^{3/2+}$ with the green and red dots and the $[Co(sep)]^{3/2+}$ with the green dots suggests that the lifetimes were so short that they exceeded the capabilities of the instrumentation. These observations match the calculated prediction that $[Co(en)_3]^{3/2+}$ should have the slowest charge transfer.

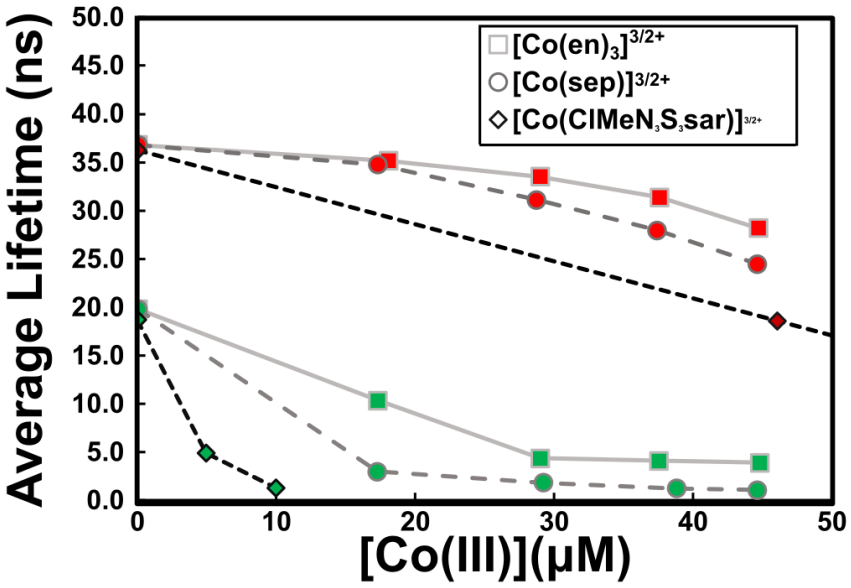

Figure 3.6: Average fluorescence lifetimes of green and red emitting CdSe QDs (markers colored accordingly) in the presence of three cobalt complex ions at varying concentrations.

Once the time-resolved fluorescence curves were fitted with tri-exponentials (SI), some more information about approximate charge transfer rates could be identified that matched the predicted trends. In the combinations where the charge transfer rates were expected to be the highest – $[Co(ClMeN_3S_3sar)]^{3/2+}$ with red or green QDs, and $[Co(sep)]^{3/2+}$ with green dots– the time resolved fluorescence saw the emergence of a new, extremely short component, that was fitted to be sub-nanosecond. For the combinations with the slowest predicted rates, – $[Co(en)_3]^{3/2+}$ with green or red QDs and $[Co(sep)]^{3/2+}$ with red QDs– the fittings showed increased contributions from components between 1-5 ns. One interpretation of this result is that charge transfer occurs at this time scale for these combinations. Due to limitations of the detector, it is not possible to fit these the

sub-nanosecond lifetimes with any greater detail, however the results agree with the predicted trends by Marcus theory. Spectroscopies that have picosecond resolution such as transient absorption are planned to achieve exact values of k_{ET}.

The ratio of the rates for electron transfer for the green vs the red dots illustrates that Marcus theory, while useful, is yet incomplete in describing this system. In general, once normalized for the difference in tunnelling barriers between the red and green QDs (approximated in SI), we expect that of the three complexes, charge transfer rates to $[Co(ClMeN_3S_3sar)]^{3/2+}$ to show the smallest improvement upon increasing driving force from red to green QDs; while charge transfer from green QDs to $[Co(ClMeN_3S_3sar)]^{3/2+}$ is in the Marcus inverted regime and should be moderated. However, experimentally, we observed that the improvement upon increasing the driving force for charge transfer to $[Co(ClMeN_3S_3sar)]^{3/2+}$ greatly outpaced the other two complexes. We attribute this difference to Auger-Assisted Charge transfer, which is most impactful at the barrierless and inverted regimes, and therefore is most effective in charge transfer from green dots to $[Co(ClMeN_3S_3sar)]^{3/2+}$ (Figure 2). As the other combinations of QDs and complexes are far below the barrierless or inverted regimes, the effects of Auger-Assisted Charge transfer are modest.

3.4 Conclusions

A series of Co-based redox mediators with varying reorganization energies and similar electrochemical potentials were studied for their charge transfer from QDs. Marcus theory predicts that both driving force to the acceptor and the reorganization energy effect charge transfer rates. In this case, the theory predicted that the effect of minimizing reorganization energy would far outweigh the subtler effect of varying driving force on maximizing the charge transfer rates.

The N/S mixed donor redox mediator $[Co(ClMeN_3S_3sar)]^{3/2+}$, has the smallest internal reorganization energy of the three cobalt complexes at only 0.83 eV. This compound has a cage structure that prevents ligand movement, and belongs to a select family of ions where both the Co(II) and Co(III) species are low spin due to the influence of the S-donor atoms, which requires very little movement in the ligand shell to support changing oxidation state. These features allow it to have a smaller reorganization energy than the rigidly caged $[Co(sep)]^{3/2+}$ (l=1.82eV) and the relatively floppy $[Co(en)_3]^{3/2+}$ (l=2.79eV).

In steady state quenching experiments low reorganization energy $[Co(ClMeN_3S_3sar)]^{3/2+}$ was able to quench green and red QDs 140 and 180 times more effectively than $[Co(en)]^{3/2+}$, respectively. Time resolved photoluminescence experiments suggests that the charge transfer to $[Co(en)]^{3/2+}$ was

1-5 ns, but transfer to $[Co(sep)]^{3/2+}$ (with a large driving force) or $[Co(ClMeN_3S_3sar)]^{3/2+}$ was even faster than the instrument could measure and could only been deemed as sub-nanosecond.

Comparison of the predicted rates and the average rates observed by TRPL, suggest that Auger-Assisted electron transfer is an active mechanism for charge transfer, that was not predicted by the Marcus Model employed.

Previous studies of charge transfer from QDs to charge acceptors, are often performed in organic solvents, which serendipitously lower solvent reorganization energy. However, many applications of QDs, such as photocatalytic water splitting and biological applications require solvation in water. Here, we chose to study charge transfer kinetics under these more stringent conditions, to ensure that the results were relevant to applications.

The results here suggest that careful design of the ligand environment of redox mediators to reduce reorganization energy is an important route forward in improving technologies were charge

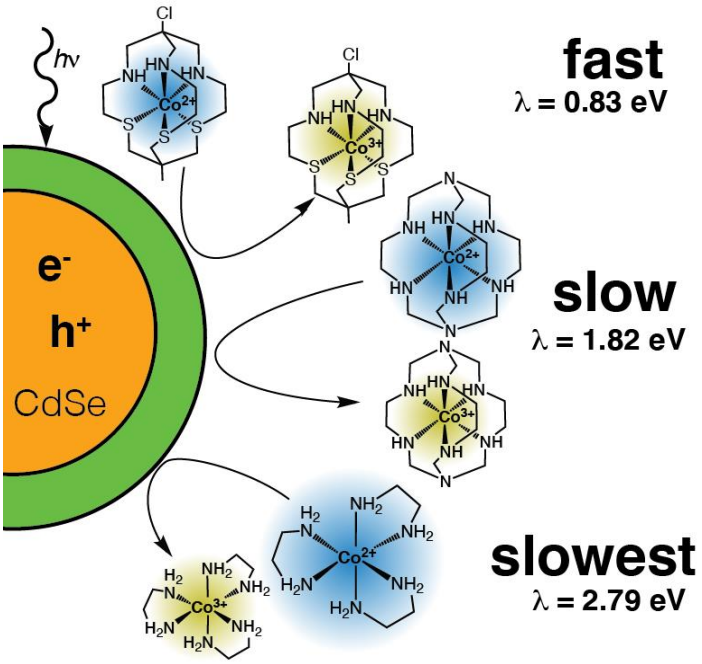

transfer from QDs is featured.

Chapter 4: The Surface of Iron Pyrite

4.1 The Draw of Fool's Gold

Iron pyrite is a commonly found mineral worldwide. I found my first piece of pyrite in Ouray Colorado more than twenty years ago. I made the usual mistake and thought it gold. "Fool's Gold" was thought to be of no monetary value, but with the advent of the semiconductor revolution it has been reimagined as a possible photovoltaic material. As we approach four decades of intensive pyrite research, pyrite has also gained attention for other possible applications, including use in battery technologies, sensing devices, and as a photocatalyst. The most anticipated application, however, is in photovoltaics.[4,122,123] Since photovoltaic research on pyrite began in the early 1980s, hundreds of researchers have yet to produce an economically viable solar cell.

The allure of pyrite lies in the reported values for its bandgap, absorption coefficient, electron mobility, carrier diffusion lengths, and in its apparent abundance. The accuracy of some of these values continues to be debated. The stated bandgap of pyrite is 0.95eV (indirect), with a direct transition at 1.03eV, but there is reason to believe it could be as low as 0.58eV.[124] This ideally-placed bandgap allows pyrite to approach the Shockley-Quiesser limit of efficiency for an ideal single junction solar cell.[125] In addition, pyrite has a high value for electron mobility (μ=360cm^{2}V^{-1}S^{-1}) for single crystals.[126,127] The carrier diffusion length is estimated as being between 100nm and 1000nm. Combined with its electron mobility properties, the diffusion length should allow for the extraction of generated charges, i.e. the charge carriers should be able to reach the cathode and the anode without recombination.

One advantage of pyrite over other semiconductors is its remarkably high absorption coefficient of α>105 for hυ>1.3eV, permitting the use of an exceptionally thin layer of pyrite in many applications. A pyrite thin film of 20nm absorbs 90% of incoming light. By contrast, crystalline silicon would require a 300μm thick layer to achieve the same percentage of light absorption.[127] This attribute should expand the range of possible applications of pyrite-based photovoltaics with additional research.

In addition, pyrite is earth abundant, inexpensive, and nontoxic. Assuming a potential 10% cell efficiency and a 5μm active layer, the United States' primary power demand could be satisfied with a tenth of the pyrite that is currently discarded as mining waste in six states alone.[128,129]

The field of pyrite solar cell research began in the early 1980's with work by Tributsch and coworkers. Their work that continued through the 1990's created the most successful pyrite solar cells to date. In fact, they made the only successful pyrite solar cells.[126,127,130–147] The initial architecture used a photoelectrochemical cell, while later work was based on the Schottky cell design.[141,148] Tributsch and his colleagues developed many of the initial characterizations of the fundamental values for the photoelectrochemical, photoconductive, and electronic properties of pyrite. Their pyrite devices seemed to show high quantum efficiencies (over 90%) and photocurrents (upwards of 40mA cm^{-2}). Surprisingly, however, the cells never performed at the levels that should have been expected from these values, as the cells achieved a solar conversion efficiency of just below 3%.[148] The low efficiency was attributed to a low photovoltage of 200mV. All attempts to generate a higher solar conversion efficiency cell have performed significantly worse; the lack of efficiency has usually been attributed to a poor photovoltage.

A 2009 study by Wadia et al. galvanized the scientific community's efforts to make pyrite solar cells a reality. The study showed that, when measured in lifetime energy output, a pyrite solar cell operating at 4% efficiency should be as equally cost-effective as a 20% efficient crystalline silicon cell.[4] As silicon cells have now dropped in cost (to USD $0.20/W in 2018), while silicon-based solar cell efficiencies have increased to over 26%, the impetus for pyrite solar cell development has decreased.[7,8]

Pyrite solar cell research has continued, due in part to concerns over the current localization of production of cells to China and Taiwan, as well as the continuing interest in using a readily available material. Much of the cost-effectiveness of silicon was achieved through massive investment in solar production research and development, large scale manufacturing facilities and market-creation, leading to economies of scale and scope. Pyrite is one of the few semiconductor materials that could be as cost-efficient as silicon-based cells with substantially less capital investment and seven decades of research.[4] Pyrite can form the basis for thinner, lighter, and possibly flexible solar cells (a possibility afforded to designers based on nanoparticle technology) that would not be feasible with silicon's large and very brittle crystal structure. Put together, there should be considerable motivation to functionalize pyrite photovoltaics as an alternative to traditional silicon-based solar cells.

The excitement around pyrite research was severely tempered in 2012, when Steinhagen et al. published a work showing what was apparently phase pure pyrite failing to produce any photoconversion efficiency in four different cell configurations.[149] The pyrite used by Steinhagen

was synthesized using hot injection with $FeCl_2$ tetrahydrate in octadecylamine with sulfur powder in diphenyl ether. Hot injection with iron chloride is a common method of synthesis, although the ligand and solvent choices are somewhat unusual. While this disheartening result caused many to cease their pursuit of a pyrite cell, other scientists sought to understand why this seemingly super-material failed to function in the slightest degree.

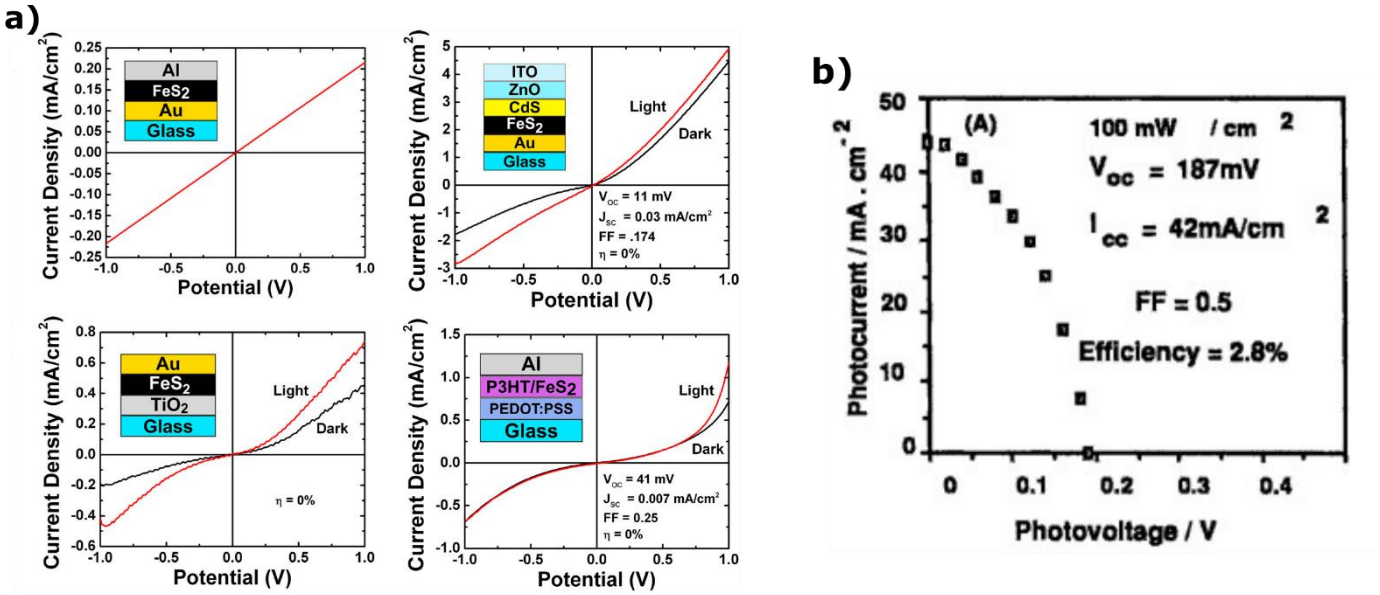

Figure 4.1: a) The photovoltaic cells made by Steinhagen et al. showing that regardless of cell type pyrite cells showed no photoconversion efficiency.[149] b) The most efficient pyrite solar cell made by Ennaoui et al.[138]

The highest recorded efficiency to date for a pyrite photovoltaic device comes from a photoelectrochemical cell made by Ennaoui et al.[138] This cell consisted of an n-type FeS_2 single crystal and aqueous iodide/tri-iodide electrolyte (I^-/I_3^-). The limiting aspect of this cell was the low open circuit voltage which kept the efficiency at 2.8% (Voc=187mV). The cell had a fairly high short circuit current and moderate fill factor (Isc = 42mA/cm2, FF = 0.50). Fill factor is a measure of relative squareness, not density. The comparison must be made to the state of the art n-type crystalline single junction silicon cells which have an efficiency of 26.7% and a similar short circuit current although a much larger open circuit voltage (Voc = 738mV; Isc = 42.7 mA/cm2; FF = 0.85).[7,150] We may, from this, understand that the key to success is increasing the open circuit voltage in pyrite cells.

Solar cell efficiency is governed by the principles discussed in section 1.3. To derive a more in-depth nuanced understanding of V_{OC} the ideal diode equation may be solved when the current is set to zero. The form of the equation is:

$$V_{OC} = \frac{nkT}{q} ln\left(\frac{I_L}{I_O} + 1\right) \quad (1)$$

The principal difference between this form and the standard form is the included ideality factor. The ideality factor can vary from 1 depending on factors such as the recombination type. K is Boltzmann's constant, T is temperature, q the charge of the electron, I_L is light generated current, and I_0 represents dark saturated currents. The dark saturated current depends on the charge carrier recombination and can vary by orders of magnitude. The orders of magnitude variation in the dark current implies that V_{OC} is a measure of carrier recombination in the cell. Low V_{OC} can then be understood as being attributable to high levels of charge recombination within the cell. Not only does a high degree of recombination prevent a significant amount of charge extraction, but the Shockley-Quiesser limit depends on the assumption that all recombination is radiative. Any other forms of recombination will bring down the efficiency. While there is a consensus in the literature that the low V_{oc} is the limiting factor in pyrite photovoltaics, the debate now dominating the field is what is causing this high charge carrier recombination and general lack of potential. The debate centers around four questions at the present.

First, are defects responsible for the underwhelming performance of pyrite cells and if so, are these defects in the surface, bulk, or both?[151]

Second, since carrier concentrations are often measured at degenerate levels, what is the extent and nature of this unintentional doping?[136,152–155]

Third, what is the role of phase purity, if any?[156–160]

And finally, the most difficult question, why has no one made a cell with similar properties to those made by the Tributsch group in the last 40 years?

4.2 The Role of Defects

The effort to determine if defects were the principal cause of the underwhelming performance seen above began with observable lattice defects. The measured stoichiometry is very rarely seen to be the ideal stoichiometric 1:2 Fe to S. Observed samples have had a deviation of $FeS_{2-x,}$ where x is as high as 0.25.[161] Sulfur deficiencies have been interpreted as sulfur vacancies where the unit cell is mostly intact. If these degrees of sulfur deficiencies are considered in terms of the unit cell, there are four iron atoms per cell but only seven of the eight sulfur atoms expected. As

there are approximately $2.52*10^{22}$ Fe atoms per cm^3, it is evident that even one in eight of expected sulfur atoms being vacant could lead to the $\sim 10^{21}$ carriers per cm^3 of degenerate doping observed.[162] There are some complications with this argument. Notably, until recently, there was not a consensus as to whether the observed doping was n type or p type.[155,163]

Sulfur vacancies have traditionally been thought of as leaving the unit cell intact with missing sulfur atoms, at least in computational models. Models of the pyrite cell structure have been investigated by Birkholz et al.[147] They use the presumption that the sulfur vacancy acts like a simple Schottky defect, in that changes in the local coordination environment and oxidation states occur in order to preserve net charge neutrality. The vacancy of one sulfur of the dimer results in the breaking of four bonds for each sulfur vacancy: three S-Fe bonds and one S-S bond. The formal charge of the remaining sulfur increases to 2- as a result of the vacancy. Importantly, the formally octahedral coordination around the Fe atom shifts to square pyramidal, and locally, obtains C_{4v} point symmetry. This reduction in symmetry causes new splitting of the Fe 3d orbitals. The σ bond interaction shifts, causing defect states within the valence band and in the mid-gap Fe dz_2-like states. The mid-gap states can be highly prevalent and function as trap states, severely diminishing the bandgap. The exact position and width of this defect band is not understood, potentially explaining the apparently very low open-circuit voltage.

There is contention as to whether bulk sulfur vacancies are the cause of the apparent sulfur deficiency. Computational studies have posited that the barrier for formation of bulk sulfur vacancies is too high to allow for the likely formation of these vacancies. In a 2011 study, the barrier for formation was calculated at 2.4 eV, making the formation of sulfur vacancies extremely unlikely.[164] Other computational studies found the sulfur vacancy (V_S) formation energy to be nearly 2-3.5 eV.[159,165,166] It is important to remember that while these formation energies seem very high, a similar value was calculated for metal oxides and oxygen vacancies.[167] These oxygen vacancies are known to be highly prevalent.[165] Studies of in-situ high resolution XRD have shown that pyrite has a very inflexible lattice parameter.[167,168] The studies indicate that the apparent deficiency of sulfur is possibly attributable to secondary phases such as pyrrhotite. Low concentrations of pyrrhotite even though in sufficient concentration to cause the apparent sulfur deficiencies and carrier concentrations may nonetheless be invisible to XRD.

At a minimum, pyrrhotite has the potential to lower the bandgap; pyrrhotite's reported bandgap is 0.8eV. DFT studies have called into question, however, whether pyrrhotite acts as more metallic than this bandgap would imply. While pyrrhotite did show an increase in conductivity with

temperature, indicating it may be a semiconductor, a low semiconductor-to-metallic transition temperature is possible. This increase in conductivity with temperature only occurred after an activation energy of 0.01 to 0.14 eV. The number of holes in the valence band may be understood as:

$$p = 2\left\{\frac{m_p^* kT}{2\pi\hbar^2}\right\}^{\frac{3}{2}} e^{(E_V - E_F)/kT} \quad (1)$$

Where k is Boltzman's constant, T is the temperature in degrees Kelvin, m_p^* is the hole effective mass, E_V is the valence band energy, and $E_F$is the Fermi energy. This relationship shows us that, if the Fermi level is indeed below the valence band, there must be free holes to conduct.

Secondary phases such as pyrrhotite are often difficult to detect via XRD as XRD is unreliable for phases below 3% composition but will often appear through magnetic measurements. Stoichiometric pyrite is diamagnetic, but sub-stoichiometric pyrite or impure samples can often exhibit a paramagnetic of ferromagnetic response.[143,169,170] Magnetic measurements have also been used to determine if the secondary phase marcasite, orthorhombic FeS_2, is present. The degree to which marcasite may contribute to a low photovoltage is not well-understood. [170]

There is no definitive proof that the sub-stoichiometry of pyrite is the culprit for the electrical properties.[142,170] Work of the Tributsch group using pyrite crystals grown with CVD showed crystals with a stoichiometry of 1:1.88 Fe to S outperforming those with a higher ratio in terms of photovoltage. There is a somewhat discernible linear trend within this data showing an increase of the photovoltage with higher sulfur content, however, seen in Figure B.1.[142] It is difficult to determine to what extent impurity elements may have affected these samples, as each sample had numerous impurities including chromium, tungsten, bismuth, and bromine. It must be noted that no one has replicated the work of the Tributsch group. All other attempts, using supposedly perfect stoichiometries, have not resulted in any reports of improved photovoltage.[171]

4.3 The Effect of the Surface

As stoichiometry doesn't appear to have a direct impact on the photovoltage of pyrite, it may be appropriate to consider other factors. Quite early in the field of pyrite research, it was noted that chemically etching the surface was the only way to achieve any amount of photovoltaic response.[137] Natural pyrite crystals show almost no photoconductive response.[172] Polishing and

other standard methods of treatment were not sufficient for either synthetic crystals or natural crystals to increase photoconductive responses. Instead, successful pyrite samples had been treated with a solution of $HF/CH_3COOH/HNO_3$.[134] At room temperature, however, this acid treatment still did not exhibit an open circuit voltage exceeding 40mV. It should be noted that this "successful" example comes from the Tributsch group. Other treatments from the Tributsch group also showed success. Liu et al. demonstrated the use of KCl on an electrode surface increased the photocurrent response and decreased the dark current.[134] This treatment was most successful when done under illumination. Furthermore, other surface oxidation treatments were shown to lower the dark current and increase photoresponse. Some of these treatments liberated H_2S, with the increased photocurrent calling into doubt whether sulfur vacancies were responsible for poor performance.[134,143] Overall, evidence for surface conduction has been seen from the temperature dependence of resistance, resistance anisotropy, thickness dependent resistivity, sensitivity to surface preparation, and observed surface insulator-to-metal transitions.[173]

Surface treatment of nanocrystalline pyrite with ligands has also been shown to be successful in creating a photoconductive response to AM 1.5 light.[174] The photoresponse was thought to be the result of surface passivation and was done with trioctylphosphine oxide (TOPO). It was noted that without TOPO on the surface, the pyrite can release sulfur into the air. With the addition of TOPO, the pyrite was stable for more than a year. Bi et al. do not make a cell or test for the open circuit voltage, however, so it is difficult to determine whether the ligands altered the photovoltage. Additionally, TOPO is infamous for containing many impurities. The authors do not discuss how this might alter the function of pyrite in this case or its stability.[175]

Other treatments have sought to use hydrazine to stabilize pyrite. Hydrazine did alter the work function, but other aspects weren't seen to shift in a productive way.[162] The primary function of hydrazine for many researchers has been to strip the surface of any native ligands. This research found that pyrite treated with hydrazine wasn't useful as an absorber layer but was useful as a contact or buffer layer. Density of grain boundaries was the physical property with the largest influence on conductivity.

Because the properties of nanoscale materials are strongly influenced by their surfaces, attempts have been made to change the ligands to influence their surface states. The methodologies for ligands to passivate surface states were adapted from the successful methods used on quantum dots.[174,176] Ligand exchanges were performed, and the absorption characteristics were observed in addition to electrical characteristics. Ligands were varied based on their anchor groups, bridging

groups, and chain lengths. The nature of bridging groups will be further explored below. We found that ligands with the same anchoring group had very similar shifts in the optical absorption edge but had very different conductance. The conductance was seen to shift based largely on the bridging

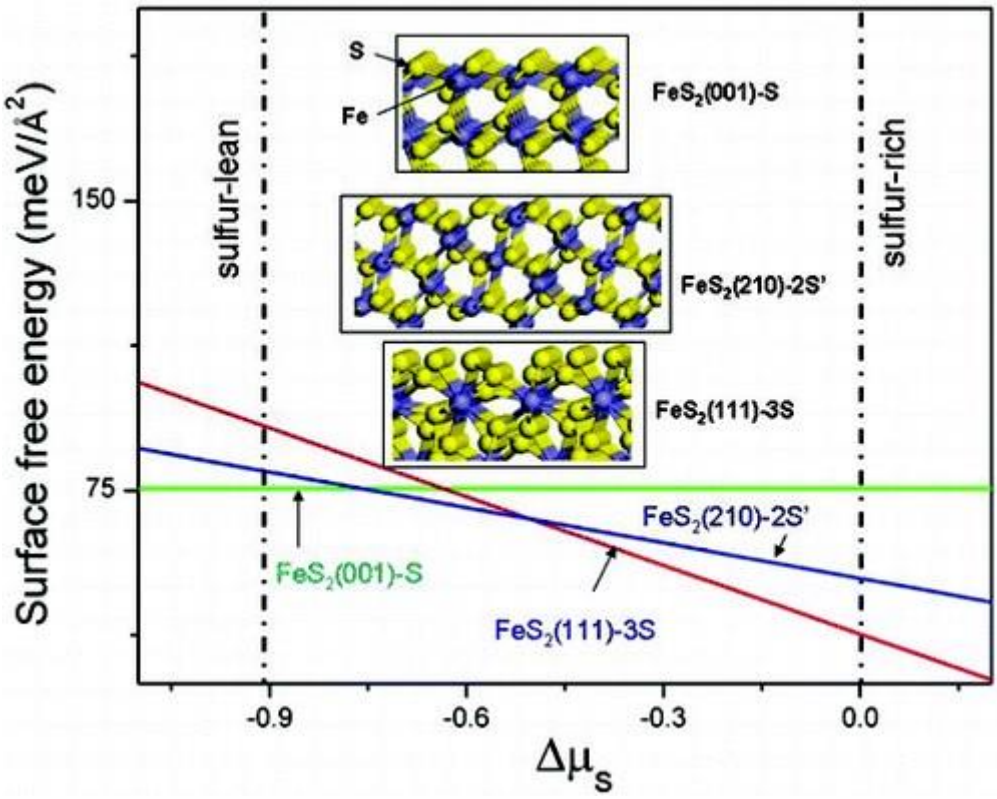

Figure 4.2: Free energy of different surfaces with sulfur rich to sulfur lean environments from reference [1].

unit. This excitement over exerting control must be tempered by the knowledge that the surface photovoltage (SPV) was still exceptionally small. Indeed, it was two to three orders of magnitude smaller than SPV signals from conventional semiconductors.

Given the demonstrated influence of the surface on the optical properties, albeit minor, it becomes necessary to understand the nature of the surface. It is commonly understood that exposed pyrite surfaces may decompose into H_2S or sulfuric acid.[177] The most commonly observed surface is the S-terminated (100) surface. As opposed to generating sulfur vacancies within the bulk, computational studies have instead found a low defect formation energy for this surface (~0.4eV).[164,178] This lower defect formation energy was actually the most stable in low sulfur environments when comparing the (100), (210), (111), and (110) surfaces.[1] This understanding led

many researchers to strive to make more “perfect cubes” which would be terminated in (100) surfaces.[179] Early research used electrochemical methods to avoid anything other that the (100) surfaces, converting all surfaces to FeS and then using molecular hydrogen at the unfavorable FeS sites to create FeSH.[143]

Given the evidence of a relationship between the surface and surface photoactivity, some research suggests that there is a relationship between surface sulfur stability, the formation of sulfur vacancies, and performance.

The precise configuration of the (100) pyrite surface can vary greatly, leading to different degrees of surface charge. The surface can be cleaved such that either an Fe-S or a S-S bond breaks . In the event that the Fe-S bond breaks, there is a layer of Fe^{2+} terminating the surface with $(S_2)^{2-}$ below. When the persulfide cleaves, there is instead a Fe^{2+} and S^{1-} terminating the surface. The sulfur monomer likely reduces to a more stable S^{2-}. This reduction can even induce sulfur dimer vacancies. The sulfur and dimer vacancies have been linked to many potential issues including surface conductive states, a surface FeS layer, a surface inversion layer, surface nonstoichiometry, surface traps, deep traps, and reduced surface bandgap.[1,180,181] In a comprehensive study of 120 pyrite samples grown by chemical vapor transport (CVT), also called chemical vapor deposition (CVD), it was found that n-type single crystals demonstrated a p-type surface inversion layer.[173] In this particular example, the inversion layer was found to be 3nm in thickness, equating to roughly 6 unit cells deep.[173]

4.4 Phase Impurities

The role that other iron sulfur phases might play in photovoltaic failure has been a matter of some debate among those studying pyrite photovoltaics. Many mechanisms for the formation of pyrite go through intermediate phases, notably an FeS phase.[182,183]. Many of the decompositions of pyrite form other phases.[184] Early research focused on marcasite, the orthorhombic polymorph of pyrite. It was thought that marcasite had a low bandgap of only 0.34eV and was potentially responsible for the low photovoltage.[185] This was a troubling possibility, because at the concentrations necessary to create the degenerate doping levels, marcasite was nearly impossible to detect with x-ray diffraction (XRD). Researchers were forced to turn to magnetic measurements or to Raman to disprove the presence of marcasite. The narrative on marcasite has since changed dramatically. Recent work has demonstrated that properly identified marcasite has an indirect

transition closer to 0.83eV.[156] There is a direct transition closer to 2.0eV. This suggests that if there is a marcasite impurity, it is not attributing to the low photovoltage. Recent measurements of pyrite/marcasite mixed phase films have been shown to have a higher diffusion coefficient for photogenerated minority carriers, versus a phase-pure pyrite sample.[157,158] This is potentially the explanation for the observed improvement in the photoactivity of pyrite/marcasite films mixtures. Though avoiding marcasite was a focus for many years, at this point in pyrite research, the other sulfur deficient phases are of far greater concern. Greigite, pyrrhotite, and troilite are thought to be much more detrimental to the performance of pyrite films. Upon conversion to pyrrhotite, pyrite films showed a drop of resistivity of four orders of magnitude and a sign reversal from n-type to p-type.[160]

4.5 Questions About the Bandgap

The failure of pyrite's surface photovoltage has called the nature of its bandgap into question. While early optical measurements seem to show a bandgap of 0.95eV, DFT calculations differ.[186] First principles studies have found that the sulfur 3p-dominated conduction band does not strongly contribute to the optical absorption. This observation suggests that the difference between the optical and fundamental band gaps are significant. While DFT calculations should be taken with a grain of salt, it suggests a new understanding of pyrite's bandgap is necessary. Transient reflection measurements found that it was possible to excite carriers at 0.58eV, significantly below the accepted 0.95eV.[124] Not only were carriers excited, but these carriers' lifetimes reached a quasi-relaxed state extremely quickly, needing only 10ps. The lifetimes of these relaxed carriers were shown to be 30ps and 200ps, lifetimes likely related to an annihilation process, calling the carriers' supposed high mobility into question.

4.6 The Current State of Pyrite Research

There is evidence that the lack of photovoltage comes not from surface states, but from bulk defects. In an intensive study by Cabàn-Acevado et al., bridging many characterization techniques, only a large number of bulk deep donor states could be responsible for the low Voc.[187] There was a buried junction, likely due to surface Fermi level pinning; this junction could be intentionally exploited for photovoltaics. The ionized deep donor states produced a small barrier height of only 230mV, with most of this barrier at 130mV within 10nm of the surface. Observed ultrafast lifetimes

suggest that the diffusion of carriers is extremely limited. Together, these finding indicate that attempts to make photovoltaic iron pyrite must include a method to mitigate the formation of intrinsic bulk states. In addition, for nanocrystalline and polycrystalline films to function, some method of overcoming surface defect states is necessary at grain boundaries.

These studies demonstrate that the keys towards making a functioning pyrite solar cell will come from making defect-free pyrite with passivated surfaces. It is therefore appropriate to examine where pyrite occurs in nature, and how it is synthesized. Iron-sulfur minerals are earth abundant, potentially functioning in a large number of biogeochemical processes.[188] The large quantities of iron sulfide have been attributed to: (a) the generation by bacteria through the reduction of sulfate, and (b), from expulsion of hydrothermal fluids from which the sulfides precipitate.[189] There are six naturally occurring phases: Mackinawite, troilite, pyrrhotite, smythite, greigite, and marcasite.[189] This already-complex system is further convoluted, because below 350°C pyrrhotite forms with a large number of ordered vacancy superstructures. Additionally, phases such as marcasite and greigite are metastable, and very rarely found in nature, often complicating synthetic work.

Phase-pure pyrite formation is accordingly arduous to obtain. There are other iron sulfide phases with lower sulfur ratios that are stable at room temperature. The S_2^{2-} dimers add inherent difficulties as any absent S leads to formal charge changes. In the natural and synthetic worlds, few precursors will decompose to form the S_2^{2-} units directly leading to the sulfidation of sulfur poor phases. Usually this is mackinawite, pyrrhotite, or greigite.[183,188,190,191]

As might be anticipated, the knowledge that a perfect crystal was desired led many researchers to attempt nanocrystalline syntheses to form pyrite solar cells, although many other methods have been used. Early work focused on CVD,[161] MOCVD,[192] and spray pyrolysis.[193] In the attempt to create perfect crystals, the field has shifted into synthesizing nanoscale structures and films. In particular, many researchers have tried to utilize colloidal synthesis because of its cost-effectiveness and tunable nature. Beginning with the efforts of the Law group, hot injection has become one of the most common methods for forming nanoparticles.[194] Hot injection, hydrothermal, and solvothermal methods have allowed for the control of size, morphology, and surface, while amplifying any surface effect issues.[122]

The use of diallyl disulfide instead of elemental sulfur in a colloidal synthesis is a recent innovation from the MacDonald lab.[195] Diallyl disulfide decomposes into the sulfur dimer, meaning

that preliminary formation of Fe-S does not occur. This effect was shown by taking aliquots during the synthesis and evaluating them with Raman spectroscopy.[196]

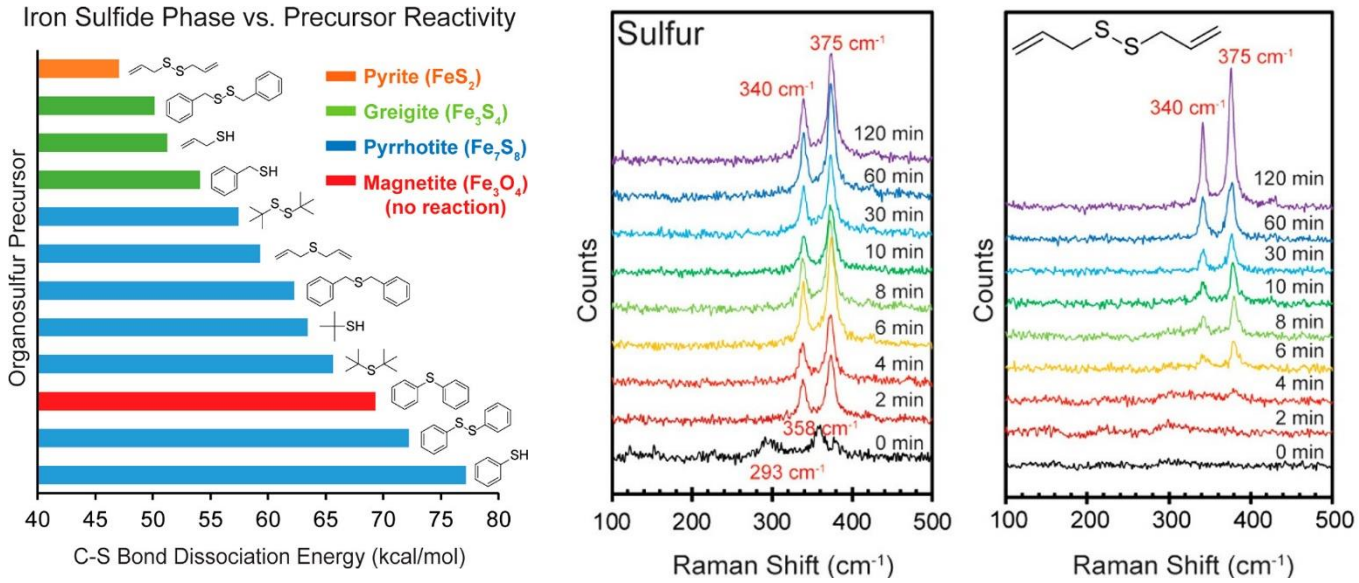

Figure 4.3: left) the bond-dissociation energy of sulfur precursors used by Rhodes et al. (right) Aliquots taken during reaction for a pyrite synthesis using sulfur vs. diallyl disulfide by Rhodes et al.

The work of Rhodes et al. demonstrated that the low bond dissociation energy (BDE) of the C-S bond of the diallyl disulfide alone among the other disulfides led to the formation of pyrite. The other disulfides had a much higher BDE for the C-S bond which led the R-S-S-R to dissociate to R-S and S-R. Similar strategies of the direct production of pyrite will be necessary to avoid bulk defects.

4.7 Iron Pyrite in Batteries

One alternative use of iron pyrite is as the cathode active layer in batteries.[197,198] Pyrite has been studied in this capacity since the early 1980s.[199] FeS_2 offers the possibility of a solid-state conversion battery. There are several advantages to FeS_2 in this role; the high specific capacity, non-toxicity, and natural abundance seem ideal for making a very inexpensive solid-state battery. As of 2000, the materials cost estimate was 50$ kWh^{-1}, which was five times lower than lithium and lithium-ion batteries.[200] The theoretic specific capacity of FeS_2 is 894 $mAhg^{-1,}$ as opposed to Li ion batteries with a capacity closer to 200$mAhg^{-1}$. Of eight common battery systems studied, only Li_2S outperformed FeS_2 in its specific capacity.[9] Initial cells were operated at very high temperatures (nearly 400°C). These cells showed reversibility above 200°C, with the initial theory that FeS_2 formed Li_2FeS_2 to FeS_y and S. Above 200C, a reaction occurs between the FeS_y and S reforming FeS_2.

It is interesting to note that most syntheses of pyrite going through a similar pathway must be done at similar temperatures. Intercalation batteries have inherent limitations in their design, most notably, that cycling often includes large volume changes. These large volume changes upon cycling cause mechanical fatigue and can induce rapid failures as lithium is exposed to air through cracks in the case.

Nanoparticulate pyrite is often chosen for this battery applications over bulk pyrite. It has been demonstrated that the smaller the particles, the higher the capacity and rate capability.[201] This phenomenon was attributed to higher surface area to volume ratio and short Li^+ pathways. The higher ratio also led to more interfacial area for competing decomposition reactions and capacity fading. Research suggests particles on the length scale of the diffusion length of Fe during cation exchange would have much more reversible reactions.[202]

4.8 Iron Pyrite in DSSCs

While efforts to make iron pyrite into an effective absorber layer have been stymied by the properties listed above, iron pyrite has been proven useful as a counter electrode in DSSCs.[203] Dye-sensitized solar cells (DSSCs) are a highly promising technology for solar energy capture. (Chapter 2 has much more information on the benefits and limitations of this technology.) Pyrite inks and nanorods have been observed as operating as a counter electrode, with efficiencies that are comparable to platinum, at only a fraction of the cost. The ink operated at η=7.31% versus 7.52% for Pt.[204] The nanorods operated at η=5.88% versus 6.23% for Pt in the same cell architecture.[205] When combining "nanowhisker" pyrite with reduced graphene oxide, the pyrite outperformed Pt with a η=7.38% versus η=6.24% for Pt in the same system.[206] Pyrite grown by spray pyrolysis operated with higher efficiencies than Pt when run with the traditional I_3^-/I^- couple.[207] The pyrite here had an η=8.0% versus η=7.5% for Pt. It was possible for this system to use a Co(III)/Co(II) electrolyte couple, although with lower efficiencies for both the PEDOT and pyrite (η=6.3% and η=6.3% respectively). The use of pyrite is a promising means to lower cost and increase performance of DSSCs.

Chapter 5: Pyrite

5.1 Unsymmetric Disulfides

5.1.1 Introduction

The work of Rhodes et al. showed it was possible to directly produce pyrite without going through intermediate phases.[195] This is because rather than sulfurizing an FeS intermediate, Rhodes used diallyl disulfide. Rhodes theorized that this was due to two sequential nucleophilic attacks, SN_2' reactions, by amine nucleophiles.[208] Bond dissociation energy calculations were done demonstrating that among the disulfides probed by Rhodes, the C-S bond was weaker than the S-S bond only in the case of the diallyl disulfide. We probed what effect the nucleophile had upon the phase of iron sulfide produced and found no discernable trend.

The surface termination of pyrite has long been known to contribute to the photoconversion efficiency problems. It is highly desirable to find a way to terminate the surface with a sulfur containing ligand, especially one with a persulfide to bond with any dangling Fe^0. Recent work on crystal bound ligands encouraged the use of a thiol that was both ligand and sulfur source.[209] Crystal bound thiols that were used as the sulfur source in the formation of Cu_2S particles sat in high coordination sites with a terminal S layer.

To address the needs of the surface and take advantage of the production of persulfide possible with the use of diallyl disulfide, a set of unsymmetric disulfide ligands were made. Phenyl allyl disulfide and benzyl allyl disulfide were synthesized and reacted with pyrite seed particles. XRD, TEM, XPS, ATR, NMR, UV-Vis, GC-MS, and Raman were used to characterize the resultant particles.

5.1.2 Experimental Methods

5.1.2.1 Materials and General

All glassware is oven dried prior to use. All reagents and solvents were used as received unless otherwise specified. Standard Schlenk line techniques under N2 were used unless otherwise specified. A J-KEM Scientific Model 210 temperature controller was used with a heating mantle for reaction temperature control.

Anhydrous iron(II) chloride beads ($FeCl_2$, 99.99%), hexadecylamine (HAD, 90%), oleylamine (OAm, 70%), $FeCl_2$ beads were stored in the glove box or kept under N_2 until use.

5.1.2.2 Computational Methods

DFT calculations were done in the vein of Guo et al. to calculate the bond dissociation energy of the unsymmetric disulfide for the allyl-S bond, the S-S bond, and the S-phenyl bond.[210] Calculations were done in Gaussian using the Boese-Martin Kinetics (BMK) functional. The 6-31G(d) basis set and the single point energy 6-311G(d,p) basis set were used to optimize molecular geometries.

5.1.2.3 X-ray Photoelectron Spectroscopy

X-Ray Photoelectron Spectroscopy samples were prepared by dropcasting particles suspended in xylene with two layers. Kapton tape was used as a mold. Samples were dropcast onto an intrinsic silicon wafer and placed in vacuum for 8 hours prior to measurement. XPS measurement was performed using an Ulvac-PHI Versaprobe 5000. Monochromatic Al x-rays (1486 eV), and a takeoff angle of 45 degrees off sample normal were used in each acquisition.

5.1.2.4 Nuclear Magnetic Resonance

NMR spectroscopy was performed using a Bruker 600MHz Spectrometer. Samples were prepared in $CDCl_3$ or D_2O depending on solubility.

5.1.2.5 Transmission Electron Microscopy, X-ray Diffraction, and Attenuated Total Reflectance

X-ray diffraction was performed using a Rigaku SmartLab X-Ray diffractometer equipped with a CuKα radiation source and a D/tex Ultra 250 detector with an operating voltage of 40kV and current of 40mA. Samples were prepared by dropcasting a concentrated solution of nanoparticles onto glass sample holder.

TEM images and EDS measurements were acquired using a FEI Tecnai Osiris STEM operating at 200kV with ChemiSTEM for EDS detection. TEM grids used were carbon film 300mesh copper.

Attenuated Total Reflectance Spectroscopy (ATR) measurements were taken using a Thermo Scientific Nicolet iS5 FTIR with an iD5 ATR attachment.

5.1.2.6 Pyrite Synthesis

The pyrite particles used for evaluating the effect of the unsymmetric ligand was modified from the work of MacPherson et al.[179] 253.5mg (2.0mmol) of $FeCl_2$ anhydrous beads was added to a 250mL 3 neck RBF with 384.8mg (12.0mmol) of S. 20g of HDA was ground with a mortar and pestle and added to the neck of the round bottom flask with a 2.5cm stir bar. Septa were added to the two side necks and a condenser with chilled water. The setup was added to the Schlenk line and a thermocouple punched through one side. The flask was wrapped with glass wool and foil and set under nitrogen as the temperature was raised to 100°C. Once the HDA had melted, the flask was placed under vacuum and the stir rate set to 240rpm. Once the flask reached 100°C, the vacuum was switched to nitrogen. The temperature was raised to 250°C and stirred for 3 hours. At the end of the 3 hours, the heat was removed and the glass and wool removed as the system was allowed to return to room temperature.

The set HDA became a solid at room temperature (RT). The N_2 was flushed through the system. One septum was removed as the nitrogen flow was set high. 507mg (4.0mmol) of $FeCl_2$, 262.9mg (8.2mmol) of S, and 30mL of OLAM were added and the septum returned. The system was heated to 70C under N_2 with the condenser running constantly. The temperature was raised to 200°C with a stir rate of 750rpm. While the temperature was still below 100°C, the system was set

under vacuum. After the temperature reached 100°C, the system was switched to N_2. The system was kept at 100°C for 9 hours. At the end of this reaction, the temperature was allowed to go back to RT by removing the heating mantle, glass wool, and foil. The flask was kept under N_2 for the duration of experiments.

Samples were prepared by heating the flask to 70°C under N_2 and then pipetting out 20mL. These aliquots were placed in centrifuge tubes. Particles were suspended in chloroform with ethanol as the antisolvent. The particles were crashed with the washing solvent. The particles were vortexed and sonicated and then spun at 8000rpm for 5 minutes. This washing procedure was done 5 times.

5.1.2.7 Phenyl allyl unsymmetric synthesis

Phenylallyl disulfide was first made by taking a 100mL Schlenk flask and adding 40mL of THF. This was placed in an insulated bowl and 1.05mL of thiophenol (12mmol) was added to this flask and set stirring for 20 minutes. 0.8mL of sulfuryl dichloride (10mmol) was added dropwise. This was stirred for 1 hour at 0°C while a second flask was prepared. A 250mL round bottom flask (RBF) was placed on a stir plate and 30mL of THF was added. To the second flask, 3.1mL of triethylamine (22mmol) and 0.82mL of 2-propene-1-thiol (10mmol) was added. This flask was set to stir at 750rpm. At the end of the hour, the contents of the first flask were added dropwise to the second to avoid fumes. This was stirred overnight, and the following day washed with saturated sodium bicarbonate. The solution was concentrated by rotoary evaporization.

5.1.2.8 Ligand Treatments

Ligand exchange in the manner of Li et al. was performed using a wide variety of ligands.[176] For this method, a concentrated sample suspended in xylene was dropcast onto a glass slide using a Kapton tape mold. Several layers were deposited and the sample allowed to dry at least 2 hours. The Kapton tape was removed. The glass slide was placed in a centrifuge tube and a 0.1M solution of the ligand of choice in MeOH was added. This was allowed to sit for 24hours at a minimum. Another attempted method of ligand exchange was to measure 30mg of dried FeS2 particles into a 6 dram vial. A 0.1M solution of the desired ligand was pipetted in and the solution was stirred at 750rpm for 24 hours.

5.1.3 Results and Discussion

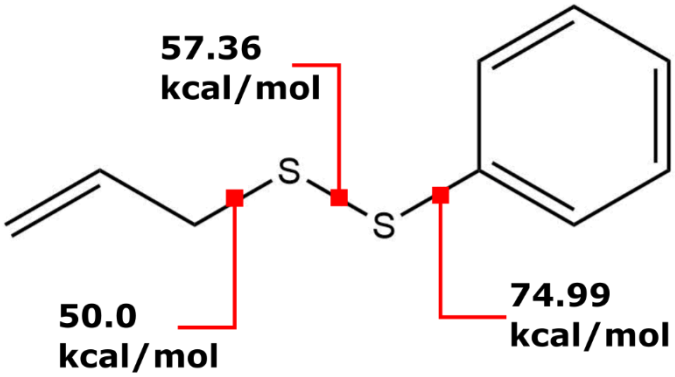

Figure 5.1: Calculated BDEs of the phenyl unsymmetric disulfide.

The calculated BDE for the allyl-S, S-S, and S-phenyl bonds shows that the premise of such an unsymmetric disulfide has promise. As anticipated, the allyl-S bond was the weakest (50kcal/mol), the S-S bond the second weakest (57.36kcal/mol), and the S-phenyl the strongest (74.99 kcal/mol). The difference in energy between the Allyl-S bond and the S-S bond was not as much as desired, only 7.36kcal/mol.

XRD demonstrated that after using the heated treatment, the only phase observed was pyrite as seen in Figure C12. There is a small aberration at 30 degrees. The exchange process was monitored by Attenuated Total Reflectance (ATR). The major peaks between 2800cm-1 and 3100cm-1 are characteristic of a C-H stretch. Quantitatively these peaks have been used previously to monitor ligand exchange. The increase here is troubling as the removal of alkyl chains should have diminished these peaks. The peak located around 1450cm-1 is within the region expected for a phenyl group, peaks at 907, 989, and 1640cm-1 are characteristic of allyl peaks. This would seem to indicate that there is still a significant quantity of allyl groups on the surface.

NMR of nanoparticles is complicated by the Nuclear Overhauser Effect.[211] The effect is such that the NMR shifts closest to the surface of the nanoparticle is spread and shifted. An example of free oleylamine and oleylamine bound to the surface pyrite is found in Figure C2. In the event there is free ligand in solution, due to the dynamic equilibrium of ligands with the surface, there can still be sharp peaks at their appropriate shifts. The vanillin peaks are perhaps the easiest to use to see if OLAM is still on the surface. It is possible to see from Figure 5.3a that the untreated particles have a mix of free and bound OLAM from the combination of both sharp peaks and broadened peaks at 4.9ppm. This peak is absent from the treated particles in Figure 5.3b, indicating that it is possible that the increased ATR C-H stretches do not come from native OLAM.

XPS was taken and can be seen in Figure C4. From XPS of the iron 2p3 spectra, it appears that the treatment did not decrease the amount of iron(III) but rather increased it. This is attributed to the increase in intensity of the peak at 712eV. This is potentially due to oxidation of the sample rather than the unsymmetric disulfide breaking iron coordination at the surface.

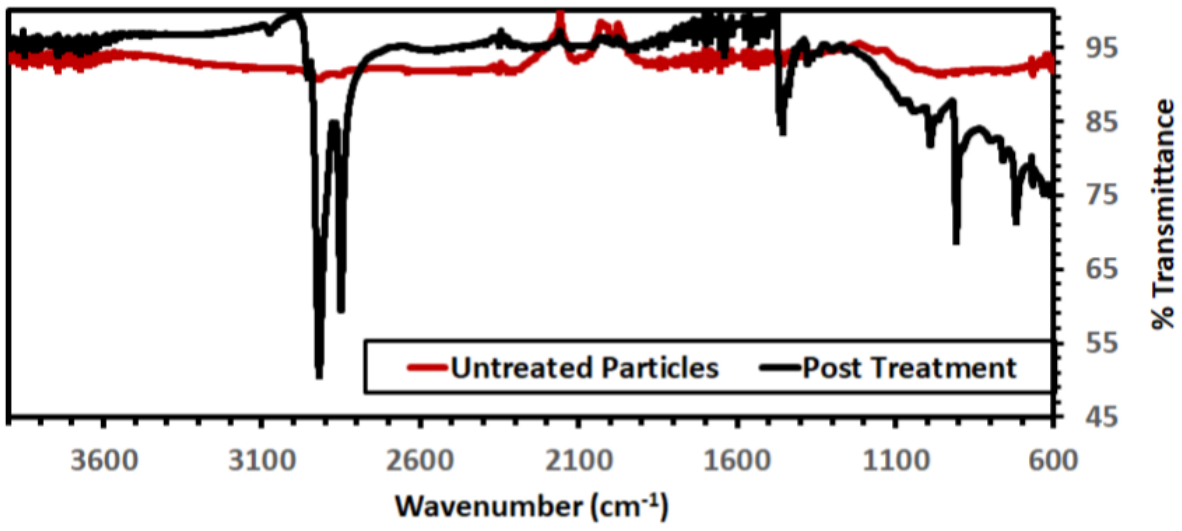

Figure 5.2: ATR spectra of particles treated with unsymmetric ligand.

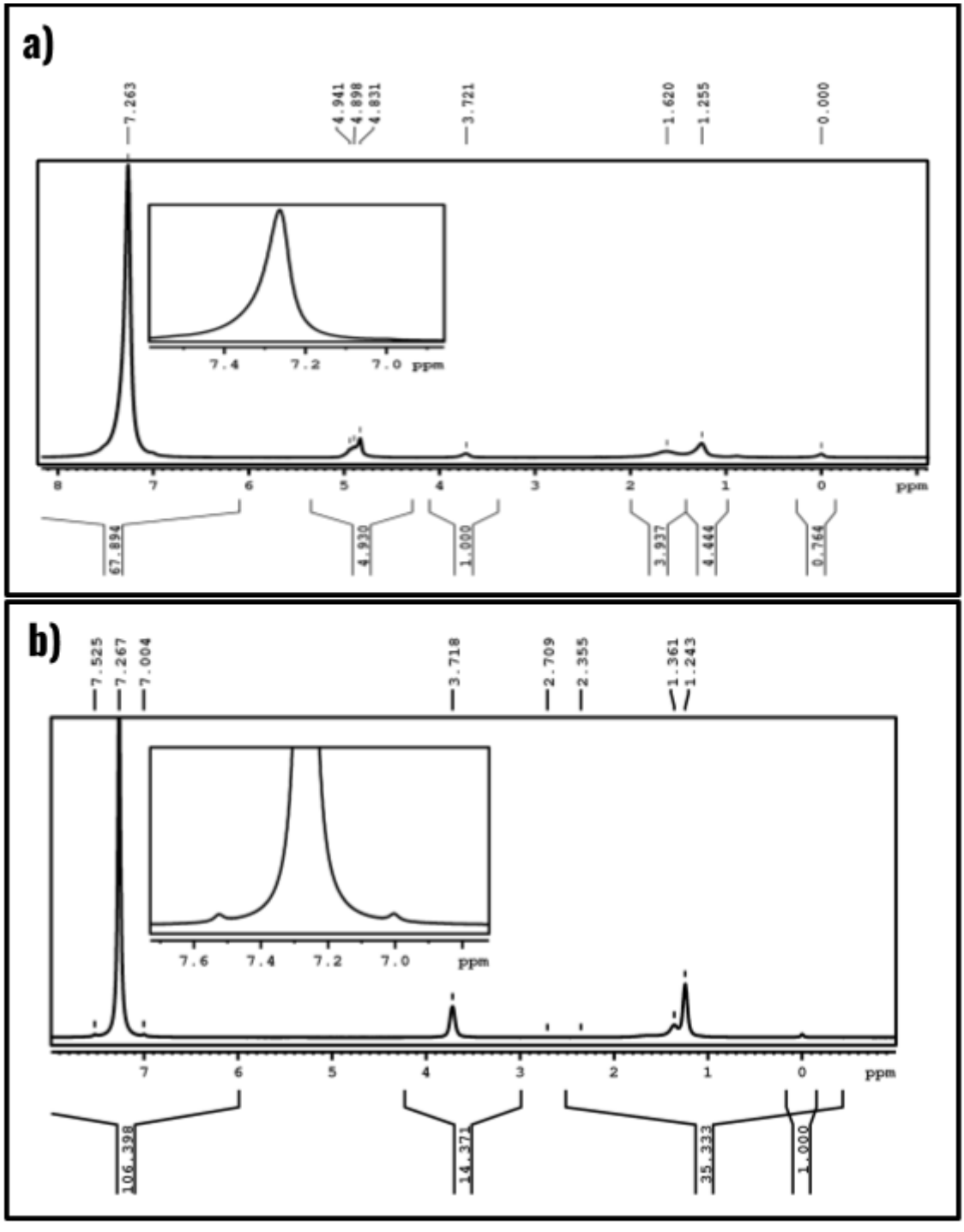

Figure 5.3: ^{1}H NMR of pyrite particles treated with unsymmetric ligand. A) shows NMR of the particles with only the native ligand, oleylamine. b) ^{1}H NMR of particles treated with unsymmetric disulfide.

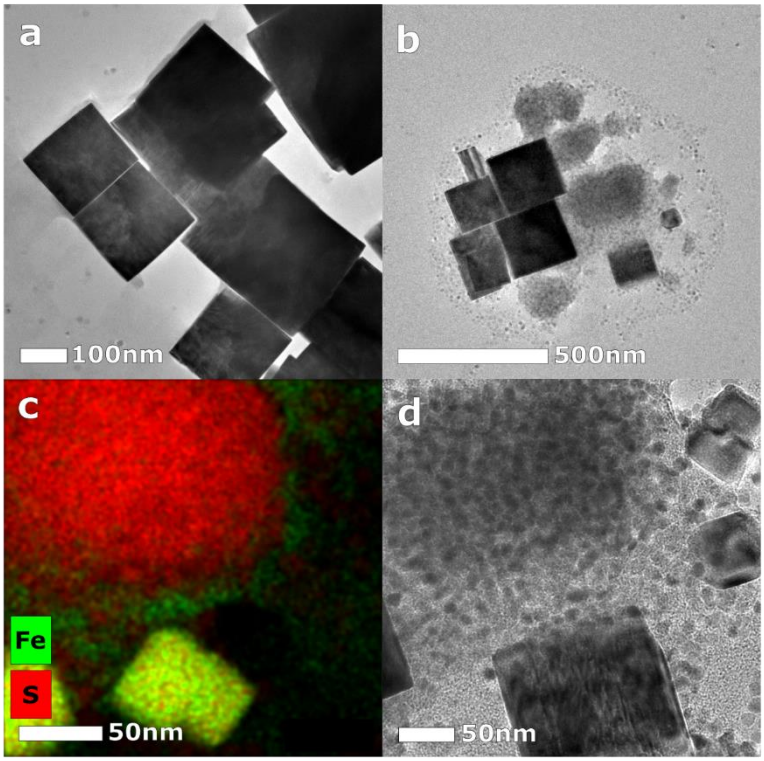

Figure 5.4: TEM of pyrite cubes a)untreated particles. b)a wide-view of particles seeming to "burst" apart. c) STEM-EDS of a cube appearing to be pulled apart. d) A higher magnification of b) where is possible to see the highly homogenous smaller particles.

The most accurate picture of what effect treating the particles with unsymmetric ligand had is observable by TEM. The untreated cubes, visible in Figure 5.4a, are roughly 200nm across. The large cube here is characteristic of the synthesis type used. After treating the particles with unsymmetric disulfide, the particles appear to have been eaten Figure 5.4b-d. Some of the large cubes appeared to have burst and were surrounded by small, highly crystalline particles closer to 10nm in size such as those seen in Figure C1. From Figure 5c, it appears that the unsymmetric leached the iron out of the particles and re-coordinated as smaller particles. The precise mechanism, and the reason why only some cubes appeared eaten, is unclear.

5.2 Phase Transformations of Pyrite

5.2.1 Introduction

As was stated in section 4.7, the uses of iron pyrite extend beyond photovoltaics. Batteries are one area of interest for iron pyrite. Pyrite batteries have historically been utilized in very high temperatures in efforts to maintain reversibility.[212] One of the intermediate phases for one of the proposed reactions necessary for reversibility has never been seen at temperatures <400C. The proposed reversible reaction takes the form:[212,213]

FeS_2 <-> $Li_3Fe_2S_4$<->$Li_{2+x}Fe_{1-x}S_2$ (x~0.2) +$Fe_{1-x}S$<->Li_2FeS_2<->Li_2S+Fe (1)

Pyrite batteries, especially pyrite lithium-ion batteries, have been using nanocrystalline materials. Regardless of whether the proposed pathway in Equation 1 is the correct one, it becomes necessary to understand the relationship between pyrite phase and temperature for nanocrystalline pyrite. Towards that end, work was undertaken with Nicole Moehring to determine the mechanism of phase change for nanocrystalline pyrite.[184]

Pyrite cubes were synthesized in the fashion of Macpherson et al. due to the strong control over shape.[179] The cubes made in this fashion are terminated in {100} surfaces which are the most stable in sulfur-lean conditions.[1] Synthesized cubes were cleaned and then characterized by preliminary XRD and TEM prior to in situ heated experiments.

5.2.2 Experimental Methods

5.2.2.1 Particle Synthesis

To make the necessary cubes terminated in {001} surfaces, a modified version of the synthesis by Macpherson et al. was carried out.[179] Anhydrous iron chloride ($FeCl_2$, purity 99.99%), was purchased from Strem Chemicals. $FeCl_2$ beads were stored in the glovebox until immediately prior to use or stored under N_2 externally; oleylamine (Olam, purity ~70%), hexadecylamine (HDA, purity ~90%) were purchased from Aldrich; sulfur powder (S, 99%) was purchased from Sigma Aldrich. All glassware was oven dried prior to use. All reagents and solvents were used as received unless otherwise specified. Standard Schlenk line techniques under N_2 were used unless otherwise specified. A J-KEM Scientific Model 210 temperature controller was used with a heating mantle for reaction temperature control.

The synthesis began with a nucleation step. 253.5mg(2.0mmol) of $FeCl_2$ and 384.4mg(12mmol) of S were added to a 100mL three neck round bottom flask (RBF) with a large (2.5cm) stir bar followed by 20g of HDA. Septa were added to the side necks and the flask was placed on a heating mantle. A

thermocouple was punched through one septum and a chilled water condenser was added to the center neck. The setup was placed on a Schlenk line and the RBF was wrapped well with glass wool and foil. The reaction was heated to 100°C under N_2 and then stirred at 240rpm under vacuum. The temperature was maintained at 100°C under vacuum for 1 hour and switched to N_2 and the temperature was raised to 250°C. The reaction was kept at 250°C for 3 hours stirring at 750rpm. After 3 hours the heat source was removed and the reaction allowed to return to room temperature. Stirring was turned off and the HDA hardened.

The growth step was performed with the product of the nucleation step. N_2 was left flowing over the solidified HDA. The temperature was raised to 70°C and once no longer a solid, stirring was set to 750rpm. The N_2 flow rate was increased and the septum without the thermocouple was removed quickly. 507mg(4.0mmol) of $FeCl_2$, 262.9mg(8.2mmol) of S, and 30ml of OLAM were added under N_2 gas flush. After 5 minutes, the reaction was placed under vacuum. The temperature was set to 200°C and stirring maintained at 750rpm. Once the temperature reached 100°C the reaction was switched to N_2. The solution was stirred under N_2 at 750rpm for 9 hours wrapped with glass wool and foil with a chilled water condenser constantly running. After 9 hours, the glass wool and foil was removed and the RBF was allowed to return to room temperature (reactions where the glass wool and foil were not immediately removed saw a far higher instance of pyrrhotite).

The flask was kept under N2 for the duration of the experiments. 20mL aliquots were removed from the solidified HAD by heating the flask to 80°C and pipetting out the appropriate amount under N_2 flush. Samples were washed five times prior to TEM and XRD. The samples were washed by adding the particle solution to centrifuge tubes and adding chloroform. The tubes were spun at 8000rpm for 5 minutes. The pellet was kept and the supernatant discarded. This procedure was repeated 5 times. Particles were then stored under nitrogen prior to experimental measurements.

5.2.2.2 In-Situ X-Ray Diffraction

In situ XRD measurements were performed with a Rigaku SmartLab X-Ray diffractometer and a PTC-EVO temperature controller. The x-ray radiation source was Cu Kα(λ=0.15418nm) with an operating voltage of 40kV and an operating current of 44mA and a Dtex Ultra 250 1D silicon strip detector. A highly concentrated sample was dropcast onto the platinum sample holder and the solvent allowed to evaporate. The sample temperature was increased stepwise from 22°C to 55°C with a ramp rate of 4°C/min as measured by an R type thermocouple with an accuracy of ±1.5°C

contacting the Pt heater. An XRD pattern was collected every 50°C with a holding time of 3 min before and 20 min after for consistency in measurements. All high temperature measurements were performed under vacuum to maintain conditions similar to the in situ TEM experiments also performed in this work.

The percent phase composition and crystallite size were determined using Rietveld refinements. These were performed in the PDXL program using whole pattern powder fitting excluding regions where the platinum sample holder had peaks. Refinements were all run for 1000 cycles. Pyrrhotite is identified using JCPDS PDF#15-1767 and pyrite with JCPDS PDF#42-1340.

5.2.3 Results and Discussion

In situ XRD found a distinctive phase transition from cubic pyrite to hexagonal pyrrhotite between 400C and 450C. This was in close agreement with the in situ TEM carried out by Moehring. The removed portions of the spectra correlate to the Pt sample holder.

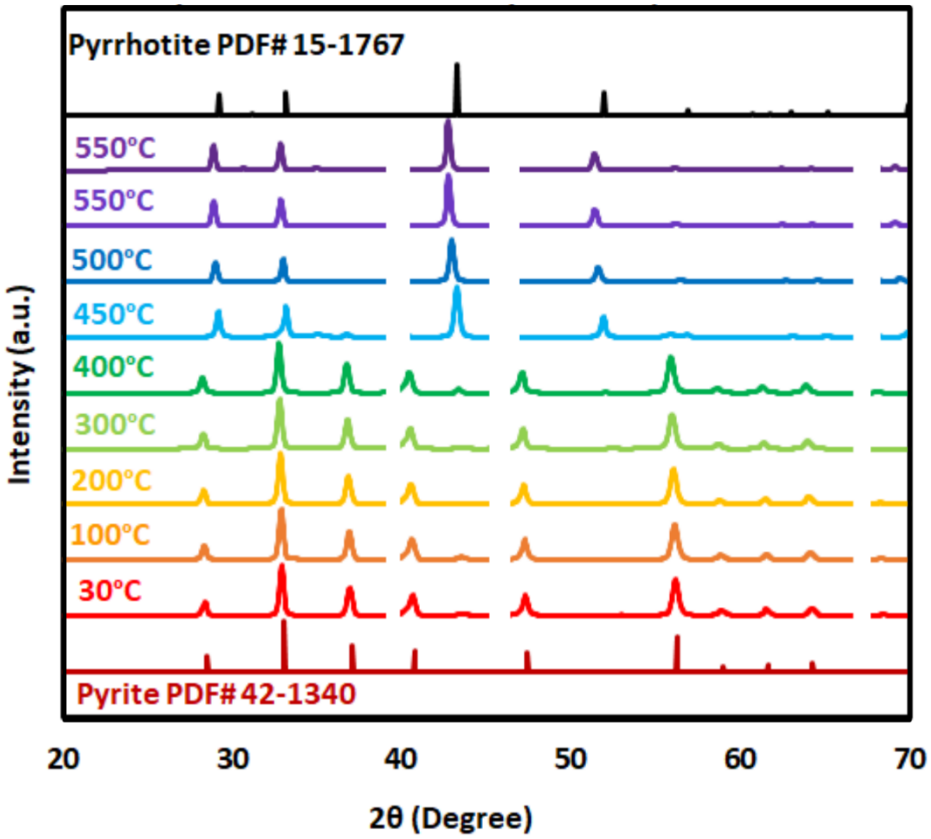

Figure 5.5: XRD patterns collected from 30°C to 550°C. The standards for pyrite and pyrrhotite are given. The Pt peaks have been removed from the spectrum.

Rietveld refinement, visible in section C3, fit the spectrum to (96.09± 0.58%) pyrite sample with a pyrrhotite impurity. The pyrrhotite impurity can be seen from the small peak near 43°C. Rietveld refinement found that the pyrite crystallites were 30.0 ± 0.2nm in size. As the cubes in reference [184] show cubes of a much larger size, it must be assumed that each particle contains multiple grains. Peak drift to more widely spaced planes was attributed to strain of thermal expansion.

As the temperature ramps up, the pyrite peaks vanish completely. By 550°C, the sample was composed 93.88 ± 3.1% pyrrhotite as found by the Rietveld refinement. Interestingly, as the sample shift to majority pyrrhotite, the reported pyrrhotite crystallite continues to grow to sizes even larger than the initial pyrite crystallites. This suggests annealing between pyrite crystallites.

Moehring demonstrated by in situ TEM that the overall shape of the particle does not change with the phase transformation. Furthermore, there is no distinctive core shell intermediate.

It is thought that the overall macroscopic change in shape (a shrinking of one dimension) is due to S sublimation.

5.3.4 Conclusions

In situ TEM and XRD demonstrate a phase change of cubic pyrite to hexagonal pyrrhotite upon heating. This phase change was seen to occur between 400°C and 450°C, a full 100°C to 150°C lower than reported values for bulk pyrite. 400°C is the operating temperature for FeS_2 cathodes. This indicates that this phase change is well within reach of high temperature batteries and must be considered deconvoluting the phase changes that occur. Beneficially, it is observed that the morphology does not shift dramatically at the relevant temperatures with this phase change, an important factor in technologies where the sample strain already does tremendous damage.

Chapter 6: Conclusion

6.1 Summary

The world's power output needs to double within the next 25 years. The production of this power needs to be done in a renewable fashion to avoid climate catastrophe and nuclear power is not a sufficient method. The sun provides orders of magnitude more energy than is needed to power the planet, even in the coming centuries. There are many ways to harvest solar energy. Dye-sensitized solar cells, splitting water into H_2, and iron pyrite-based solar cells all have tremendous potential. There are aspects of these technologies that must be improved before they can compete with fossil fuel technologies in terms of cost, convenience, and reliability. This thesis is a contribution to the understanding of the materials involved in these mechanisms and a roadmap of what must be done to improve them.

In chapter 2, an overview of quantum dots, Marcus theory of charge transfer, dye-sensitized solar cells, and photocatalytic water splitting is given. Quantum dots are an incredible discovery that have been utilized in a wide variety of fields. Their functionality comes from the ability to tune their size and subsequently their optical and electrical properties. Marcus theory is a powerful tool to describe charge transfer. While Marcus theory is highly accurate in the case of molecules, it does

not adequately describe charge transfer between nanoparticles and molecules. Auger-assisted charge transfer allows for the reduction in the reorganization energy to be used without fear of the inverted region. Dye sensitized solar cells represent a significant development in attempts to utilize solar energy. They can be made with a wide variety of different natural materials, are non-toxic, inexpensive, translucent, and have complementary properties to traditional silicon solar cells. They have grown significantly more efficient, in part due to the switch to using cobalt redox mediators, in particular $[Co(bipy)_3]^{3/2+}$. It was theorized that the internal reorganization energy of $[Co(bipy)_3]^{3/2+}$ was largely to blame for the efficiency only reaching 12%. This is a distinct possibility since the reorganization energy of $[Co(bipy)_3]^{3/2+}$ meant that with the driving force described the transfer kinetics are still far in the normal regime. Attempts to avoid the spin transition partially contributing to the high reorganization energy has led researchers to use $[Cu(dmp)_2]^{1/2+}$ and other copper complexes. A brief discussion of photocatalytically splitting water to produce hydrogen is given. While the field has made the tremendous leap to 100% efficiency, the rate limiting step of this process remains transferring the hole out of the structure. Several methods have been used to attempt to speed this process including using metal redox mediators and altering the number of monolayers passivating the core structure.

Chapter 3 examines how changing the reorganization energy of redox mediators controlled charge transfer rates. This was accomplished by using three cobalt complexes with similar reduction potentials but wildly different reorganization energies. A model was constructed using Marcus theory demonstrating that two of the complexes, $[Co(en)_3]^{3/2+}$ and $[Co(sep)]^{3/2+}$, were both still in the normal region while only the $[Co(ClMeN_3S_3sar)]^{3/2+}$ was in the barrierless region. The complexes were titrated into solutions of quantum dots which were observed via steady state fluorescence and time-resolved luminescence. Steady state fluorescence, evaluated via Stern-Volmer, demonstrated that the $[Co(ClMeN_3S_3sar)]^{3/2+}$ quenched the green emitting QDs 10 times more than $[Co(sep)]^{3/2+}$ and 60 times more strongly than $[Co(en)_3]^{3/2+}$. $[Co(ClMeN_3S_3sar)]^{3/2+}$ quenched the red emitting QDs ~260 times more strongly than $[Co(sep)]^{3/2+}$ and ~338 times more than $[Co(en)_3]^{3/2+}$. Forster resonant energy was disproven as the mechanism for this quench. Nanosecond lifetimes demonstrated that for the $[Co(ClMeN_3S_3sar)]^{3/2+}$, new sub-nanosecond lifetimes were emerging. We observed that the $[Co(ClMeN_3S_3sar)]^{3/2+}$ outperformed what was expected from simple Marcus theory, suggesting that perhaps Auger-assisted transfer was occurring.

Chapter 4 examines the “fool’s gold” material pyrite. An in-depth historical evaluation is done examining the early successes of the field and the subsequent failure to produce a working

cell. Despite measured properties that would seem ideal for producing an inexpensive and efficient solar cell, research has yet to produce an efficiency higher than 3%. A recent attempt to use a variety of different cell architectures by Steinhagen et al. showed an efficiency of 0%. The lack of production is determined to be from a low V_{OC} coming from degenerate levels of doping within the cell. The role of defects is unclear as the stoichiometry described could certainly lead to the carrier concentrations described, yet the trend linking poor stoichiometry with low photovoltage is not distinct. The surface seemed likely to contribute to the lacking photovoltage, especially as early successful cells had a surface etching treatment done prior to producing any photovoltage. Attempts were made to use ligands to alter the surface photovoltage to little effect, although TOPO seemed to at least stabilize the surface. The marcasite phase has been poorly understood and is likely not contributing to the photovoltage problem. Pyrrhotite in particular is much more detrimental to performance than marcasite. It seems likely that the difference in the fundamental and optical band gaps are significant. Transient reflection has measured carriers around 0.58eV, significantly below the reported 0.95eV. Current measurements find that there is a buried junction due to a large number of bulk defects. This junction occurs within 10nm of the surface and has a small barrier height. The use of diallyl disulfide allowed for a direct colloidal route to formation of FeS_2 without passing through FeS. Iron pyrite has found applications in both batteries and dye-sensitized solar cells.

Chapter 5 discussed attempts to use unsymmetric disulfides to improve the surface of iron pyrite. Unsymmetric disulfide is synthesized and applied to pyrrhotite cubes. The exchange is monitored by ATR and NMR. ATR results seemed to indicate the instead of the S-S-phenyl ideally coordinated to the surface there was instead an allyl group still present. NMR showed that oleylamine was unlikely to still be on the crystal surface due to the lack of the vanillin peak. TEM and STEM-EDS showed the cubes apparently being consumed during the exchange process. Chapter 5 also used in situ XRD to examine the phase change of iron pyrite to pyrrhotite showing that it is lower for nanocrystalline materials than earlier supposed by more than 100°C.

6.2 Future Directions and Outlook

The need to create more mechanisms of charge extraction is unavoidable. Chapter 3 focused on electron transfer, but the charge that must be extracted faster is the hole. In dye-sensitized solar cells, the hole has been seen to transfer as much as five orders of magnitude more slowly than the electron. In hole transfer from nanocrystal semiconductor photocatalysts the hole is seen to leave

three to four orders of magnitude more slowly than the electron. Altering the driving force does speed up charge transfer, but at the cost of usable photovoltage. It should be determined if altering reorganization energy is similarly impactful for hole transfer. After discovering whether reorganization energy impacts hole transfer, it will be possible to implement this knowledge in ligand cage design to make better redox mediators.

An iron pyrite photovoltaic cell would be unparalleled in terms of cost and material abundance. The past ten years have seen some of the issues understood. To make photovoltaic iron pyrite, there must be a method to mitigate the formation of intrinsic bulk states. For nanocrystalline and polycrystalline films, some method of overcoming surface defect states at grain boundaries is required. In the absence of such a method, the recombination and annihilation at grain boundaries is too high. The use of allyl disulfide does eliminate one method of forming intrinsic bulk defects, but there are still a degenerate number of carriers. New synthetic techniques are necessary to avoid forming bulk defects. Standard XRD and TEM do not do an adequate job in finding these defects, And hence finding a method more available than a synchrotron or ultrafast measurement system to test for these defects is a necessity for continuing pyrite research.

The need to increase charge transfer rates in nanocrystalline semiconducting materials is clear. The route to using reorganization energy to increase electron transfer rates has been shown; the effect of reorganization energy on hole transfer is the route now to be charted. Dye sensitized cells and hydrogen generation by water splitting have enormous potential; the impact speeding up hole transfer would make the dream of renewable energy by these technologies much more a reality.

The jury is still out on whether pyrite can ever realize its full potential. The promise of a solar material that is so abundant, nontoxic, and inexpensive is enough to have kept researchers trying to solve the technical problems preventing it's widespread application for forty years. The new uses of pyrite, as a battery cathode and as a counter electrode in dye-sensitized cell, are a wonderful readaptation of this incredible material. The hope, though, remains.

References

(1) Alfonso, D. R. Computational Investigation of FeS 2 Surfaces and Prediction of Effects of Sulfur Environment on Stabilities. **2010**, 8971–8980. https://doi.org/10.1021/jp100578n.

(2) Lewis, S. Nathan (Division of Chemistry and Chemical Engineering, C. I. of T.; Nocera, Daniel G (Department of Chemistry, M. I. of T. Powering the Planet: Chemical Challenges in Solar Energy Utilization. *Proceedings of the National Academy of Science* **2006**, *103* (43), 15729–15735. https://doi.org/10.1073/pnas.0603395103.

(3) Peter, L. M. Towards Sustainable Photovoltaics : The Search. *Philosphical Transactions of the Royal Society A* **2011**, *369*, 1840–1856. https://doi.org/10.1098/rsta.2010.0348.

(4) Wadia, C.; Alivisatos, A. P.; Kammen, D. M. Materials Availability Expands the Opportunity for Large-Scale Photovoltaics Deployment. *Environ Sci Technol* **2009**, *43* (6), 2072–2077.

(5) Hueso, K. B.; Armand, M.; Rojo, T. High Temperature Sodium Batteries: Status, Challenges and Future Trends. *Energy and Environmental Science*. March 2013, pp 734–749. https://doi.org/10.1039/c3ee24086j.

(6) Binetti, S.; Acciarri, M.; Donne, A. le; Morgano, M.; Jestin, Y. Key Success Factors and Future Perspective of Silicon-Based Solar Cells. **2013**, *2013*.

(7) Yoshikawa, K.; Kawasaki, H.; Yoshida, W.; Irie, T.; Konishi, K.; Nakano, K.; Uto, T.; Adachi, D.; Kanematsu, M.; Uzu, H.; Yamamoto, K. Silicon Heterojunction Solar Cell with Interdigitated Back Contacts for a Photoconversion Efficiency over 26%. *Nat Energy* **2017**, *2* (5). https://doi.org/10.1038/nenergy.2017.32.

(8) Woodhouse, M.; Smith, B.; Ramdas, A.; Margolis, R.; Woodhouse, M.; Smith, B.; Ramdas, A.; Margolis, R. Crystalline Silicon Photovoltaic Module Manufacturing Costs and Sustainable Pricing : 1H 2018 Benchmark and Cost Reduction Road Map Crystalline Silicon Photovoltaic Module Manufacturing Costs and Sustainable Pricing : 1H 2018 Benchmark and Cost Reduction . **2020**, No. February.

(9) Eftekhari, A. On the Theoretical Capacity/Energy of Lithium Batteries and Their Counterparts. *ACS Sustain Chem Eng* **2019**, *7* (4), 3684–3687. https://doi.org/10.1021/acssuschemeng.7b04330.

(10) Mirabi, E.; Akrami Abarghuie, F.; Arazi, R. Integration of Buildings with Third-Generation Photovoltaic Solar Cells: A Review. *Clean Energy* **2021**, *5*, 505–526. https://doi.org/10.1093/ce/zkab051.

(11) Cressler, J. D. *Silicon Earth*; Cambridge University Press: New York, 2009.

(12) Eustis, S.; El-Sayed, M. A. Why Gold Nanoparticles Are More Precious than Pretty Gold: Noble Metal Surface Plasmon Resonance and Its Enhancement of the Radiative and Nonradiative Properties of Nanocrystals of Different Shapes. *Chem Soc Rev* **2006**, *35* (3), 209–217. https://doi.org/10.1039/b514191e.

(13) Kovalenko, M. v.; Manna, L.; Cabot, A.; Hens, Z.; Talapin, D. v.; Kagan, C. R.; Klimov, V. I.; Rogach, A. L.; Reiss, P.; Milliron, D. J.; Guyot-Sionnnest, P.; Konstantatos, G.; Parak, W. J.; Hyeon, T.; Korgel, B. A.;

Murray, C. B.; Heiss, W. Prospects of Nanoscience with Nanocrystals. *ACS Nano* **2015**, *9* (2), 1012–1057. https://doi.org/10.1021/nn506223h.

(14) García de Arquer, F. P.; Talapin, D. v.; Klimov, V. I.; Arakawa, Y.; Bayer, M.; Sargent, E. H. Semiconductor Quantum Dots: Technological Progress and Future Challenges. *Science* **2021**, *373* (6555). https://doi.org/10.1126/science.aaz8541.

(15) Efros, Al. L.; Rosen, M. The Electronic Structure of Semiconductor Nanocrystals. *Annual Review of Materials Science* **2000**, *30*, 475–521.

(16) Konstantatos, G.; Sargent, E. H. *Colloidal Quantum Dot Optoelectronics and Photovoltaics*; Cambridge University Press: New York, 2013.

(17) Piryatinski, A.; Ivanov, S. A.; Tretiak, S.; Klimov, V. I. Effect of Quantum and Dielectric Confinement on the Exciton-Exciton Interaction Energy in Type II Core/Shell Semiconductor Nanocrystals. *Nano Lett* **2007**, *7* (1), 108–115. https://doi.org/10.1021/nl0622404.

(18) Klimov, V. I.; Mikhailovsky, A. A.; Xu, S.; Malko, A.; Hollingsworth, J. A.; Leatherdale, C. A.; Eisler, H. J.; Bawendi, M. G. Optical Gain and Stimulated Emission in Nanocrystal Quantum Dots. *Science (1979)* **2000**, *290* (5490), 314–317. https://doi.org/10.1126/science.290.5490.314.

(19) Klimov, V. I. Mechanisms for Photogeneration and Recombination of Multiexcitons in Semiconductor Nanocrystals: Implications for Lasing and Solar Energy Conversion. *Journal of Physical Chemistry B* **2006**, *110* (34), 16827–16845. https://doi.org/10.1021/jp0615959.

(20) Ruland, A.; Schulz-Drost, C.; Sgobba, V.; Guldi, D. M. Enhancing Photocurrent Efficiencies by Resonance Energy Transfer in CdTe Quantum Dot Multilayers: Towards Rainbow Solar Cells. *Advanced Materials* **2011**, *23* (39), 4573–4577. https://doi.org/10.1002/adma.201101423.

(21) Coropceanu, I.; Bawendi, M. G. Core/Shell Quantum Dot Based Luminescent Solar Concentrators with Reduced Reabsorption and Enhanced Efficiency. *Nano Lett* **2014**, *14* (7), 4097–4101. https://doi.org/10.1021/nl501627e.

(22) Hoffman, J. B.; Choi, H.; Kamat, P. v. Size-Dependent Energy Transfer Pathways in CdSe Quantum Dot-Squaraine Light-Harvesting Assemblies: Förster versus Dexter. *Journal of Physical Chemistry C* **2014**, *118* (32), 18453–18461. https://doi.org/10.1021/jp506757a.

(23) Wu, K.; Lian, T. Quantum Confined Colloidal Nanorod Heterostructures for Solar-to-Fuel Conversion. *Chem Soc Rev* **2016**, *45* (14), 3781–3810. https://doi.org/10.1039/c5cs00472a.

(24) Burke, R.; Bren, K. L.; Krauss, T. D. Semiconductor Nanocrystal Photocatalysis for the Production of Solar Fuels. *Journal of Chemical Physics* **2021**, *154* (3), 1–19. https://doi.org/10.1063/5.0032172.

(25) Liu, C.; Qiu, F.; Peterson, J. J.; Krauss, T. D. Aqueous Photogeneration of H2 with CdSe Nanocrystals and Nickel Catalysts: Electron Transfer Dynamics. *Journal of Physical Chemistry B* **2015**, *119* (24), 7349–7357. https://doi.org/10.1021/jp510935w.

(26) Cogan, N. M. B.; Liu, C.; Qiu, F.; Burke, R.; Krauss, T. D. Ultrafast Dynamics of Colloidal Semiconductor Nanocrystals Relevant to Solar Fuels Production. *Ultrafast Bandgap Photonics II* **2017**, *10193* (May 2017), 101930B. https://doi.org/10.1117/12.2262168.

(27) Lv, H.; Wang, C.; Li, G.; Burke, R.; Krauss, T. D.; Gao, Y.; Eisenberg, R. Semiconductor Quantum Dot-Sensitized Rainbow Photocathode for Effective Photoelectrochemical Hydrogen Generation. *Proc Natl Acad Sci U S A* **2017**, *114* (43), 11297–11302. https://doi.org/10.1073/pnas.1712325114.

(28) Burke, R.; Chakraborty, S.; McClelland, K. P.; Jelušić, J.; Matson, E. M.; Bren, K. L.; Krauss, T. D. Light-Driven Hydrogen Production with CdSe Quantum Dots and a Cobalt Glutathione Catalyst. *Chemical Communications* **2021**, *57* (16), 2053–2056. https://doi.org/10.1039/d0cc07364d.

(29) Hildebrandt, N.; Spillmann, C. M.; Russ Algar, W.; Pons, T.; Stewart, M. H.; Oh, E.; Susumu, K.; Díaz, S. A.; Delehanty, J. B.; Medintz, I. L. Energy Transfer with Semiconductor Quantum Dot Bioconjugates: A Versatile Platform for Biosensing, Energy Harvesting, and Other Developing Applications. *Chem Rev* **2017**, *117* (2), 536–711. https://doi.org/10.1021/acs.chemrev.6b00030.

(30) Clapp, A. R.; Medintz, I. L.; Mauro, J. M.; Fisher, B. R.; Bawendi, M. G.; Mattoussi, H. Fluorescence Resonance Energy Transfer between Quantum Dot Donors and Dye-Labeled Protein Acceptors. *J Am Chem Soc* **2004**, *126* (1), 301–310. https://doi.org/10.1021/ja037088b.

(31) Peterson, M. D.; Holbrook, R. J.; Meade, T. J.; Weiss, E. A. Photoinduced Electron Transfer from PbS Quantum Dots to Cobalt(III) Schiff Base Complexes: Light Activation of a Protein Inhibitor. *J Am Chem Soc* **2013**, *135* (35), 13162–13167. https://doi.org/10.1021/ja4065393.

(32) Snee, P. T.; Somers, R. C.; Nair, G.; Zimmer, J. P.; Bawendi, M. G.; Nocera, D. G. A Ratiometric CdSe/ZnS Nanocrystal PH Sensor. *J Am Chem Soc* **2006**, *128* (41), 13320–13321. https://doi.org/10.1021/ja0618999.

(33) Jiang, Y.; Weiss, E. A. Colloidal Quantum Dots as Photocatalysts for Triplet Excited State Reactions of Organic Molecules. *J Am Chem Soc* **2020**, *142* (36), 15219–15229. https://doi.org/10.1021/jacs.0c07421.

(34) Harris, R. D.; Bettis Homan, S.; Kodaimati, M.; He, C.; Nepomnyashchii, A. B.; Swenson, N. K.; Lian, S.; Calzada, R.; Weiss, E. A. Electronic Processes within Quantum Dot-Molecule Complexes. *Chem Rev* **2016**, *116* (21), 12865–12919. https://doi.org/10.1021/acs.chemrev.6b00102.

(35) Rossetti, R.; Nakahara, S.; Brus, L. E. Quantum Size Effects in the Redox Potentials, Resonance Raman Spectra, and Electronic Spectra of CdS Crystallites in Aqueous Solution. *J Chem Phys* **1983**, *79* (2), 1086–1088. https://doi.org/10.1063/1.445834.

(36) Brus, L. Electronic Wave Functions in Semiconductor Clusters: Experiment and Theory. *Journal of Physical Chemistry* **1986**, *90* (12), 2555–2560. https://doi.org/10.1021/j100403a003.

(37) Goldstein, L.; Glas, F.; Marzin, J. Y.; Charasse, M. N.; le Roux, G. Growth by Molecular Beam Epitaxy and Characterization of InAs/GaAs Strained-Layer Superlattices. *Appl Phys Lett* **1985**, *47* (10), 1099–1101. https://doi.org/10.1063/1.96342.

(38) Oshinowo, J.; Nishioka, M.; Ishida, S.; Arakawa, Y. Highly Uniform InGaAs/GaAs Quantum Dots (~15 Nm) by Metalorganic Chemical Vapor Deposition. *Appl Phys Lett* **1994**, *65* (11), 1421–1423. https://doi.org/10.1063/1.112070.

(39) Sowers, K. L.; Hou, Z.; Peterson, J. J.; Swartz, B.; Pal, S.; Prezhdo, O.; Krauss, T. D. Photophysical Properties of CdSe/CdS Core/Shell Quantum Dots with Tunable Surface Composition. *Chem Phys* **2016**, *471*, 24–31. https://doi.org/10.1016/j.chemphys.2015.09.010.

(40) Orfield, N. J.; Majumder, S.; McBride, J. R.; Yik-Ching Koh, F.; Singh, A.; Bouquin, S. J.; Casson, J. L.; Johnson, A. D.; Sun, L.; Li, X.; Shih, C. K.; Rosenthal, S. J.; Hollingsworth, J. A.; Htoon, H. Photophysics of Thermally-Assisted Photobleaching in "Giant" Quantum Dots Revealed in Single Nanocrystals. *ACS Nano* **2018**, *12* (5), 4206–4217. https://doi.org/10.1021/acsnano.7b07450.

(41) Shirasaki, Y.; Supran, G. J.; Bawendi, M. G.; Bulović, V. Emergence of Colloidal Quantum-Dot Light-Emitting Technologies. *Nat Photonics* **2013**, *7* (1), 13–23. https://doi.org/10.1038/nphoton.2012.328.

(42) Wang, X.; Ren, X.; Kahen, K.; Hahn, M. A.; Rajeswaran, M.; MacCagnano-Zacher, S.; Silcox, J.; Cragg, G. E.; Efros, A. L.; Krauss, T. D. Non-Blinking Semiconductor Nanocrystals. *Nature* **2009**, *459* (7247), 686–689. https://doi.org/10.1038/nature08072.

(43) Krauss, T. D.; Peterson, J. J. Quantum Dots: A Charge for Blinking. *Nat Mater* **2012**, *11* (1), 14–16. https://doi.org/10.1038/nmat3206.

(44) Zhao, J.; Chen, O.; Strasfeld, D. B.; Bawendi, M. G. Biexciton Quantum Yield Heterogeneities in Single CdSe (CdS) Core (Shell) Nanocrystals and Its Correlation to Exciton Blinking. *Nano Lett* **2012**, *12* (9), 4477–4483. https://doi.org/10.1021/nl3013727.

(45) Garrett, M. D.; Dukes, A. D.; McBride, J. R.; Smith, N. J.; Pennycook, S. J.; Rosenthal, S. J. Band Edge Recombination in CdSe, CdS and CdSxSe1-x Alloy Nanocrystals Observed by Ultrafast Fluorescence Upconversion: The Effect of Surface Trap States. *Journal of Physical Chemistry C* **2008**, *112* (33), 12736–12746. https://doi.org/10.1021/jp803708r.

(46) Orfield, N. J.; McBride, J. R.; Wang, F.; Buck, M. R.; Keene, J. D.; Reid, K. R.; Htoon, H.; Hollingsworth, J. A.; Rosenthal, S. J. Quantum Yield Heterogeneity among Single Nonblinking Quantum Dots Revealed by Atomic Structure-Quantum Optics Correlation. *ACS Nano* **2016**, *10* (2), 1960–1968. https://doi.org/10.1021/acsnano.5b05876.

(47) Bowers, M. J.; McBride, J. R.; Garrett, M. D.; Sammons, J. A.; Dukes, A. D.; Schreuder, M. A.; Watt, T. L.; Lupini, A. R.; Pennycook, S. J.; Rosenthal, S. J. Structure and Ultrafast Dynamics of White-Light-Emitting CdSe Nanocrystals. *J Am Chem Soc* **2009**, *131* (16), 5730–5731. https://doi.org/10.1021/ja900529h.

(48) Marcus, R. A.; Sutin, N. Electron Transfers in Chemistry and Biology. *Biochim Biophys Acta* **1985**, *811* (86127), 265–322. https://doi.org/https://doi.org/10.1016/0304-4173(85)90014-X.

(49) Marcus, R. A. On the Theory of Electron-Transfer Reactions. VI. Unified Treatment for Homogeneous and Electrode Reactions. *J Chem Phys* **1965**, *43* (2), 679–701. https://doi.org/10.1063/1.1696792.

(50) Marcus, R. A. Electron Transfer Reactions in Chemistry: Theory and Experiment (Nobel Lecture). *Angewandte Chemie International Edition in English* **1993**, *32* (8), 1111–1121. https://doi.org/10.1002/anie.199311113.

(51) Chou, M.; Creutz, C.; Sutin, N. Rate Constants and Activation Parameters for Outer-Sphere Electron-Transfer Reactions and Comparisons with the Predictions of Marcus Theory. *J Am Chem Soc* **1977**, *99* (17), 5615–5623. https://doi.org/10.1021/ja00459a014.

(52) Zhu, H.; Yang, Y.; Hyeon-Deuk, K.; Califano, M.; Song, N.; Wang, Y.; Zhang, W.; Prezhdo, O. v.; Lian, T. Auger-Assisted Electron Transfer from Photoexcited Semiconductor Quantum Dots. *Nano Lett* **2014**, *14* (3), 1263–1269. https://doi.org/10.1021/nl4041687.

(53) Ding, T. X.; Olshansky, J. H.; Leone, S. R.; Alivisatos, A. P. Efficiency of Hole Transfer from Photoexcited Quantum Dots to Covalently Linked Molecular Species. *J Am Chem Soc* **2015**, *137* (5), 2021–2029. https://doi.org/10.1021/ja512278a.

(54) Olshansky, J. H.; Ding, T. X.; Lee, Y. v.; Leone, S. R.; Alivisatos, A. P. Hole Transfer from Photoexcited Quantum Dots: The Relationship between Driving Force and Rate. *J Am Chem Soc* **2015**, *137* (49), 15567–15575. https://doi.org/10.1021/jacs.5b10856.

(55) Wongcharee, K.; Meeyoo, V.; Chavadej, S. Dye-Sensitized Solar Cell Using Natural Dyes Extracted from Rosella and Blue Pea Flowers. *Solar Energy Materials and Solar Cells* **2007**, *91* (7), 566–571. https://doi.org/10.1016/j.solmat.2006.11.005.

(56) Yuan, Y.; Wan, C. Dual Application of Waste Grape Skin for Photosensitizers and Counter Electrodes of Dye-Sensitized Solar Cells. *Nanomaterials* **2022**, *12* (3). https://doi.org/10.3390/nano12030563.

(57) Narayan, M. R. Review: Dye Sensitized Solar Cells Based on Natural Photosensitizers. *Renewable and Sustainable Energy Reviews* **2012**, *16* (1), 208–215. https://doi.org/10.1016/j.rser.2011.07.148.

(58) Miettunen, K.; Vapaavuori, J.; Poskela, A.; Tiihonen, A.; Lund, P. D. Recent Progress in Flexible Dye Solar Cells. *Wiley Interdiscip Rev Energy Environ* **2018**, *7* (5), 1–11. https://doi.org/10.1002/wene.302.

(59) Miettunen, K.; Halme, J.; Lund, P. Metallic and Plastic Dye Solar Cells. *Wiley Interdiscip Rev Energy Environ* **2013**, *2* (1), 104–120. https://doi.org/10.1002/wene.46.

(60) O'Regan, B.; Graetzel, M. A Low-Cost, High-Efficiency Solar Cell Based on Dye-Sensitized Colloidal TiO2 Films. *Nature* **1991**, *353*, 737–740.

(61) Baxter, J. B. Commercialization of Dye Sensitized Solar Cells: Present Status and Future Research Needs to Improve Efficiency, Stability, and Manufacturing. *Journal of Vacuum Science & Technology A: Vacuum, Surfaces, and Films* **2012**, *30* (2), 020801. https://doi.org/10.1116/1.3676433.

(62) Dubey, S.; Sarvaiya, J. N.; Seshadri, B. Temperature Dependent Photovoltaic (PV) Efficiency and Its Effect on PV Production in the World - A Review. *Energy Procedia* **2013**, *33*, 311–321. https://doi.org/10.1016/j.egypro.2013.05.072.

(63) Sharma, K.; Sharma, V.; Sharma, S. S. Dye-Sensitized Solar Cells: Fundamentals and Current Status. *Nanoscale Res Lett* **2018**, *13*. https://doi.org/10.1186/s11671-018-2760-6.

(64) Jung, H. S.; Lee, J. K. Dye Sensitized Solar Cells for Economically Viable Photovoltaic Systems. *Journal of Physical Chemistry Letters* **2013**, *4* (10), 1682–1693. https://doi.org/10.1021/jz400112n.

(65) Kroon, J. M.; Bakker, N. J.; Smit, H. J. P.; Liska, P.; Thampi, K. R.; Wang, P.; Zakeeruddin, S. M.; Gr{\"a}tzel, M.; Hinsch, A.; Hore, S.; W{\"u}rfel, U.; Sastrawan, R.; Durrant, J. R.; Palomares, E.; Pettersson, H.; Gruszecki, T.; Walter, J.; Skupien, K.; Tulloch, G. E. Nanocrystalline Dye-Sensitized Solar Cells Having Maximum Performance. *Progress in Photovoltaics: Research and Applications* **2007**, *15*, 1–18. https://doi.org/10.1002/pip.707.

(66) TRIBUTSCH, H.; CALVIN, M. Electrochemistry of Excited Molecules: Photo-Electrochemical Reactions of Chlorophylls. *Photochem Photobiol* **1971**, *14* (2), 95–112. https://doi.org/10.1111/j.1751-1097.1971.tb06156.x.

(67) Bella, F.; Gerbaldi, C.; Barolo, C.; Grätzel, M. Aqueous Dye-Sensitized Solar Cells. *Chemical Society Reviews*. Royal Society of Chemistry June 7, 2015, pp 3431–3473. https://doi.org/10.1039/c4cs00456f.

(68) Xiang, W.; Huang, F.; Cheng, Y. B.; Bach, U.; Spiccia, L. Aqueous Dye-Sensitized Solar Cell Electrolytes Based on the Cobalt(Ii)/(Iii) Tris(Bipyridine) Redox Couple. *Energy Environ Sci* **2013**, *6* (1), 121–127. https://doi.org/10.1039/c2ee23317g.

(69) Byne, O.; Coughlan, A.; Surolia, P. K.; Thampi, R. K. Succinonitrile-Based Solid-State Electrolytes for Dye-Sensitised Solar Cells. *Progress in Photovoltaics: Research and Applications* **2013**, *23*, 417–427. https://doi.org/10.1002/pip.2441.

(70) Hamann, T. W.; Jensen, R. A.; Martinson, A. B. F.; van Ryswyk, H.; Hupp, J. T. Advancing beyond Current Generation Dye-Sensitized Solar Cells. *Energy Environ Sci* **2008**, *1* (1), 66–78. https://doi.org/10.1039/b809672d.

(71) Xie, Y.; Hamann, T. W. Fast Low-Spin Cobalt Complex Redox Shuttles for Dye-Sensitized Solar Cells. *Journal of Physical Chemistry Letters* **2013**, *4* (2), 328–332. https://doi.org/10.1021/jz301934e.

(72) Miettunen, K.; Saukkonen, T.; Li, X.; Law, C.; Sheng, Y. K.; Halme, J.; Tiihonen, A.; Barnes, P. R. F.; Ghaddar, T.; Asghar, I.; Lund, P.; O'Regan, B. C. Do Counter Electrodes on Metal Substrates Work with Cobalt Complex Based Electrolyte in Dye Sensitized Solar Cells? *J Electrochem Soc* **2013**, *160* (2), H132–H137. https://doi.org/10.1149/2.074302jes.

(73) Miettunen, K.; Jouttijärvi, S.; Jiang, R.; Saukkonen, T.; Romu, J.; Halme, J.; Lund, P. Low Cost Ferritic Stainless Steel in Dye Sensitized Solar Cells with Cobalt Complex Electrolyte. *J Electrochem Soc* **2014**, *161* (3), H138–H143. https://doi.org/10.1149/2.054403jes.

(74) Iftikhar, H.; Sonai, G. G.; Hashmi, S. G.; Nogueira, A. F.; Lund, P. D. *Progress on Electrolytes Development in Dye-Sensitized Solar Cells*; 2019; Vol. 12. https://doi.org/10.3390/ma12121998.

(75) Cao, Y.; Saygili, Y.; Ummadisingu, A.; Teuscher, J.; Luo, J.; Pellet, N.; Giordano, F.; Zakeeruddin, S. M.; Moser, J. E.; Freitag, M.; Hagfeldt, A.; Grätzel, M. 11% Efficiency Solid-State Dye-Sensitized Solar Cells with Copper(II/I) Hole Transport Materials. *Nat Commun* **2017**, *8*, 1–8. https://doi.org/10.1038/ncomms15390.

(76) Fujishima, Akira (Department of Applied Chemistry, Kanagawa University, Y.; Honda, Kenichi(Institute of Industrial Science, University of Tokyo, Roppongi, T. Electrochemical Photolysis of Water at a Semiconductor Electrode. *Nature* **1972**, *238* (5358), 38–40. https://doi.org/10.1038/238038a0.

(77) Chen, X.; Shen, S.; Guo, L.; Mao, S. S. Semiconductor-Based Photocatalytic Hydrogen Generation. *Chem Rev* **2010**, *110* (11), 6503–6570. https://doi.org/10.1021/cr1001645.

(78) Kalisman, P.; Nakibli, Y.; Amirav, L. Perfect Photon-to-Hydrogen Conversion Efficiency. *Nano Lett* **2016**, *16* (3), 1776–1781. https://doi.org/10.1021/acs.nanolett.5b04813.

(79) Amirav, L.; Alivisatos, A. P. Photocatalytic Hydrogen Production with Tunable Nanorod Heterostructures. *Journal of Physical Chemistry Letters* **2010**, *1* (7), 1051–1054. https://doi.org/10.1021/jz100075c.

(80) Kalisman, P.; Amirav, L. Improved Efficiency and Stability of Cadmium Chalcogenide Nanoparticles by Photodeposition of Co-Catalysts. *MRS Adv* **2016**, *1* (59), 3923–3927. https://doi.org/10.1557/adv.2016.239.

(81) Wu, K.; Zhu, H.; Lian, T. Ultrafast Exciton Dynamics and Light-Driven H2 Evolution in Colloidal Semiconductor Nanorods and Pt-Tipped Nanorods. *Acc Chem Res* **2015**, *48* (3), 851–859. https://doi.org/10.1021/ar500398g.

(82) Gimbert-Suriñach, C.; Albero, J.; Stoll, T.; Fortage, J.; Collomb, M. N.; Deronzier, A.; Palomares, E.; Llobet, A. Efficient and Limiting Reactions in Aqueous Light-Induced Hydrogen Evolution Systems Using Molecular Catalysts and Quantum Dots. *J Am Chem Soc* **2014**, *136* (21), 7655–7661. https://doi.org/10.1021/ja501489h.

(83) la Croix, A. D.; O'Hara, A.; Reid, K. R.; Orfield, N. J.; Pantelides, S. T.; Rosenthal, S. J.; Macdonald, J. E. Design of a Hole Trapping Ligand. *Nano Lett* **2017**, *17* (2), 909–914. https://doi.org/10.1021/acs.nanolett.6b04213.

(84) Lian, S.; Weinberg, D. J.; Harris, R. D.; Kodaimati, M. S.; Weiss, E. A. Subpicosecond Photoinduced Hole Transfer from a CdS Quantum Dot to a Molecular Acceptor Bound Through an Exciton-Delocalizing Ligand. *ACS Nano* **2016**, *10* (6), 6372–6382. https://doi.org/10.1021/acsnano.6b02814.

(85) Veinot, J. G. C.; Galloro, J.; Pugliese, L.; Pestrin, R.; Pietro, W. J. Surface Functionalization of Cadmium Sulfide Quantum-Confined Nanoclusters. 5. Evidence of Facile Surface-Core Electronic Communication in the Photodecomposition Mechanism of Functionalized Quantum Dots. *Chemistry of Materials* **1999**, *11* (3), 642–648. https://doi.org/10.1016/j.solener.2011.06.020.

(86) Deng, Z.; Tseng, H. W.; Zong, R.; Wang, D.; Thummel, R. Preparation and Study of a Family of Dinuclear Ru(II) Complexes That Catalyze the Decomposition of Water. *Inorg Chem* **2008**, *47* (6), 1835–1848. https://doi.org/10.1021/ic7010875.

(87) O'Connor, T.; Panov, M. S.; Mereshchenko, A.; Tarnovsky, A. N.; Lorek, R.; Perera, D.; Diederich, G.; Lambright, S.; Moroz, P.; Zamkov, M. The Effect of the Charge-Separating Interface on Exciton Dynamics in Photocatalytic Colloidal Heteronanocrystals. *ACS Nano* **2012**, *6* (9), 8156–8165. https://doi.org/10.1021/nn302810y.

(88) Amirav, L.; Alivisatos, A. P. Luminescence Studies of Individual Quantum Dot Photocatalysts. *J Am Chem Soc* **2013**, *135* (35), 13049–13053. https://doi.org/10.1021/ja404918z.

(89) Sheng, W.; Gasteiger, H. A.; Shao-Horn, Y. Hydrogen Oxidation and Evolution Reaction Kinetics on Platinum: Acid vs Alkaline Electrolytes. *J Electrochem Soc* **2010**, *157* (11), B1529. https://doi.org/10.1149/1.3483106.

(90) Wu, K.; Chen, Z.; Lv, H.; Zhu, H.; Hill, C. L.; Lian, T. Hole Removal Rate Limits Photodriven H2 Generation Efficiency in CdS-Pt and CdSe/CdS-Pt Semiconductor Nanorod-Metal Tip Heterostructures. *J Am Chem Soc* **2014**, *136* (21), 7708–7716. https://doi.org/10.1021/ja5023893.

(91) Kalisman, P.; Kauffmann, Y.; Amirav, L. Photochemical Oxidation on Nanorod Photocatalysts. *J Mater Chem A Mater* **2015**, *3* (7), 3261–3265. https://doi.org/10.1039/c4ta06164k.

(92) Nakibli, Y.; Kalisman, P.; Amirav, L. Less Is More: The Case of Metal Cocatalysts. *Journal of Physical Chemistry Letters* **2015**, *6* (12), 2265–2268. https://doi.org/10.1021/acs.jpclett.5b00872.

(93) Koposov, A. Y.; Szymanski, P.; Cardolaccia, T.; Meyer, T. J.; Klimov, V. I.; Sykora, M. Electronic Properties and Structure of Assemblies of CdSe Nanocrystal Quantum Dots and Ru-Polypyridine Complexes Probed by Steady State and Time-Resolved Photoluminescence. *Adv Funct Mater* **2011**, *21* (16), 3159–3168. https://doi.org/10.1002/adfm.201100415.

(94) Han, Z.; Qiu, F.; Eisenberg, R.; Holland, P. L.; Krauss, T. D. Robust Photogeneration of H_2 in Water Using Semiconductor Nanocrystals and a Nickel Catalyst. *Science (1979)* **2012**, *338* (December), 1321–1324.

(95) Sykora, M.; Petruska, M. A.; Alstrum-Acevedo, J.; Bezel, I.; Meyer, T. J.; Klimov, V. I. Photoinduced Charge Transfer between CdSe Nanocrystal Quantum Dots and Ru-Polypyridine Complexes. *J Am Chem Soc* **2006**, *128* (31), 9984–9985. https://doi.org/10.1021/ja061556a.

(96) Burke, R.; Cogan, N. M. B.; Oi, A.; Krauss, T. D. Recovery of Active and Efficient Photocatalytic H2 Production for CdSe Quantum Dots. *Journal of Physical Chemistry C* **2018**, *122* (25), 14099–14106. https://doi.org/10.1021/acs.jpcc.8b01237.

(97) Weiss, E. A. Designing the Surfaces of Semiconductor Quantum Dots for Colloidal Photocatalysis. *ACS Energy Lett* **2017**, *2* (5), 1005–1013. https://doi.org/10.1021/acsenergylett.7b00061.

(98) Yin, J.; Cogan, N. M. B.; Burke, R.; Hou, Z.; Sowers, K. L.; Krauss, T. D. Size Dependence of Photocatalytic Hydrogen Generation for CdTe Quantum Dots. *Journal of Chemical Physics* **2019**, *151* (17), 1–8. https://doi.org/10.1063/1.5125000.

(99) Rosner, T.; Pavlopoulos, N. G.; Shoyhet, H.; Micheel, M.; Wächtler, M.; Adir, N.; Amirav, L. The Other Dimension—Tuning Hole Extraction via Nanorod Width. *Nanomaterials* **2022**, *12* (19), 1–10. https://doi.org/10.3390/nano12193343.

(100) Somers, R. C.; Bawendi, M. G.; Nocera, D. G. CdSe Nanocrystal Based Chem-/Bio- Sensors. *Chem Soc Rev* **2007**, *36* (4), 579–591. https://doi.org/10.1039/b517613c.

(101) Owen, J.; Brus, L. Chemical Synthesis and Luminescence Applications of Colloidal Semiconductor Quantum Dots. *J Am Chem Soc* **2017**, *139* (32), 10939–10943. https://doi.org/10.1021/jacs.7b05267.

(102) Xia, B. Y.; Yang, P.; Sun, Y.; Wu, Y.; Mayers, B.; Gates, B.; Yin, Y.; Kim, F.; Yan, H. One-Dimensional Nanostructures : Synthesis , Characterization , and Applications. *Advanced Materials* **2003**, *15* (5), 353–389.

(103) Wilker, M. B.; Schnitzenbaumer, K. J.; Dukovic, G. Recent Progress in Photocatalysis Mediated by Colloidal II-VI Nanocrystals. *Isr J Chem* **2012**, *52* (11–12), 1002–1015. https://doi.org/10.1002/ijch.201200073.

(104) He, F. M. C.; Bernhardt, P. v. Cobalt Cage Complexes as Mediators of Protein Electron Transfer. *Journal of Biological Inorganic Chemistry* **2017**, *22* (5), 775–788. https://doi.org/10.1007/s00775-016-1427-y.

(105) Ørnsø, K. B.; Jónsson, E. O.; Jacobsen, K. W.; Thygesen, K. S. Importance of the Reorganization Energy Barrier in Computational Design of Porphyrin-Based Solar Cells with Cobalt-Based Redox Mediators. *Journal of Physical Chemistry C* **2015**, *119* (23), 12792–12800. https://doi.org/10.1021/jp512627e.

(106) Sapp, S. A.; Elliott, C. M.; Contado, C.; Caramori, S.; Bignozzi, C. A. Substituted Polypyridine Complexes of Cobalt(II/III) as Efficient Electron-Transfer Mediators in Dye-Sensitized Solar Cells. *J Am Chem Soc* **2002**, *124* (37), 11215–11222. https://doi.org/10.1021/ja027355y.

(107) Han, K.; Wang, M.; Zhang, S.; Wu, S.; Yang, Y.; Sun, L. Photochemical Hydrogen Production from Water Catalyzed by CdTe Quantum Dots/Molecular Cobalt Catalyst Hybrid Systems. *Chemical Communications* **2015**, *51* (32), 7008–7011. https://doi.org/10.1039/c5cc00536a.

(108) Eckenhoff, W. T.; McNamara, W. R.; Du, P.; Eisenberg, R. Cobalt Complexes as Artificial Hydrogenases for the Reductive Side of Water Splitting. *Biochim Biophys Acta Bioenerg* **2013**, *1827* (8–9), 958–973. https://doi.org/10.1016/j.bbabio.2013.05.003.

(109) Bernhardt, P. v.; Jones, L. A. Electrochemistry of Macrocyclic Cobalt(III/II) Hexaamines: Electrocatalytic Hydrogen Evolution in Aqueous Solution. *Inorg Chem* **1999**, *38* (22), 5086–5090. https://doi.org/10.1021/ic981425d.

(110) Yu, W. W.; Qu, L.; Guo, W.; Peng, X. Experimental Determination of the Extinction Coefficient of CdTe, CdSe, and CdS Nanocrystals. *Chemistry of Materials* **2003**, *15* (14), 2854–2860. https://doi.org/10.1021/cm034081k.

(111) Feldt, S. M.; Wang, G.; Boschloo, G.; Hagfeldt, A. Effects of Driving Forces for Recombination and Regeneration on the Photovoltaic Performance of Dye-Sensitized Solar Cells Using Cobalt Polypyridine Redox Couples. *Journal of Physical Chemistry C* **2011**, *115* (43), 21500–21507. https://doi.org/10.1021/jp2061392.

(112) Yella, A.; Lee, H.-W.; Tsao, H. N.; Yi, C.; Chindrian, A. K.; Nazeeruddin, Md. K.; Diau, E. W.-G.; Yeh, C.-Y. Porphyrin-Sensitized Solar Cells with Cobalt (II/III)–Based Redox Electrolyte Exceed 12 Percent Efficiency. *Science (1979)* **2011**, *334* (6056), 629–633. https://doi.org/10.1126/science.1209688.

(113) Kashif, M. K.; Nippe, M.; Duffy, N. W.; Forsyth, C. M.; Chang, C. J.; Long, J. R.; Spiccia, L.; Bach, U. Stable Dye-Sensitized Solar Cell Electrolytes Based on Cobalt(II)/(III) Complexes of a Hexadentate Pyridyl Ligand. *Angewandte Chemie - International Edition* **2013**, *52* (21), 5527–5531. https://doi.org/10.1002/anie.201300070.

(114) Dubs, R. v.; Gahan, L. R.; Sargeson, A. M. Rapid Electron Self-Exchange Involving Low-Spin Cobalt(II) and Cobalt(III) in an Encapsulated Cage Complex. *Inorg Chem* **1983**, *22* (18), 2523–2527. https://doi.org/10.1021/ic00160a012.

(115) Tisdale, W. A.; Zhu, X. Y. Artificial Atoms on Semiconductor Surfaces. *Proc Natl Acad Sci U S A* **2011**, *108* (3), 965–970. https://doi.org/10.1073/pnas.1006665107.

(116) Zhao, H.; Li, Y.; Diao, L.; Sun, C.; Shi, Y. Reevaluating the Effects of Reorganization Energy on Electron Transfer Rate for Quantum Dot-Molecular Acceptor Complexes in Different Solvents. *Spectrochim Acta A Mol Biomol Spectrosc* **2019**, *218*, 237–242. https://doi.org/10.1016/j.saa.2019.04.016.

(117) Mau, A. W. H.; Sasse, W. H. F.; Sargeson, A. M. The Synthesis and Properties of Cobalt Cage Complexes with N_3S_3Donor Sets. *Aust J Chem* **1993**, *46* (5), 641–661. https://doi.org/10.1071/CH9930641.

(118) Jasieniak, J.; Califano, M.; Watkins, S. E. Size-Dependent Valence and Conduction Band-Edge Energies of Semiconductor Nanocrystals. *ACS Nano* **2011**, *5* (7), 5888–5902. https://doi.org/10.1021/nn201681s.

(119) Osvath, P.; Sargeson, A. M.; Skelton, B. W.; White, A. H. Cobalt(II) and Cobalt(III) Complexes of a Novel Homoleptic Thioether Cage. *J Chem Soc Chem Commun* **1991**, No. 15, 1036–1038. https://doi.org/10.1039/C39910001036.

(120) Endres, R. G.; LaBute, M. X.; Cox, D. L. Theory of Adiabatic Hexaamminecobalt Self-Exchange. *Journal of Chemical Physics* **2003**, *118* (19), 8706–8714. https://doi.org/10.1063/1.1567255.

(121) Zerk, T. J.; Saouma, C. T.; Mayer, J. M.; Tolman, W. B. Low Reorganization Energy for Electron Self-Exchange by a Formally Copper(III,II) Redox Couple. *Inorg Chem* **2019**, *58* (20), 14151–14158. https://doi.org/10.1021/acs.inorgchem.9b02185.

(122) Khalid, S.; Ahmed, E.; Khan, Y.; Riaz, K. N.; Malik, M. A. Nanocrystalline Pyrite for Photovoltaic Applications. *ChemistrySelect* **2018**, *3* (23), 6488–6524. https://doi.org/10.1002/slct.201800405.

(123) Xue, H.; Yu, D. Y. W.; Qing, J.; Yang, X.; Xu, J.; Li, Z.; Sun, M.; Kang, W.; Tang, Y.; Lee, C. S. Pyrite FeS2 Microspheres Wrapped by Reduced Graphene Oxide as High-Performance Lithium-Ion Battery Anodes. *J Mater Chem A Mater* **2015**, *3* (15), 7945–7949. https://doi.org/10.1039/c5ta00988j.

(124) Sorenson, S. A.; Patrow, J. G.; Dawlaty, J. M. Electronic Dynamics in Natural Iron Pyrite Studied by Broadband Transient Reflection Spectroscopy. *Journal of Physical Chemistry C* **2016**, *120* (14), 7736–7747. https://doi.org/10.1021/acs.jpcc.5b11036.

(125) Shockley, W.; Queisser, H. J. Detailed Balance Limit of Efficiency of P-n Junction Solar Cells. *J Appl Phys* **1961**, *32* (3), 510–519. https://doi.org/10.1063/1.1736034.

(126) Jaegermann, W.; Tributsch, H. Interfacial Properties of Semiconducting Transition Metal Chalcogenides. *Prog Surf Sci* **1988**, *29* (1–2), 1–167. https://doi.org/10.1016/0079-6816(88)90015-9.

(127) Ennaoui, A.; Fiechter, S.; Pettenkofer, C.; Bilker, K.; Bronold, M.; Ch, H.; Tributsch, H. Iron Disulfide for Solar Energy Conversion. **1993**, *29*, 289–370.

(128) Tao, D. ; Abdelkhalck, M. ; Chen, S. ; Parekh, B. K. ;; Hepworth, M. T. An Integrated Process for Utilization of Gypsum and Pyrite Wastes. In *International Conference on Environmental Issues and Management of Waste in Energy and Mineral Production*; 2000; pp 347–353.

(129) Puthussery, J.; Seefeld, S.; Berry, N.; Gibbs, M.; Law, M. Colloidal Iron Pyrite (FeS 2) Nanocrystal Inks for Thin Film Photovoltaics. *J Am Chem Soc* **2011**, *133* (4), 716–719.

(130) Tributsch, H.; Pohlmann, L. Electron Transfer: Classical Approaches and New Frontiers. *Science (1979)* **1998**, *279* (5358), 1891–1895. https://doi.org/10.1126/science.279.5358.1891.

(131) Ennaoui, A.; Tributsch, H. Energetic Characterization of the Photoactive FeS2 (Pyrite) Interface. *Solar Energy Materials* **1986**, *14*, 461–474.

(132) Ennaoui, A.; Tributsch, H. Iron Sulphide Solar Cells. *Solar Cells* **1984**, *13* (2), 197–200. https://doi.org/10.1016/0379-6787(84)90009-7.

(133) Büker, K.; Vante, N. A.; Tributsch, H.; Biiker, K.; Alonso-vante, P. I.; Tributsch, H. Photovoltaic Output Limitation of n - FeS2 (Pyrite) Schottky Barriers : A Temperature - Dependent Characterization. *J Appl Phys* **1992**, *72* (1992), 5721–5728. https://doi.org/10.1063/1.351925.

(134) Chongyang, L.; Pettenkofer, C.; Tributsch, H. Enhancement of Photoactivity in Pyrite (FeS2) Interfaces by Photoelectrochemical Processes. *Surf Sci* **1988**, *204* (3), 537–554. https://doi.org/10.1016/0039-6028(88)90233-6.

(135) Ennaoui, A.; Fiechter, S.; Goslowsky, H.; Tributsch, H. Photoactive Synthetic Polycrystalline Pyrite (FeS). 10–13.

(136) Ennaoui, A.; Fiechter, S.; Jaegermann, W.; Tributsch, H. Photoelectrochemistry of Highly Quantum Efficient Single- Crystalline n-FeS (Pyrite). *133* (1).

(137) Büker, K.; Alonso-Vante, N.; Tributsch, H. Photovoltaic Output Limitation of N-FeS2 (Pyrite) Schottky Barriers: A Temperature-Dependent Characterization. *J Appl Phys* **1992**, *72* (12), 5721–5728. https://doi.org/10.1063/1.351925.

(138) Ennaoui, A.; Flechter, S.; Smestad, G.; Tributsch, H. Preparation of Iron Disulfide and Its Use for Solar Energy Conversion. In *Energy and the Environment: Into the 1990s*; Sayigh, A. A. M., Ed.; Pergamon Press: Oxford, 1990; pp 458–464. https://doi.org/10.1016/B978-0-08-037539-7.50078-8.

(139) Altermatt, P. P.; Kiesewetter, T.; Ellmer, K.; Tributsch, H. Specifying Targets of Future Research in Photovoltaic Devices Containing Pyrite (FeS2) by Numerical Modelling. *Solar Energy Materials and Solar Cells* **2002**, *71* (2), 181–195. https://doi.org/10.1016/S0927-0248(01)00053-8.

(140) Hopfner, C.; Ellmer, K.; Ennaoui, A.; Pettenkofer, C.; Fiechter, S.; Tributsch, H. Stoichiometry, Phase, and Orientation Controlled Growth of Polycrystalline Pyrite (FeS2) Thin Films by MOCVD. *J Cryst Growth* **1995**, *151*, 325–334.

(141) Chatzitheodorou, G.; Fiechter, S.; Konenkamd, R.; Kunst, M.; Jaegermann, W.; Tributsch, H. Thin Photoactive FeS2 (Pyrite) Films. *Mater Res Bull* **1986**, *21*, 1481–1487.

(142) Fiechter, S.; Birkholz, M.; Hartmann, A.; Dulski, P.; Giersig, M.; Tributsch, H. The Microstructure and Stoichiometry of Pyrite. **1992**, *7* (7), 1829–1838.

(143) Alonso-Vante, N.; Chatzitheodorou, G.; Fiechter, S.; Mgoduka, N.; Poulios, I.; Tributsch, H. Interfacial Behavior of Hydrogen-Treated Sulphur Deficient Pyrite (FeS2-x). *Solar Energy Materials* **1988**, *18* (1–2), 9–21. https://doi.org/10.1016/0165-1633(88)90041-X.

(144) G. SMESTAD; ENNAOUI, A.; FIECHTER, S.; TRIBUTSCH, H.; HOFMANN, W. K.; BIRKHOLZ, M.; KAUTEK, W. PHOTOACTIVE THIN FILM SEMICONDUCTING IRON PYRITE PREPARED BY SULFURIZATION OF IRON OXIDES. *Solar Energy Materials* **1990**, *20*, 149–165.

(145) Smestad, G.; da Silva, A.; Tributsch, H.; Fiechter, S.; Kunst, M.; Meziani, N.; Birkholz, M. Formation of Semiconducting Iron Pyrite by Spray Pyrolysis. *Solar Energy Materials* **1989**, *18* (5), 299–313. https://doi.org/10.1016/0165-1633(89)90044-0.

(146) Metallic, O.; Vapor, C.; Layer, D.; Ennaoui, A.; Fiechter, S.; Tributsch, H.; Energetik, A. S.; Berlin, D. Photoelectrochemical Energy Conversion Obtained with Ultrathin Organo-Metallic-Chemical-Vapor-Deposition Layer of FeS2 (Pyrite) on TiO2. **1992**, *2*, 1–6.

(147) Birkholz, M.; Hartmann, A. Sulfur Deficiency in Iron Pyrite (FeS2-x)and Its Consequences for Band-Structure Models. *The American Physical Society* **1991**, *43* (14), 11926–11936.

(148) Ennaoui, A.; Fiechter, S.; Smestad, G.; Tributsch, H. Preparation of Iron Disulfide and Its Use for Solar Energy Conversion. In *Energy and the Environment into the 1990s*; 1990. https://doi.org/10.1016/B978-0-08-037539-7.50078-8.

(149) Steinhagen, C.; Harvey, T. B.; Stolle, C. J.; Harris, J.; Korgel, B. A. Pyrite Nanocrystal Solar Cells: Promising, or Fool ' s Gold? *Physical Chemistry Letters* **2012**, *3*, 2352–2356.

(150) Green, M. A.; Hishikawa, Y.; Dunlop, E. D.; Levi, D. H.; Hohl-Ebinger, J.; Yoshita, M.; Ho-Baillie, A. W. Y. Solar Cell Efficiency Tables (Version 53). *Progress in Photovoltaics: Research and Applications* **2019**, *27* (1), 3–12. https://doi.org/10.1002/pip.3102.

(151) Rahman, M. Z.; Rahman, T. What Is Limiting Pyrite Solar Cell Performance? Mohammad. *Joule* **2019**, *3*, 2282–2293.

(152) Voigt, B.; Moore, W.; Manno, M.; Walter, J.; Jeremiason, J. D.; Aydil, E. S.; Leighton, C. Transport Evidence for Sulfur Vacancies as the Origin of Unintentional n - Type Doping in Pyrite FeS 2. **2019**. https://doi.org/10.1021/acsami.9b01335.

(153) Seefeld, S.; Limpinsel, M.; Liu, Y.; Farhi, N.; Weber, A.; Zhang, Y.; Berry, N.; Kwon, Y. J.; Perkins, C. L.; Hemminger, J. C.; Wu, R.; Law, M. Iron Pyrite Thin Films Synthesized from an Fe(Acac)3Ink. *J Am Chem Soc* **2013**, *135* (11), 4412–4424. https://doi.org/10.1021/ja311974n.

(154) Prabukanthan, P.; Thamaraiselvi, S.; Harichandran, G. Single Step Electrochemical Deposition of P-Type Undoped and Co 2 + Doped FeS 2 Thin Films and Performance in Heterojunction Solid Solar Single Step Electrochemical Deposition of p-Type Undoped and Co 2 + Doped FeS 2 Thin Films and Performance in Heteroju. *J Electrochem Soc* **2017**, *164*, D581–D589. https://doi.org/10.1149/2.0991709jes.

(155) Zhang, X.; Li, M.; Walter, J.; Brien, L. O.; Manno, M. A.; Voigt, B.; Mork, F.; Baryshev, S. v; Kakalios, J.; Aydil, E. S.; Leighton, C. Potential Resolution to the Doping Puzzle in Iron Pyrite : Carrier Type Determination by Hall Effect and Thermopower. *Phys Rev Mater* **2017**, *015402*, 1–11. https://doi.org/10.1103/PhysRevMaterials.1.015402.

(156) Sánchez, C.; Flores, E.; Barawi, M.; Clamagirand, J. M.; Ares, J. R.; Ferrer, I. J. Marcasite Revisited : Optical Absorption Gap at Room Temperature. *Solid State Commun* **2016**, *230*, 20–24. https://doi.org/10.1016/j.ssc.2016.01.004.

(157) Moon, D. G.; Rehan, S.; Lim, S. Y.; Nam, D.; Seo, I.; Gwak, J. Structural , Optical and Electrical Impacts of Marcasite in Pyrite Thin Fi Lms. *Solar Energy* **2018**, *159* (November 2017), 930–939. https://doi.org/10.1016/j.solener.2017.11.026.

(158) Wu, L.; Dzade, N. Y.; Gao, L.; Scanlon, D. O.; Öztürk, Z.; Hollingsworth, N.; Weckhuysen, B. M.; Hensen, E. J. M.; Leeuw, N. H. de; Hofmann, J. P. Enhanced Photoresponse of FeS 2 Films : The Role of Marcasite – Pyrite Phase Junctions. **2016**, 9602–9607. https://doi.org/10.1002/adma.201602222.

(159) Sun, R.; Chan, M. K. Y.; Ceder, G. First-Principles Electronic Structure and Relative Stability of Pyrite and Marcasite : Implications for Photovoltaic Performance. **2011**, *235311*, 1–12. https://doi.org/10.1103/PhysRevB.83.235311.

(160) Zhang, X.; Scott, T.; Socha, T.; Nielsen, D.; Manno, M.; Johnson, M.; Yan, Y.; Losovyj, Y.; Dowben, P.; Aydil, E. S.; Leighton, C. Phase Stability and Stoichiometry in Thin Film Iron Pyrite: Impact on Electronic

Transport Properties. *ACS Appl Mater Interfaces* **2015**, *7* (25), 14130–14139. https://doi.org/10.1021/acsami.5b03422.

(161) Luck, J.; Hartmann, A.; Fiechter, S. Stoichiometry and Impurity Concentration in Synthetically Grown Iron Pyrite Crystals and Their Constituents. *Fresenius' Zeitschrift für Analytische Chemie* **1989**, *334* (5), 441–446. https://doi.org/10.1007/BF00469468.

(162) Bhandari, K. P.; Roland, P. J.; Kinner, T.; Cao, Y.; Choi, H.; Jeong, S.; Ellingson, R. J. Analysis and Characterization of Iron Pyrite Nanocrystals and Nanocrystalline Thin Films Derived from Bromide Anion Synthesis. *J Mater Chem A Mater* **2015**, *3* (13), 6853–6861. https://doi.org/10.1039/c4ta06320a.

(163) Voigt, B.; Moore, W.; Maiti, M.; Walter, J.; Das, B.; Manno, M.; Leighton, C.; Aydil, E. S. Observation of an Internal p − n Junction in Pyrite FeS 2 Single Crystals: Potential Origin of the Low Open Circuit Voltage in Pyrite Solar Cells. *American Chemical Society Materials Letters* **2020**, *2*, 861–868. https://doi.org/10.1021/acsmaterialslett.0c00207.

(164) Yu, L.; Lany, S.; Kykyneshi, R.; Jieratum, V.; Ravichandran, R.; Pelatt, B.; Altschul, E.; Platt, H. A. S.; Wager, J. F.; Keszler, D. A.; Zunger, A. Iron Chalcogenide Photovoltaic Absorbers. *Adv Energy Mater* **2011**, *1*, 748–753. https://doi.org/10.1002/aenm.201100351.

(165) Hu, J.; Zhang, Y.; Law, M.; Wu, R. First-Principles Studies of the Electronic Properties of Native and Substitutional Anionic Defects in Bulk Iron Pyrite Density of States. **2012**, *085203*, 1–10. https://doi.org/10.1103/PhysRevB.85.085203.

(166) Herbert, F. W.; Krishnamoorthy, A.; van Vliet, K. J.; Yildiz, B. Quantification of Electronic Band Gap and Surface States on FeS2(100). *Surf Sci* **2013**, *618*, 53–61. https://doi.org/10.1016/j.susc.2013.08.014.

(167) Ganduglia-Pirovano, M. V.; Hofmann, A.; Sauer, J. Oxygen Vacancies in Transition Metal and Rare Earth Oxides : Current State of Understanding and Remaining Challenges. *Surf Sci Rep* **2007**, *62*, 219–270. https://doi.org/10.1016/j.surfrep.2007.03.002.

(168) Mcauliffe, R. D.; Shoemaker, D. P. Inflexible Stoichiometry in Bulk Pyrite FeS 2 as Viewed by in Situ and High-Resolution X-Ray Diffraction. *Acta Crystallogr B Struct Sci Cryst Eng Mater* **2018**, *74*, 436–444. https://doi.org/10.1107/S2052520618010144.

(169) Shukla, S.; Xing, G.; Ge, H.; Prabhakar, R. R.; Mathew, S.; Su, Z.; Nalla, V.; Venkatesan, T.; Mathews, N.; Sritharan, T.; Sum, T. C.; Xiong, Q. Origin of Photocarrier Losses in Iron Pyrite (FeS2) Nanocubes. *ACS Nano* **2016**, *10* (4), 4431–4440. https://doi.org/10.1021/acsnano.6b00065.

(170) Berry, N.; Cheng, M.; Perkins, C. L.; Limpinsel, M.; Hemminger, J. C.; Law, M. Atmospheric-Pressure Chemical Vapor Deposition of Iron Pyrite Thin Films. **2012**, *201200043*, 1124–1135. https://doi.org/10.1002/aenm.201200043.

(171) Morrish, R.; Silverstein, R.; Wolden, C. A. Synthesis of Stoichiometric FeS 2 through Plasma-Assisted Sulfurization of Fe2O3 Nanorods. *J Am Chem Soc* **2012**, *134*, 17854–17857.

(172) Fukui, T.; Miyadai, T. Photoconductivity of Natural Pyrite (FeS2). *J Physical Soc Japan* **1971**, *31*, 1277.

(173) Walter, J.; Zhang, X.; Voigt, B.; Hool, R.; Manno, M.; Mork, F.; Aydil, E. S.; Leighton, C. Surface Conduction in n -Type Pyrite FeS2 Single Crystals. *Phys Rev Mater* **2017**, *1* (6), 1–17. https://doi.org/10.1103/PhysRevMaterials.1.065403.

(174) Bi, Y.; Yuan, Y.; Exstrom, C. L.; Darveau, S. A.; Huang, J. Air Stable, Photosensitive, Phase Pure Iron Pyrite Nanocrystal Thin Films for Photovoltaic Application. *Nano Lett* **2011**, *11* (11), 4953–4957. https://doi.org/10.1021/nl202902z.

(175) Wang, F.; Tang, R.; Buhro, W. E. The Trouble with TOPO; Identification of Adventitious Impurities Beneficial to the Growth of Cadmium Selenide Quantum Dots, Rods, and Wires. *Nano Lett* **2008**, *8* (10), 3521–3524. https://doi.org/10.1021/nl801692g.

(176) Li, W.; Dittrich, T.; Jäckel, F.; Feldmann, J. Optical and Electronic Properties of Pyrite Nanocrystal Thin Films: The Role of Ligands. *Small* **2014**, *10* (6), 1194–1201. https://doi.org/10.1002/smll.201302333.

(177) Murphy, R.; Strongin, D. R. Surface Science Reports Surface Reactivity of Pyrite and Related Sulfides. *Surf Sci Rep* **2009**, *64* (1), 1–45. https://doi.org/10.1016/j.surfrep.2008.09.002.

(178) Zhang, Y. N.; Hu, J.; Law, M.; Wu, R. Q. Effect of Surface Stoichiometry on the Band Gap of the Pyrite FeS2(100) Surface. *Phys Rev B Condens Matter Mater Phys* **2012**, *85* (8), 1–5. https://doi.org/10.1103/PhysRevB.85.085314.

(179) MacPherson, H. A.; Stoldt, C. R. Iron Pyrite Nanocubes: Size and Shape Considerations for Photovoltaic Application. *ACS Nano* **2012**, *6* (10), 8940–8949. https://doi.org/10.1021/nn3029502.

(180) Uchiyama, S.; Ishikawa, Y.; Uraoka, Y. Effect of Inversion Layer at Iron Pyrite Surface on Photovoltaic Device. **2018**, 2–9.

(181) Zhang, Y. N.; Hu, J.; Law, M.; Wu, R. Q. Effect of Surface Stoichiometry on the Band Gap of the Pyrite FeS 2 (100) Surface. **2012**, *085314*, 1–5. https://doi.org/10.1103/PhysRevB.85.085314.

(182) Wilkin, R. T.; Barnes, H. L. Pyrite Formation by Reactions of Iron Monosulfides with Dissolved Inorganic and Organic Sulfur Species. *Geochim Cosmochim Acta* **1996**, *60* (21), 4167–4179. https://doi.org/10.1016/S0016-7037(97)81466-4.

(183) Benning, L. G.; Wilkin, R. T.; Barnes, H. L. Reaction Pathways in the Fe – S System below 100 8 C. **2000**.

(184) Moehring, N. K.; Fort, M. J.; Mcbride, J. R.; Kato, M.; Macdonald, J. E.; Kidambi, P. R. In Situ Observations of Thermally Induced Phase Transformations in Iron Sulfide Nanoparticles. *Mater Today Adv* **2020**, *6*, 100057. https://doi.org/10.1016/j.mtadv.2020.100057.

(185) Jagadeesh, M. S.; Seehra, M. S. Electrical Resistivity and Band Gap of Marcasite (FeS2). *Physics Letters* **1980**, *80* (I), 77–79.

(186) Schena, T.; Bihlmayer, G.; Bl, S.; Gr, P. First-Principles Studies of FeS 2 Using Many-Body Perturbation Theory in the G 0 W 0 Approximation. **2013**, *235203*, 1–10. https://doi.org/10.1103/PhysRevB.88.235203.

(187) Cabán-Acevedo, M.; Kaiser, N. S.; English, C. R.; Liang, D.; Thompson, B. J.; Chen, H. E.; Czech, K. J.; Wright, J. C.; Hamers, R. J.; Jin, S. Ionization of High-Density Deep Donor Defect States Explains the Low

Photovoltage of Iron Pyrite Single Crystals. *J Am Chem Soc* **2014**, *136* (49), 17163–17179. https://doi.org/10.1021/ja509142w.

(188) Rickard, D.; Luther, G. W. Chemistry of Iron Sulfides. *Chemical R* **2007**, *107* (0), 514–562.

(189) Vaughan, A. D. J.; Lennie, A. R.; Vaughan, D. J.; Lennie, A. R. The Iron Sulphide Minerals : Their Chemistry and Role in Nature. *Science Progess* **1991**, *75* (3), 371–388.

(190) Hunger, S.; Benning, L. G. Greigite : A True Intermediate on the Polysulfide Pathway to Pyrite. **2007**, *20*, 1–20. https://doi.org/10.1186/1467-4866-8-1.

(191) Matamoros-veloza, A.; Stawski, T. M.; Benning, L. G. Nanoparticle Assembly Leads to Mackinawite Formation. *Cryst Growth Des* **2018**, *18*, 6757–6764. https://doi.org/10.1021/acs.cgd.8b01025.

(192) Clayton, A. J.; Irvine, S. J. C.; Barrioz, V.; Brooks, W. S. M.; Zoppi, G.; Forbes, I.; Rogers, K. D.; Lane, D. W.; Hutchings, K.; Roncallo, S. Metal-Organic Chemical Vapor Deposition of Ultra-Thin Photovoltaic Devices Using a Pyrite Based p – i – n Structure. *Thin Solid Films* **2011**, *519* (21), 7360–7363. https://doi.org/10.1016/j.tsf.2010.12.147.

(193) Smestad, G.; Silva, A. D. A.; Birkholz, M. Formation of Semiconducting Iron Pyrite by Spray Pyrolysis. *Solar Energy Materials* **1989**, *18*, 299–313.

(194) Puthussery, J.; Seefeld, S.; Berry, N.; Gibbs, M.; Law, M. Colloidal Iron Pyrite (FeS2) Nanocrystal Inks for Thin-Film Photovoltaics. *J Am Chem Soc* **2011**, *133* (4), 716–719. https://doi.org/10.1021/ja1096368.

(195) Rhodes, J. M.; Jones, C. A.; Thal, L. B.; MacDonald, J. E. Phase-Controlled Colloidal Syntheses of Iron Sulfide Nanocrystals via Sulfur Precursor Reactivity and Direct Pyrite Precipitation. *Chemistry of Materials* **2017**, *29* (19), 8521–8530. https://doi.org/10.1021/acs.chemmater.7b03550.

(196) Lutz, H. D.; Zwinscher, J. Lattice Dynamics of Pyrite FeS2- Polarizable-Ion Model. *Phys Chem Miner* **1996**, *23* (8), 497–502. https://doi.org/10.1007/BF00241999.

(197) Mori, T.; Orikasa, Y.; Nakanishi, K.; Kezheng, C.; Hattori, M.; Ohta, T.; Uchimoto, Y. Discharge/Charge Reaction Mechanisms of FeS2 Cathode Material for Aluminum Rechargeable Batteries at 55°C. *J Power Sources* **2016**, *313*, 9–14. https://doi.org/10.1016/j.jpowsour.2016.02.062.

(198) Yersak, T. A.; Macpherson, H. A.; Kim, S. C.; Le, V. D.; Kang, C. S.; Son, S. B.; Kim, Y. H.; Trevey, J. E.; Oh, K. H.; Stol dt, C.; Lee, S. H. Solid State Enabled Reversible Four Electron Storage. *Adv Energy Mater* **2013**, *3* (1), 120–127. https://doi.org/10.1002/aenm.201200267.

(199) Fong, R.; Dahn, J. R.; Jones, C. H. W. Electrochemistry of Pyrite-Based Cathodes for Ambient Temperature Lithium Batteries. *J Electrochem Soc* **1989**, *136* (11), 3206–3210.

(200) Strauss, E.; Golodnitsky, D.; Peled, E. *Study of Phase Changes during 500 Full Cycles of Li/Composite Polymer Electrolyte/FeS 2 Battery*; 2000; Vol. 45. www.elsevier.nl/locate/electacta.

(201) Dewald, G. F.; Liaqat, Z.; Lange, M. A.; Tremel, W.; Zeier, W. G. Solid-State Batteries Influence of Iron Sulfide Nanoparticle Sizes in Solid-State Batteries**. *Angewandte Chemie* **2021**, *60*, 17952–17956. https://doi.org/10.26434/chemrxiv.14483370.

(202) Douglas, A.; Carter, R.; Oakes, L.; Share, K.; Cohn, A. P.; Pint, C. L. Ultrafine Iron Pyrite (FeS2) Nanocrystals Improve Sodium-Sulfur and Lithium-Sulfur Conversion Reactions for Efficient Batteries. *ACS Nano* **2015**, *9* (11), 11156–11165. https://doi.org/10.1021/acsnano.5b04700.

(203) Kaur, G.; Kaur, M.; Thakur, A.; Kumar, A. *Recent Progress on Pyrite FeS2 Nanomaterials for Energy and Environment Applications: Synthesis, Properties and Future Prospects*; Springer US, 2020; Vol. 31. https://doi.org/10.1007/s10876-019-01708-3.

(204) Wang, Y. C.; Wang, D. Y.; Jiang, Y. T.; Chen, H. A.; Chen, C. C.; Ho, K. C.; Chou, H. L.; Chen, C. W. FeS2 Nanocrystal Ink as a Catalytic Electrode for Dye-Sensitized Solar Cells. *Angewandte Chemie - International Edition* **2013**, *52* (26), 6694–6698. https://doi.org/10.1002/anie.201300401.

(205) Huang, Q. H.; Ling, T.; Qiao, S. Z.; Du, X. W. Pyrite Nanorod Arrays as an Efficient Counter Electrode for Dye-Sensitized Solar Cells. *J Mater Chem A Mater* **2013**, *1* (38), 11828–11833. https://doi.org/10.1039/c3ta12347b.

(206) Zhou, M.; He, J.; Wang, L.; Zhao, S.; Wang, Q.; Cui, S.; Qin, X.; Wang, R. Synthesis of Carbonized-Cellulose Nanowhisker/FeS2@reduced Graphene Oxide Composite for Highly Efficient Counter Electrodes in Dye-Sensitized Solar Cells. *Solar Energy* **2018**, *166* (January), 71–79. https://doi.org/10.1016/j.solener.2018.01.089.

(207) Shukla, S.; Loc, N. H.; Boix, P. P.; Koh, T. M.; Prabhakar, R. R. Iron Pyrite Thin Film Counter Electrodes for Dye-Sensitized Solar Cells : High Efficiency for Iodine and Cobalt Redox Electrolyte Cells. *ACS Nano* **2014**, *8* (10), 10597–10605.

(208) Moore, C. G.; Watson, A. A. The Reaction of Alkenethiolate Ions with Dialkenyl Disulphides to Give Dialkenyl Monosulphides. *Tetrahedron* **1962**, *18* (2), 219–225. https://doi.org/10.1016/S0040-4020(01)92654-7.

(209) Turo, M. J.; Macdonald, J. E. Crystal-Bound vs Surface-Bound Thiols on Nanocrystals. *ACS Nano* **2014**, *8* (10), 10205–10213. https://doi.org/10.1021/nn5032164.

(210) Guo, Y.; Alvarado, S. R.; Barclay, J. D.; Vela, J. Shape-Programmed Nanofabrication: Understanding the Reactivity of Dichalcogenide Precursors. *ACS Nano* **2013**, *7* (4), 3616–3626. https://doi.org/10.1021/nn400596e.

(211) Hens, Z. A Solution NMR Toolbox for Characterizing the Surface Chemistry of Colloidal Nanocrystals. *Chemistry of Materials* **2013**, *25*, 1211–1221. https://doi.org/10.1021/cm303361s.

(212) Zou, J.; Zhao, J.; Wang, B.; Chen, S.; Chen, P.; Ran, Q.; Li, L.; Wang, X.; Yao, J.; Li, H.; Huang, J.; Niu, X.; Wang, L. Unraveling the Reaction Mechanism of FeS2as a Li-Ion Battery Cathode. *ACS Appl Mater Interfaces* **2020**, *12* (40), 44850–44857. https://doi.org/10.1021/acsami.0c14082.

(213) Tomczuk, Z.; Roche, M. F.; Vissers, D. R. Phase Relationships in Positive Electrodes of High Temperature Lithium Aluminum/Iron Sulfide Cells. *Proc Electrochem Soc* **1981**, *81–4*, 381–391.

(214) Gahan, L. R.; Healy, P. C.; Patch, G. J. Synthesis of Cobalt(III) “Cage” Complexes: A Twist on an Old Theme in the Inorganic Laboratory. *J Chem Educ* **1989**, *66* (5), 445–446. https://doi.org/10.1021/ed066p445.

(215) Gahan, L. R.; Harrowfield, J. M. Sepulchrate: Four Decades On. *Polyhedron* **2015**, *94* (20), 1–51. https://doi.org/10.1016/j.poly.2015.03.036.

(216) Creaser, I.; Harrowfield, J. M. B.; Herlt, A. J.; Sargeson, A. M.; Springborg, J.; Geue, R. J.; Snow, M. R. Sepulchrate: A Macrobicyclic Nitrogen Cage for Metal Ions. *J Am Chem Soc* **1977**, *99* (9), 3181–3182. https://doi.org/10.1021/ja00451a062.

(217) Sillen, A.; Engelborghs, Y. The Correct Use of "Average" Fluorescence Parameters. *Photochem Photobiol* **1998**, *67* (5), 475–486. https://doi.org/10.1111/j.1751-1097.1998.tb09082.x.

Appendices

A. Supporting Information for chapter 3

A1. Synthesis of (sepulchrate)cobalt(III) diethyl dithiocarbamate

$[Co(sep)][S_2CNEt_2]_3$ was synthesized in the manner described by Gahan with only minimal adjustments required.[214] Two separate solutions were made, one with 37% aqueous formaldehyde (25 mL) and the other with aqueous ammonia diluted (7 mL of 28% NH_4OH, diluted to 25 mL). The solutions were loaded into two 30 mL syringes. Using a syringe injector with an injection rate of 1mL/minute, the solutions co-injected into a flask containing 10 mL of water, Li_2CO_3 (1.15 g, 15.6 mmol) and $[Co(en)_3]Cl_3$ (0.45 g, 1.3 mmol). It was necessary to stir this flask at 700 rpm for 15 min prior to injection and for a minimum of 30 min after injection. The solution was then vacuum filtered to remove unreacted Li_2CO_3. A flask containing $Na[S_2CNEt_2]\cdot 3H_2O$ (1.25 g) and 25 mL of water was stirred for 10 min. at which point cobalt-containing filtrate was added. The mixture was stirred for 1 h at which point the precipitate was vacuum filtered and washed with portions of a 20:80 mixture of dichloromethane and hexanes to remove the green cobalt dithiocarbamate ($Co(S_2CNEt_2)_3$) impurity. The remaining red solid, $[Co(sep)][S_2CNEt_2]_3$, was dried on its filter paper overnight. Yield 0.337 g, 56%. ^{13}C NMR (400MHz, $CDCl_3$): δ 12.18, 48.14, 54.32, 68.42, 206.60. This is in agreement with the published literature [214].

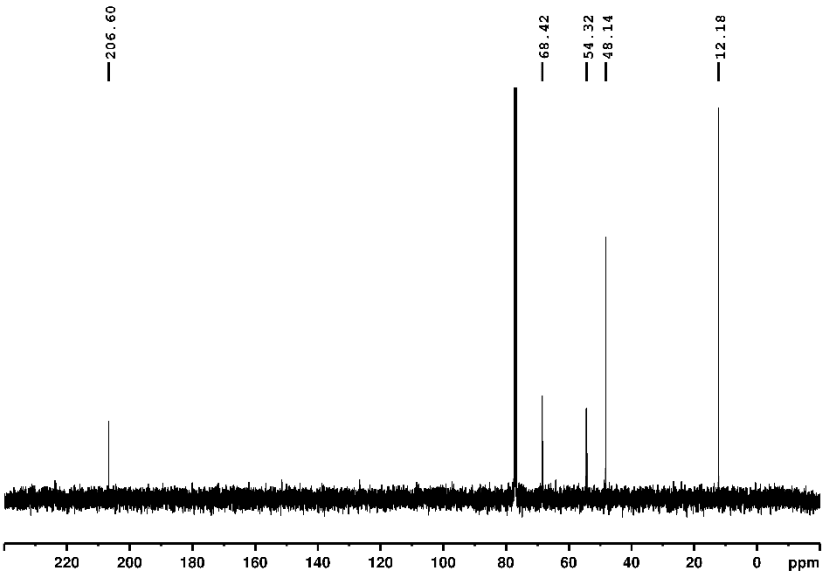

Figure A.1: ^{13}C NMR of $[Co(sep)][S_2CNEt_2]_3$ intermediate. Unlabeled peak is chloroform solvent.

A2. Synthesis of (sepulchrate)cobalt(III) chloride hydrate

$[Co(sep)]Cl_3 \cdot H_2O$ was synthesized in the manner described by Gahan with only minimal adjustments required.[214] $[Co(sep)][S_2CNEt_2]_3$ (100 mg) was dissolved in 10 mL of acetonitrile in a 6 dram vial. Concentrated hydrochloric acid (150 uL) was added. The vial placed on a hot plate at 90°C for 10 min while stirring at 700 rpm. The decomposed yellow solution was not observed to crystallize after cooling. A yellow solid was collected after precipitation with successive centrifugations in acetonitrile at 4000 rpm at room temperature. 150 uL water proved sufficient to make a deep red solution which was left to crystallize for 7 days. Yield 91.6 mg, 98 %. ^{1}H-NMR (400MHz, D_2O): δ 3.07 (AA'BB', 12H), 4.0 (AB d, 12.6H), 4.79 (D_2O residual). ^{13}C NMR (400MHz, D_2O): δ 66.88, 53.22. NMR is in agreement with Reference [214–216].

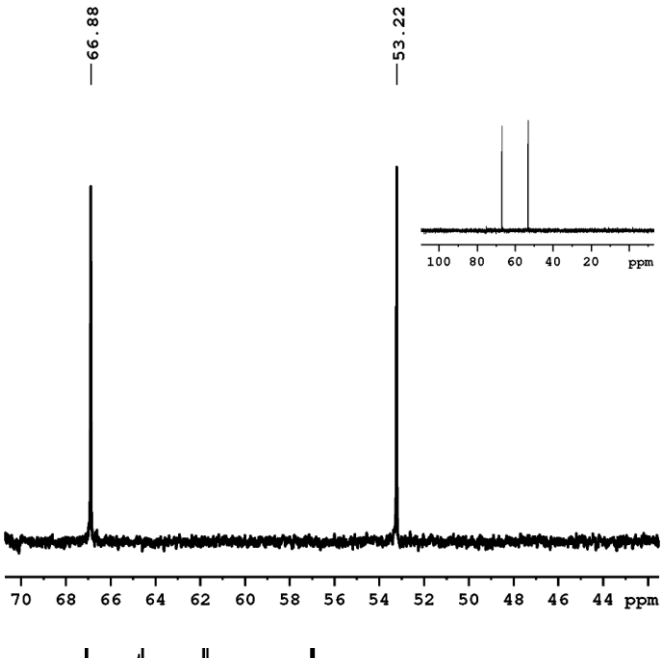

Figure A.2: ^{13}C NMR spectra of $[Co(sep)]Cl_3 \cdot H_2O$ in D_2O

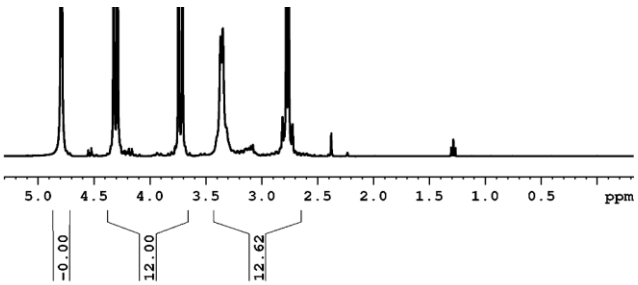

Figure A.31H NMR spectra of [Co(sep)]Cl3·H2O in D2O.

A3. Cyclic Voltammetry

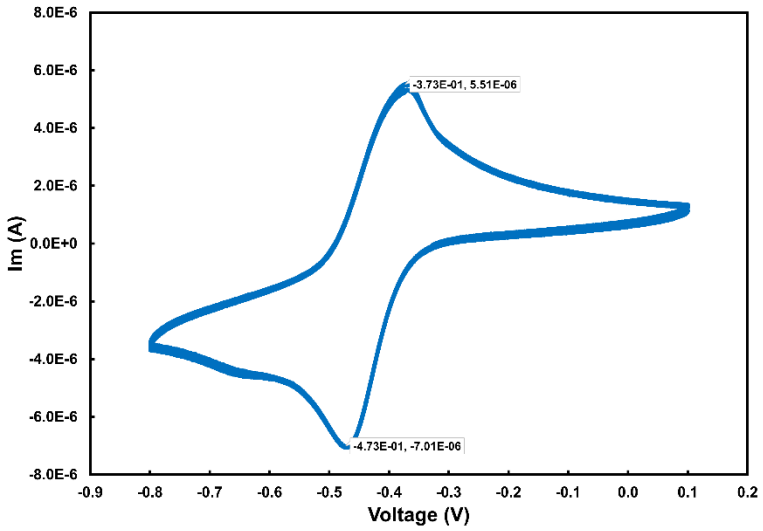

Figure A.4: CV of $[Co(en)_3]^{3/2+}$. $E_{1/2}$ = -0.423 V vs. Ag/AgCl, vs. NHE = -0.224 V

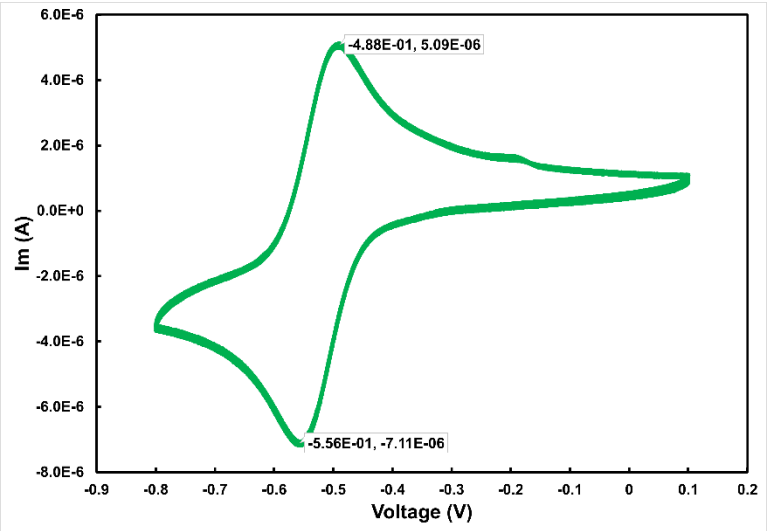

Figure A.5: CV of $[Co(sep)]^{3/2+}$ $E_{1/2}$=-0.522 V vs. AgCl/Ag, vs. NHE= -0.323V

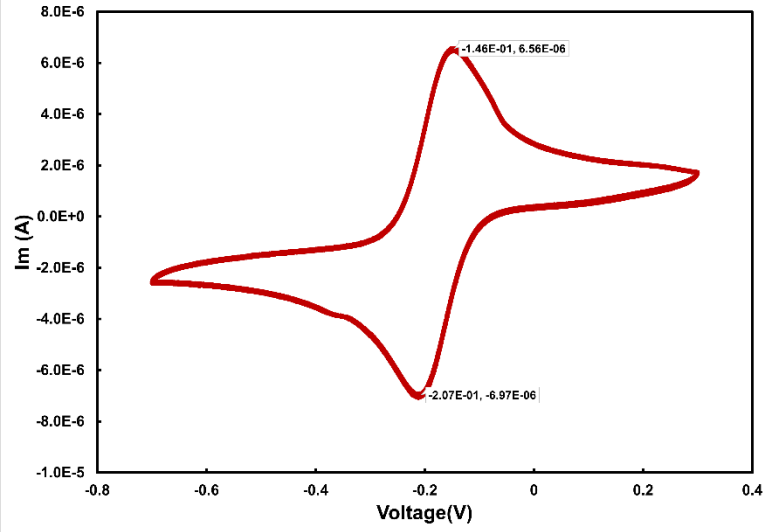

Figure A.6: CV of $[Co(ClMeN_3S_3sar)]^{3/2+}$ $E_{1/2}$= -0.177 V vs. Ag/AgCl, vs. NHE = 0.022 V

A4. Steady State Absorbance Spectra

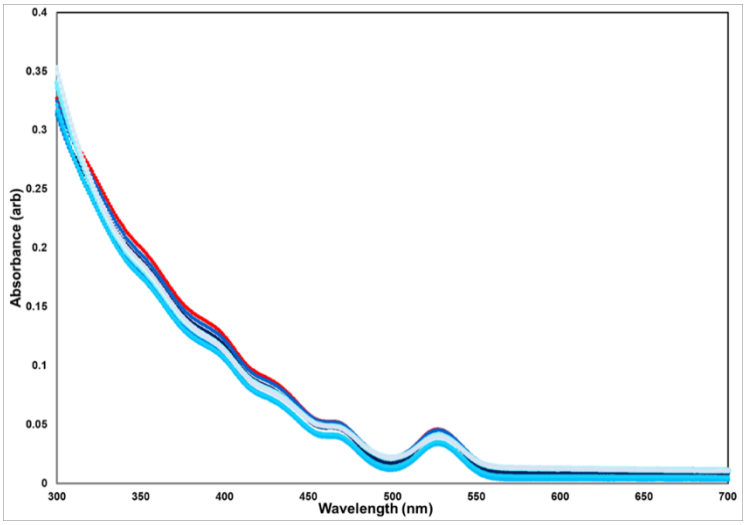

Figure A.7: Absorption spectra of solutions of green emitting Zn/CdSe/S alloy QDs with additions of $[Co(en)_3]^{3/2+}$ (matching steady state fluorescence experiments in main text)

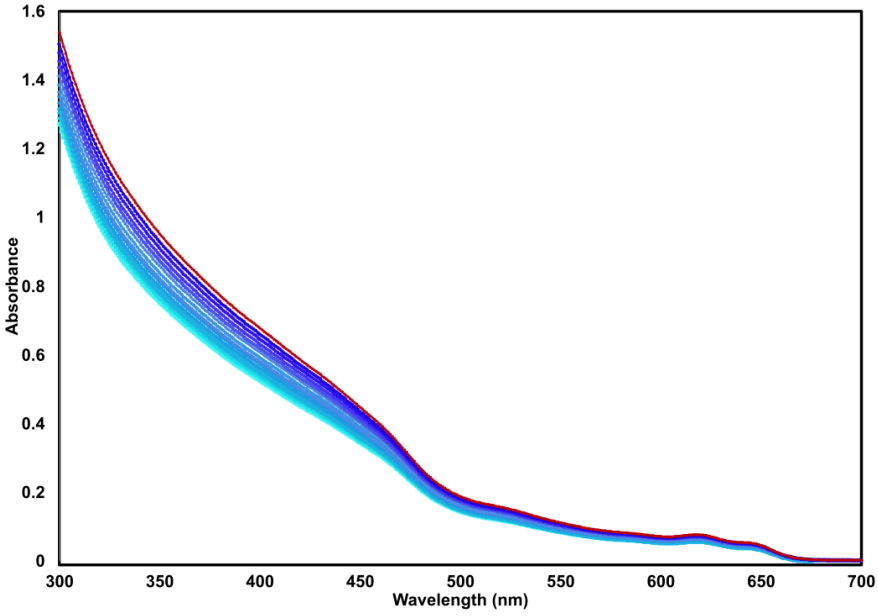

Figure A.9: Absorption spectra of solutions of red emitting CdSe@CdS QDs with additions of $[Co(en)_3]^{3/2+}$ (matching steady state fluorescence experiments in main text)

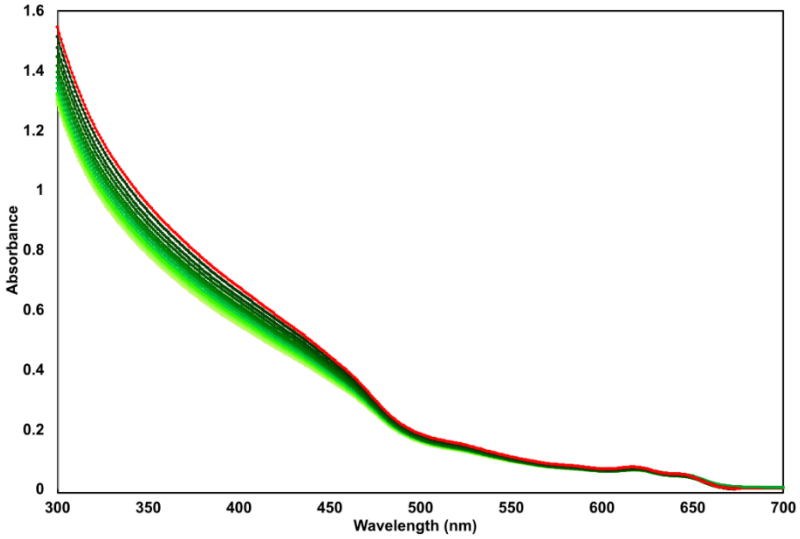

Figure A.11: Absorption spectra of solutions of red emitting CdSe@CdS QDs with additions of $[Co(sep)]^{3/2+}$ (matching steady state fluorescence experiments in main text)

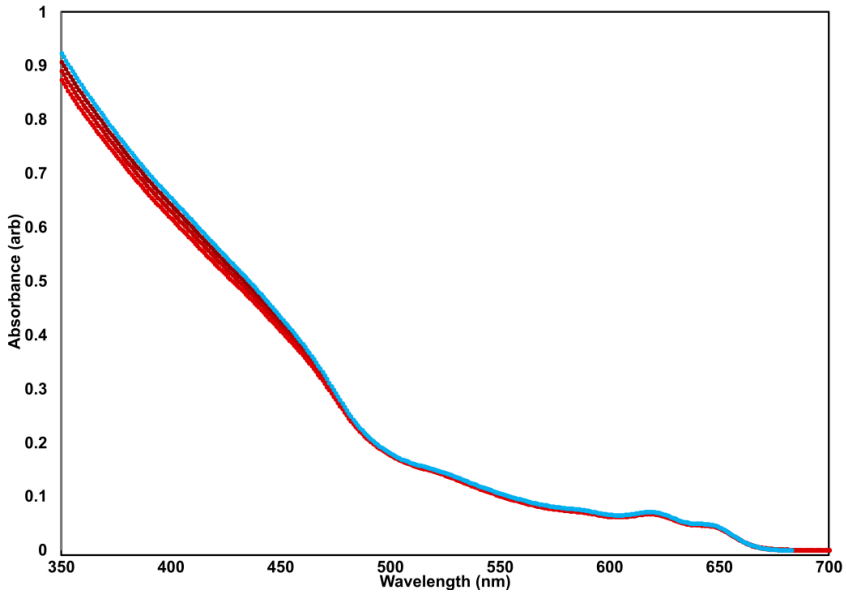

Figure A.12: Absorption spectra of solutions of red emitting CdSe@CdS QDs with additions of $[Co(ClMeN_3S_3sar)]^{3/2+}$ (matching steady state fluorescence experiments in main text)

A5. Time-resolved Photoluminescence Fits

	[Co(III)]μM	Amp_1	Amp_2	Amp_3	τ_1	τ_2	τ_3	τ_{avg}#	C^2
$[Co(en)_3]^{3/2+}$g	0	8491.0	1072.9	357.9	20.1	3.8	60.1	19.8	1.0187
	17.3	3136.7	3607.9	293.4	3.4	14.1	34.3	10.4	1.1267
	29.0	2763.1	1996.6	854.7	4.4	1.4	11.1	4.4	1.2895
	37.5	1882.3	1553.8	691.6	4.2	1.5	9.9	4.1	1.1248
	44.8	1950.4	1239.3	664.3	3.7	1.2	9.5	3.9	1.1313
[Co(sep)]$^{3/2+}$g	0	8491.0	1072.9	357.9	20.1	3.81	60.1	19.8	1.0187
	17.3	4502.2	2822.7	827.6	0.9	3.8	11.6	3.0	1.2096
	29.2	2408.4	1416.2	426.5	0.7	2.3	7.0	1.9	1.0840
	38.8	2517.3	5614.0	488.8	1.9	0.5	6.3	1.3	1.1163
	*44.6	226.6	21.6	94.9	0.6	0.0	3.0	1.1	1.0333
$[Co(ClMeN_3S_3sar)]^{3/2+}$g	0	6849.0	1450.0	1633.0	18.6	3.4	32.5	18.7	1.0005
	4.9	4129.0	1868.0	1378.0	0.7	4.9	17.4	4.9	1.2360
	10.0	33039.0	1031.0	327.0	0.4	2.0	7.8	1.3	0.9584

	[Co(III)]μM	Amp_1	Amp_2	Amp_3	τ_1	τ_2	τ_3	τ_{avg}	C^2
$[Co(en)_3]^{3/2+}$r	0	240.1	3071.4	1227.1	3.8	27.6	66.4	36.8	1.0207
	18.1	289.2	2444.0	1076.9	3.5	26.8	62.6	35.2	0.9878
	30.0	322.9	1888.3	946.2	5.0	25.7	58.8	33.5	1.0756
	37.6	346.5	1722.4	661.4	4.2	25.6	60.7	31.4	1.0442
	44.7	347.9	1337.0	412.3	4.5	25.0	58.5	28.2	1.0111
[Co(sep)]$^{3/2+}$r	0	199.9	2919.7	1213.5	2.9	27.2	65.4	36.8	1.1011
	17.3	154.1	1779.5	815.8	3.6	26.6	58.4	34.8	1.0641
	28.7	296.8	1778.7	488.2	5.0	26.9	62.2	31.1	0.9373
	37.4	326.5	1405.5	560.3	4.4	23.8	52.3	28.0	1.0551
	44.6	259.0	918.5	283.7	3.9	22.6	49.6	24.5	1.0824
$[Co(ClMeN_3S_3sar)]^{3/2+}$r	0	297.0	4369.0	1814.0	3.7	27.3	63.1	36.3	1.0950
	46.1	2057.0	1943.3	1141.0	3.3	18.3	46.6	18.6	1.0057
	89.3	1369.0	962.0	165.0	0.9	2.5	7.5	1.9	0.9187

* fluorescence intensity was very low; fits are unreliable.

#Average lifetime calculated [217] by

$$\tau_{avg} = \frac{\sum_i^3 Amp_i \tau_i}{\sum_i^3 Amp_i}$$

A6. Discussion of Forster Resonant Energy Transfer (FRET)

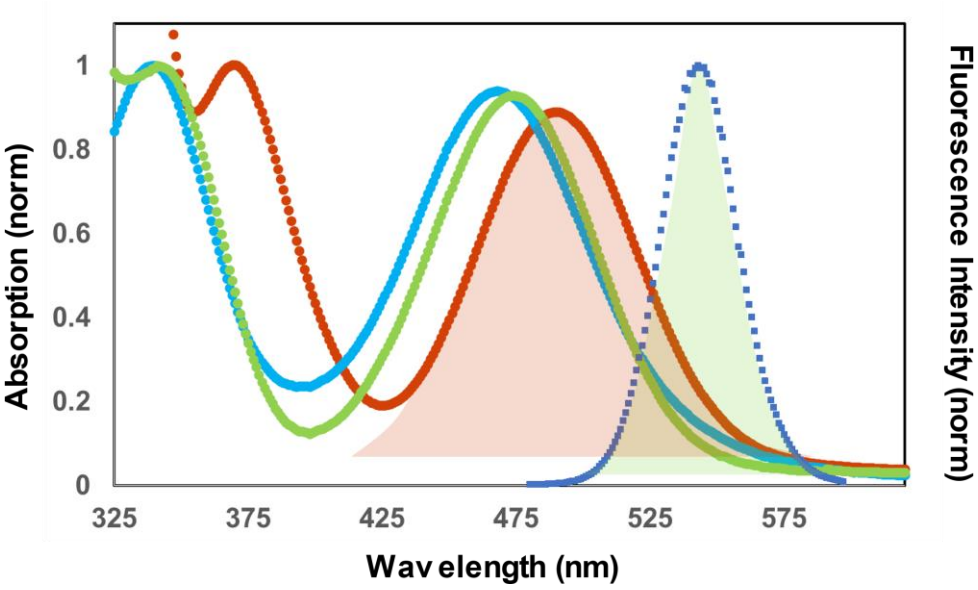

Figure A.13: General concept of spectral overlap required for FRET. Absorbance spectra of $[Co(en)_3]Cl_{3(aq)}$ (blue), $[Co(sep)]Cl_{3(aq)}$ (green) and $[Co(ClMeN_3S_3sar)]Cl_{3(aq)}$ (red) and the emission of the green emitting quantum dots (blue dotted). (Spectra are not normalized for FRET).

FRET and other resonant transfer mechanisms are dependent upon the degree of spectral overlap between the donor and the acceptor. The degree of spectral overlap is calculated by:

$$J = \int f(\lambda)\epsilon_a \lambda^4 \, d\lambda$$

This function uses the fluorescence of the donor *f(l)* normalized to where the area equals unity. The extinction coefficient of the acceptor ϵ_a are obtained through the absorbance spectrum of the sample, normalized for concentration. The following values were obtained from this expression for the overlap between the green emitting QDs and the cobalt complexes. They are low for FRET, but not outside of reason.

Table A.1: Optical values for cobalt complexes.

	ε_{max} ($M^{-1}cm^{-1}$)	ε (400 nm, $M^{-1}cm^{-1}$)	J ($M^{-1}cm^{-1}$ nm^{4-})	Ro(nm)
$[Co(en)_3]Cl_3$	85.58 (468 nm)	25.46	$1.316x10^{12}$	1.7
$[Co(sep)]Cl_3$	127.3 (474 nm)	14.10	$1.298x10^{12}$	1.7
$[Co(ClMeN_3S_3sar)]Cl_3$	905.8 (498 nm)	391.3	$18.63x10^{12}$	2.6

The distance at which the FRET process has a 50% possibility, R_o can be calculated by

$$R_o = 0.02108(k^2 \phi n^{-4} J)^{\frac{1}{6}} \text{ (nm)}$$

k is the orientation factor between the two dipole moments and is usually 2/3, ϕ is the quantum yield of the donor species, and *n* is dielectric constant of the solvent. This yielded values for these systems of 1.4 nm to 1.7 nm depending on if quantum yield was assumed to be 0.5 to 0.9. QDs as purchased had a lot requirement over 85%. The calculated values are given in Table A.1.

A6. Scanning Transmission Electorn Microscopy Energy Dispersive Spectrocopy (EDS) Mapping

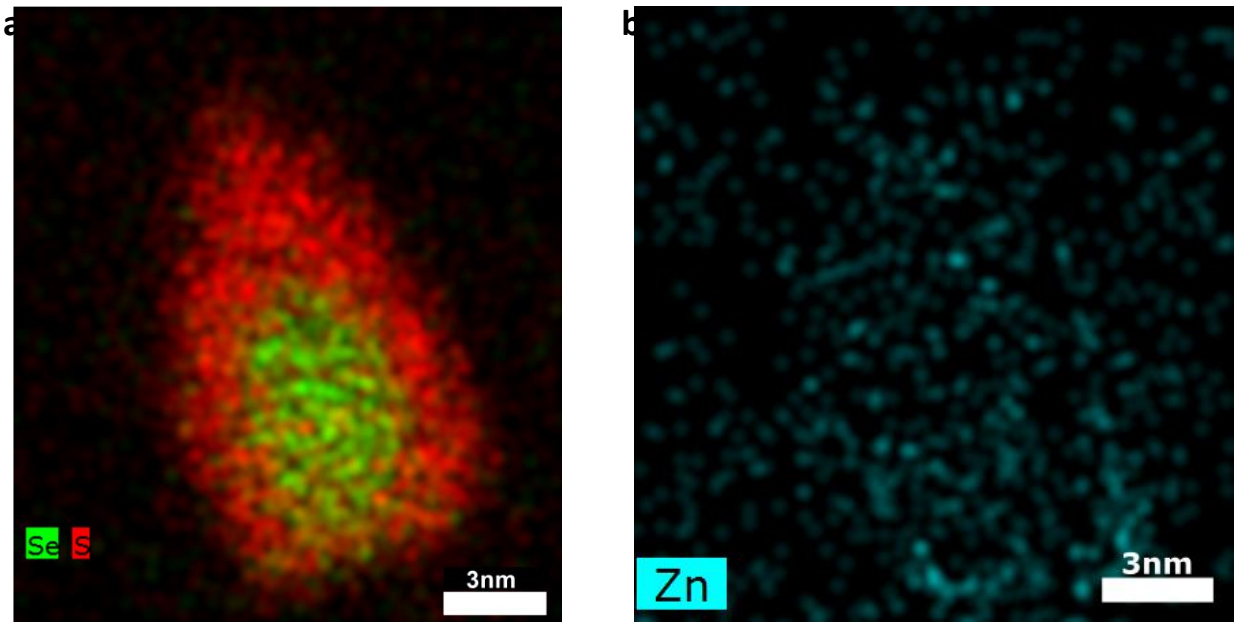

Figure A.14: Elemental maps of ThermoFisher Scientific Qdot 655ITK carboxyl quantum dots. A) Overlay of selenium and sulfur maps to demonstrate the structure of the shell layer. Shortest portion of the shell was measured as 1.18 nm ± 0.37 nm (N=63 measurements). B) Map of zinc in 655ITK dots. The distribution of zinc appears to be shot noise. Shell measurements were performed using ImageJ.

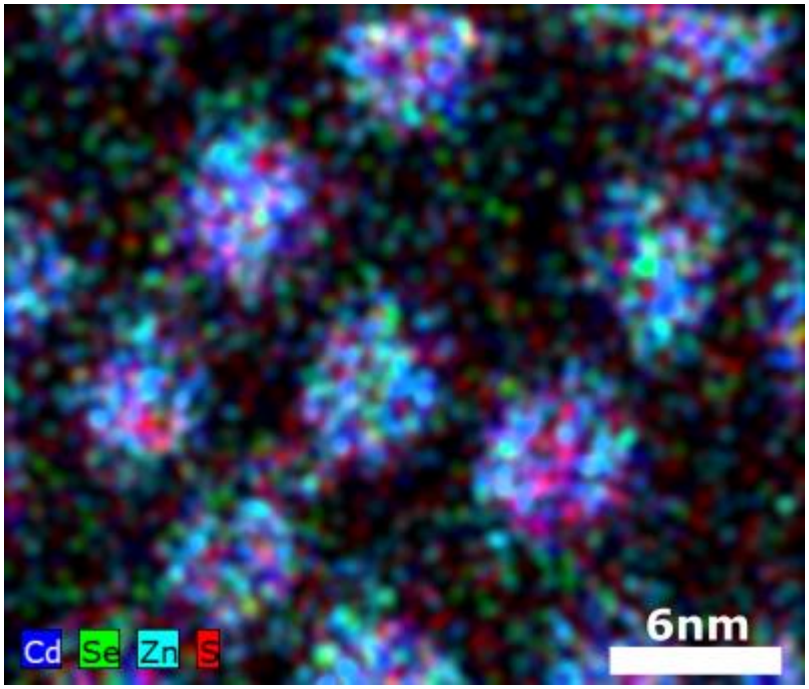

Figure A.15: Elemental maps of the 545ITK Qdots. There is a decided lack of a core structure. The dot sizes determined from this was 5.02 nm ± 0.65 nm (sample size 10 dots) measured using ImageJ.

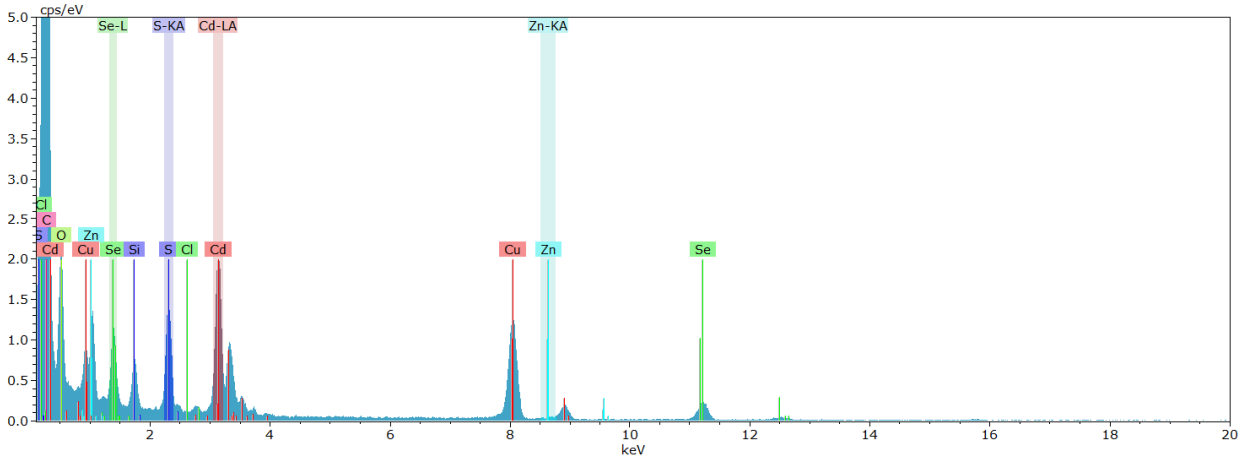

Figure A.16: Quantitative EDS analysis of red emitting QDs. Relative atomic percentages for elements of interest: cadmium 50.90 at.%, selenium 14.27 at.%, sulfur 34.08 at.%, and zinc 0.75 at.%.

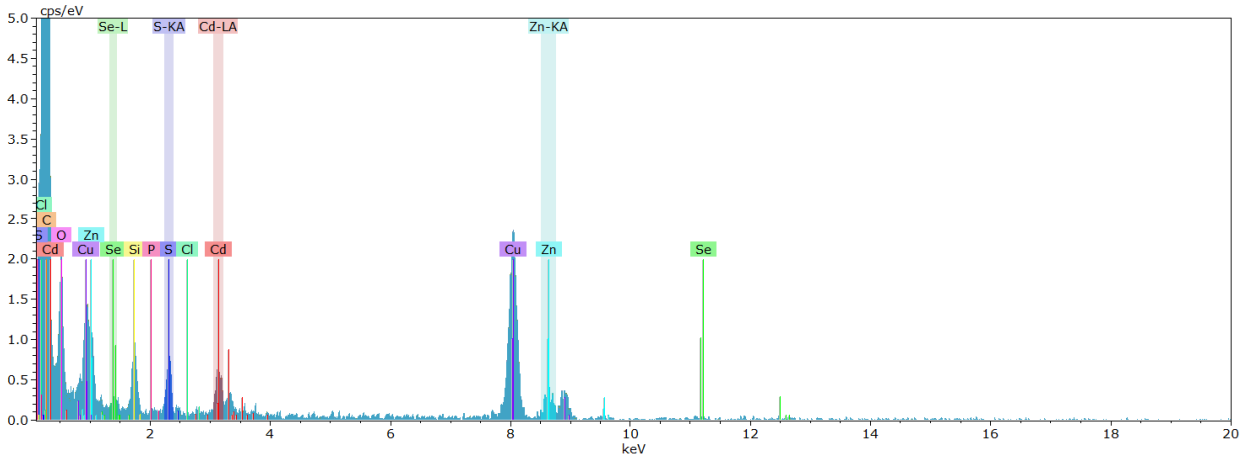

Figure A.17:Quantitative EDS analysis of green emitting QDs. Relative atomic percentages for elements of interest: cadmium 32.76 at.%, selenium 6.47 at.%, sulfur 33.01 at.%, and zinc 27.76 at.%.

A7. Dynamic Light Scattering

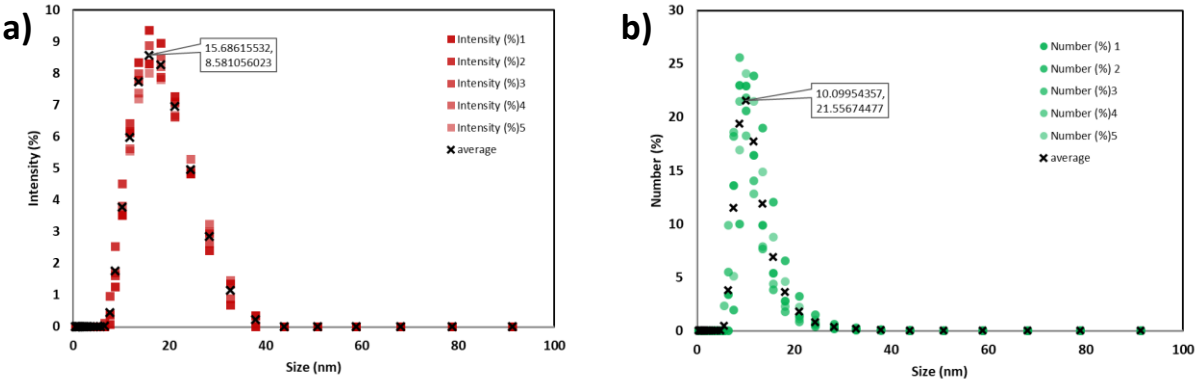

Figure A.18: Size distribution solved via dynamic light scattering of a) red emitting and b) green emitting QDs. Top number is approximated as the average particle size (nm), bottom number describes the size distribution.

Dynamic Light Scattering was employed to find the hydrodynamic radii of the QDs. The quantum dots were quenched with a minimal quantity of $[Co(ClMeN_3S_3sar)]Cl_3$ as the laser in the instrument was within the absorption region of the 655ITKs. The dynamic light scattering profile was run 5 times and averaged. The most reasonable solution for the 655ITKs was found from the intensity%. The 545ITKs had a reasonable solution for number%. Subtraction of size of the inorganic component (as measured by TEM) gave the dimensions of the of the organic portion of the QD shell.

Red emitting QDs:

- Size of total inorganic component (STEM) = 8.7 x15.18 nm
- Core (STEM) = 6.0 x 4.5 nm
- Inorganic shell thickness (thinnest point, STEM) = 1.18 nm ± 0.37 nm
- Hydrodynamic Radius (DLS) = (15.68 nm)
- Organic shell thickness ((Hydrodynamic radius – average inorganic diameter)/2) = [15.68 nm – (8.7 + 15.18 nm/2)]/2) = 1.87 nm

Green Emitting QDs:

- Size of total inorganic component (STEM) =4.59 nm x 0.65 nm
- Hydrodynamic Radius (DLS) = (10.10 nm)
- Organic shell thickness ((Hydrodynamic radius – inorganic diameter)/2) = [10.10 nm – 4.59 nm nm]/2) = 2.8 nm

A8. Tunnelling Dampening Scaling Factors

Between the organic layer thickness provided by DLS, and the STEM mapping of the inorganic portion, a determination of the tunneling barrier dampening coefficient was possible to approximate using

$$-\beta d\ (total) = -\left(\beta_{organic}\ d_{organic}\ +\ \beta_{inorganic}\ d_{inorganic}\right)$$

For the red emitting 655ITK QDs (CdSe@CdS), the CdS shell was measured to be a minimum of 11.8Å and the organic layer 18.7Å. It is understood that the β coefficient for CdS is 0.24 $Å^{-1}$ and for saturated hydrocarbon chains 0.20 $Å^{-1}$. This would yield a total dampening of 6.5. For the green emitting 545ITK dots (ZnCdSeS alloy dots) were determined to have an organic layer of 28Å. This yields a total dampening coefficient of 6.72.

The expression for scaling the electron transfer due to differing tunnelling rates takes the form of:

$$\mathrm{k_{tunneling}} = \mathrm{k_o e}^{-\beta d\ (otal)}$$

The green dots have a higher dampening of the tunneling rate over the red dots mostly because of the thick ligand shell. This indicates that the undampened rate from the green QDs is significantly higher than the rates measured.

A9. Red and Green Dot Comparisons

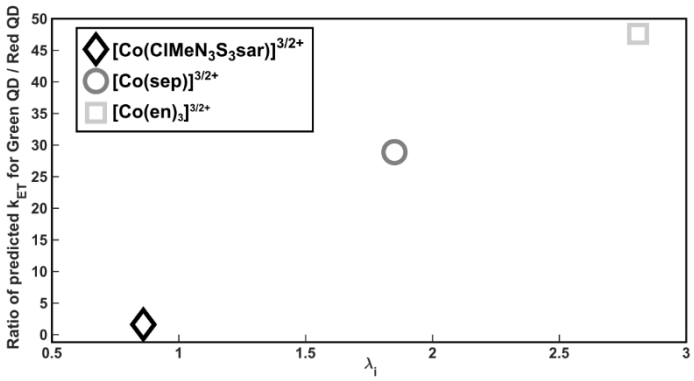

Figure A.19:Comparison of the ratios of the predicted electron transfer rates of the Green QDs/ Red QDs to three cobalt complexes with different internal reorganization energy (li). The ratio improvement in rate from shifts in driving force (red to green) should theoretically be the least for $[Co(ClMeN_3S_3Sar)]^{3/2+}$

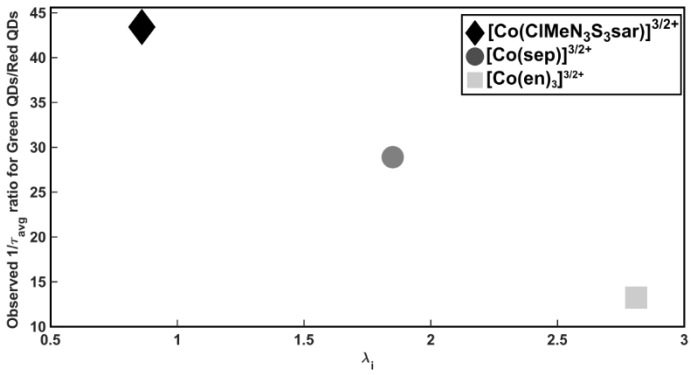

Figure A.20: Comparison of the ratios of the measured fluorescence rates of the Green QDs/ Red QDs in the presence of three cobalt complexes with different internal reorganization energy (l_i). The measured rates were scaled by the calculated tunnelling dampening factors for the two colors of dots. Unlike the predictions above, the ratio improvement in rate from shifts in driving force (red to green) was the largest for $[Co(ClMeN_3S_3Sar)]^{3/2+}$. Marcus inverted behavior was not observed, and Auger Assisted Charge transfer allows the charge transfer from green QDs to $[Co(ClMeN_3S_3Sar)]^{3/2+}$ to outperform Marcus model expectations.

B. Supporting Information from Chapter 4

B1. The Stoichiometric Ratio of Sulfur to Iron vs. Photovoltage

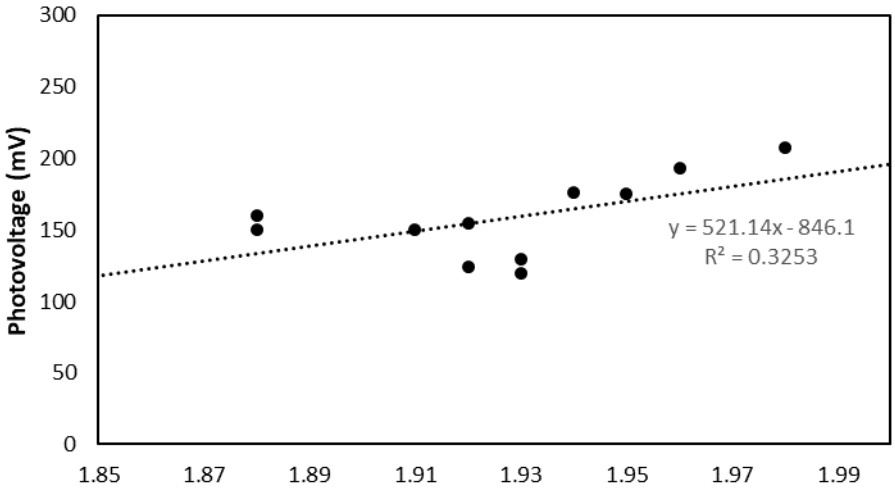

Figure B.21: The stoichiometric ratio of sulfur to iron in samples made by reference [142] and produced photovoltage. There is a minor trend visible, although not distinctive. It is unclear what role dopant atoms had.

C. Supporting Information from Chapter 5

C1. TEM

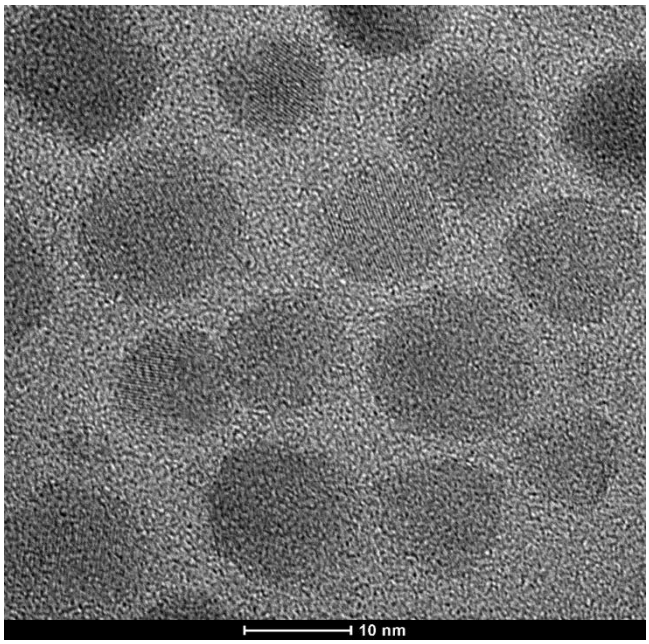

Figure C.1: post treatment small particles visible in Figure 5.4

C2. NMR

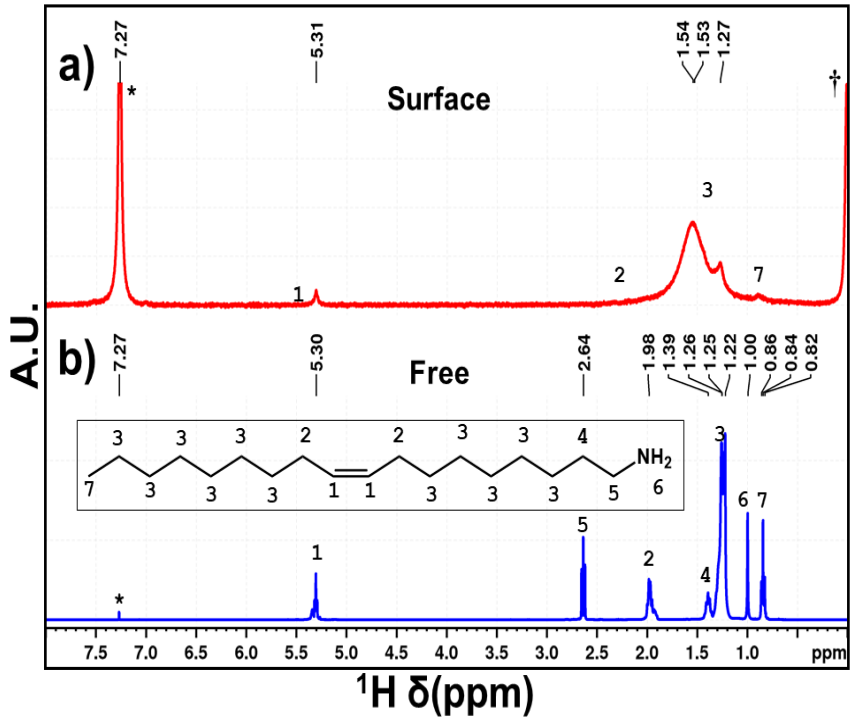

Figure C.22: ^{1}H NMR shifts of oleylamine a) bound to the surface of a pyrite nanoparticle and b) free oleylamine. a) ^{1}H (600MHz, $CDCl_3$): δ 0.88, 1.27, 1.53, 1.54, 5.31 b) ^{1}H (600MHz, $CDCl_3$): δ 0.84, 1.00, 1.25, 1.98, 2.64, 5.30. Peak with * is chloroform solvent.

C3. In Situ XRD Refinements

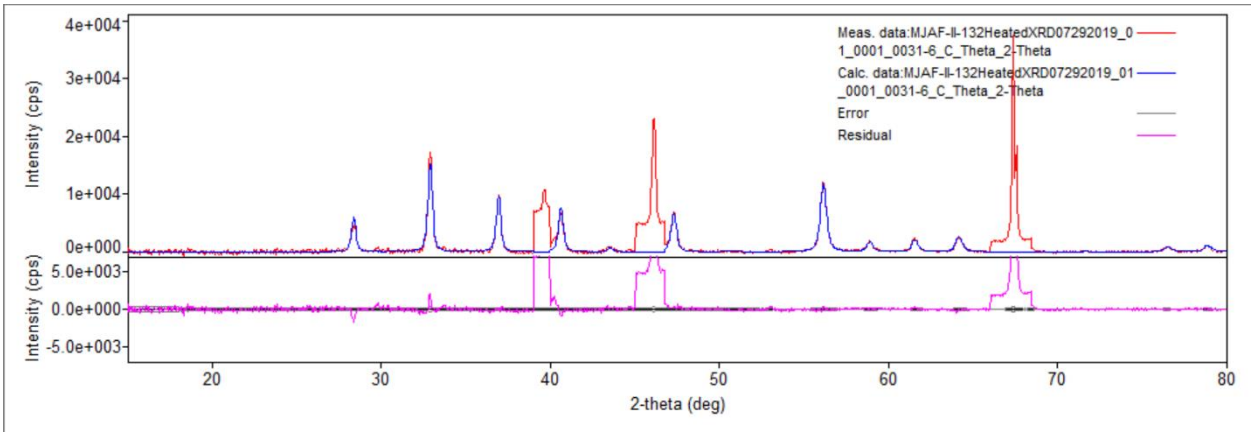

Figure C.3: Refinement and residuals of heated in situ XRD at 30°C. Rwp=3.19%, Rp=2.11%, Re=2.13%, S=1.4897, χ^2=2.2192.

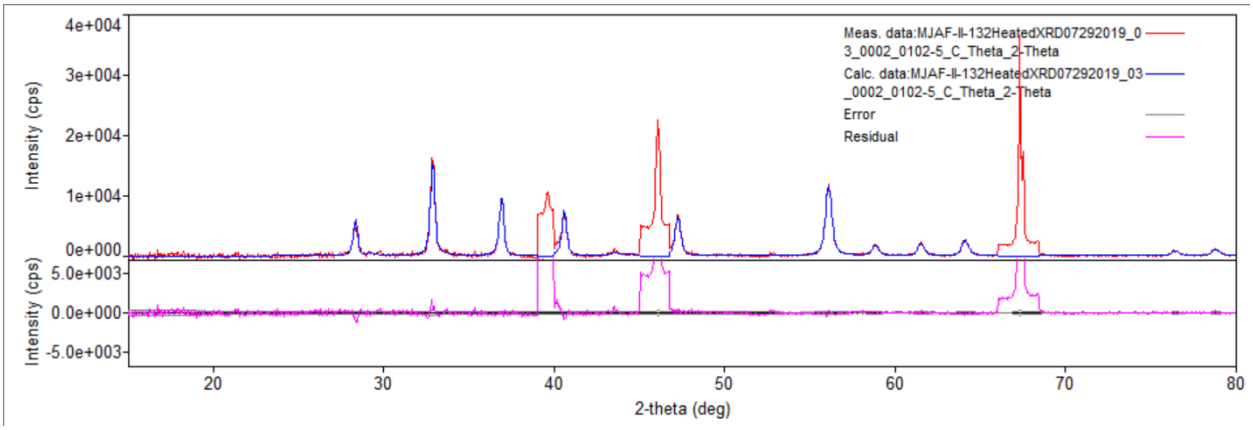

Figure C.23: Refinement and residuals of heated in situ XRD at 102°C. Rwp=3.08%, Rp=2.12%, Re=2.13%, S=1.4414, χ^2=2.0777.

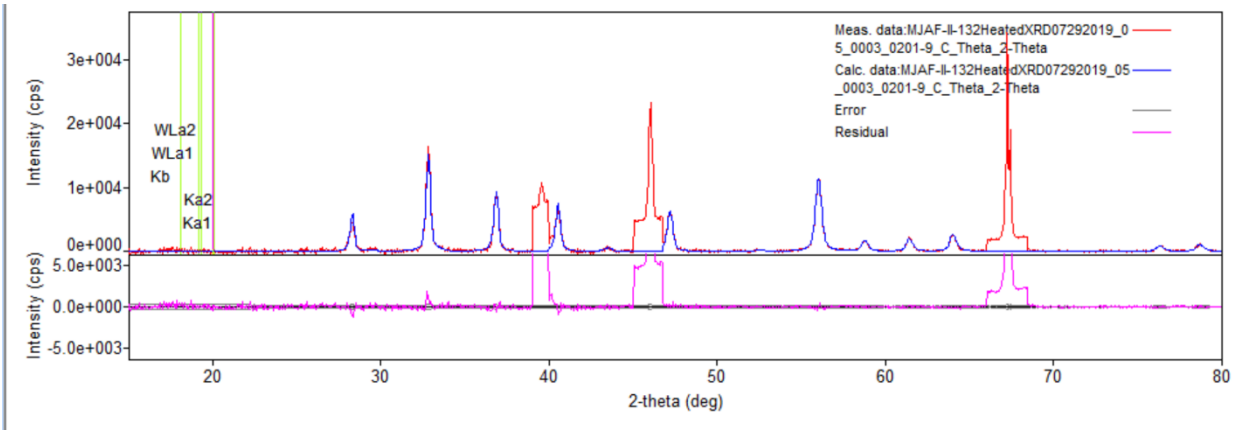

Figure C.5: Refinement and residuals of heated in situ XRD at 200°C. Rwp=2.78%, Rp=1.92%, Re=2.13%, S=1.3002, χ^2=1.6904.

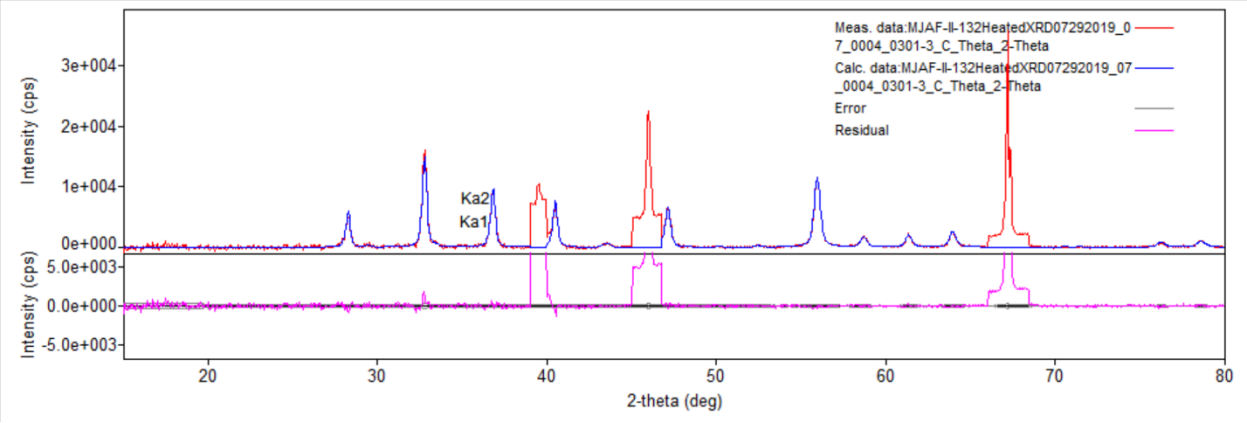

Figure C.6: Refinement and residuals of heated in situ XRD at 300°C. Rwp=2.70%, Rp=1.87%, Re=2.13%, S=1.2644, χ^2=1.5988.

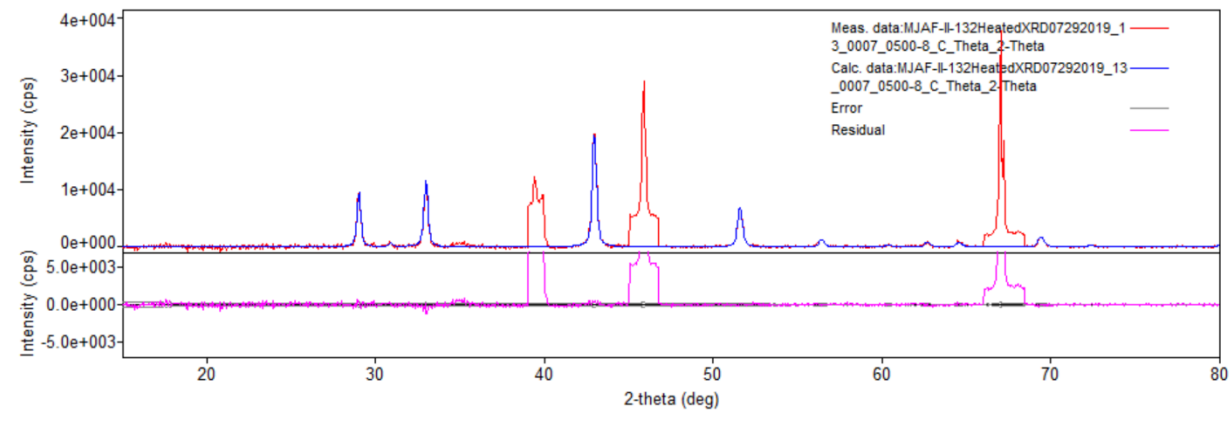

Figure C.7: Refinement and residuals of heated in situ XRD at 500°C. Rwp=2.76%, Rp=1.88%, Re=2.11%, S=1.3019, χ^2=1.6948.

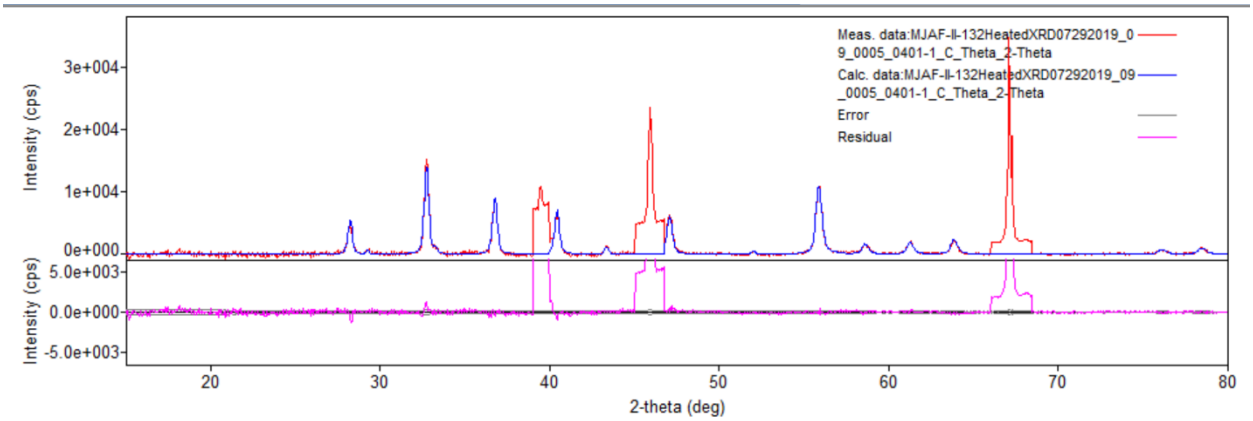

Figure C.8: Refinement and residuals of heated in situ XRD at 400°C. Rwp=2.91%, Rp=1.98%, Re=2.13%, S=1.3603, χ^2=1.8504.

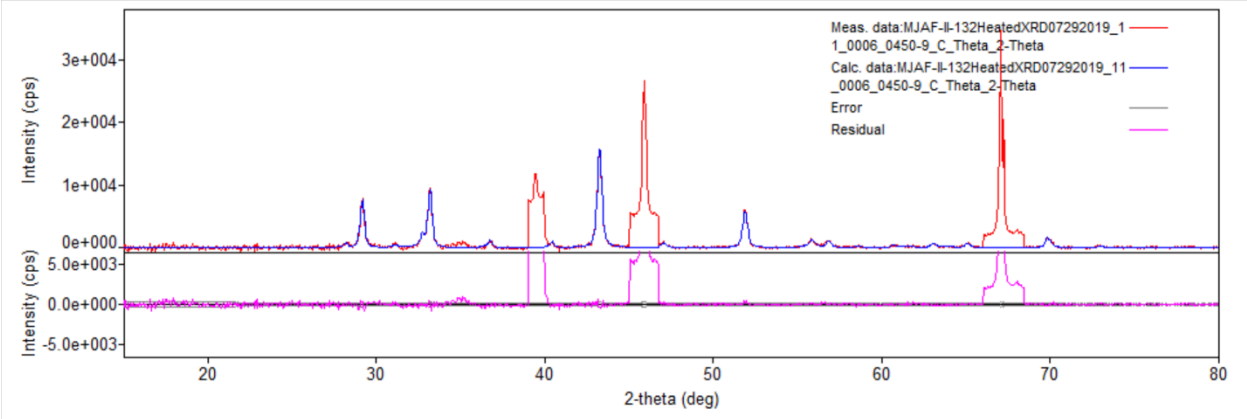

Figure C.9: Refinement and residuals of heated in situ XRD at 450°C. Rwp=2.66%, Rp=1.88%, Re=2.21%, S=1.2548, χ^2=1.5745.

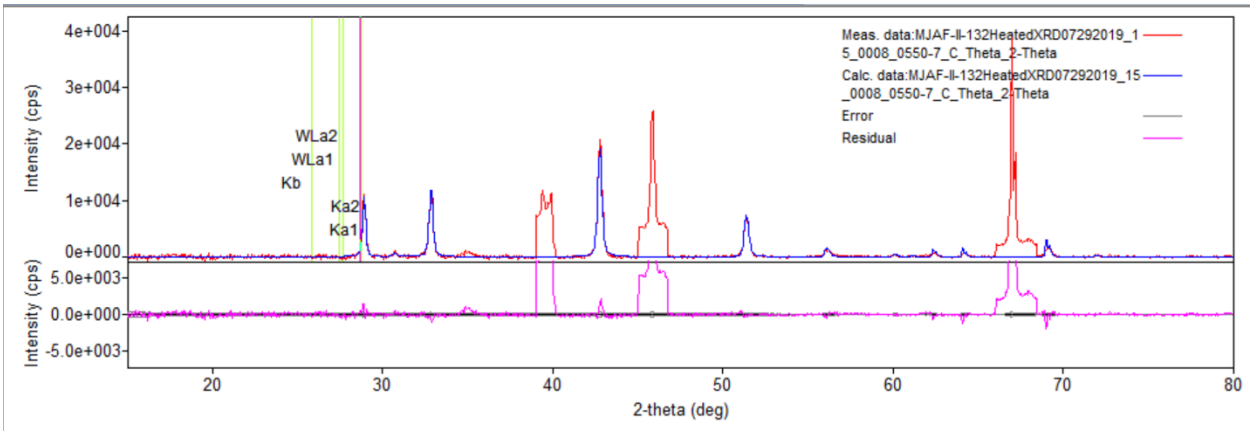

Figure C.10: Refinement and residuals of heated in situ XRD at 550°C. Rwp=4.03%, Rp=2.24%, Re=2.21%, S=1.8978, χ^2=3.6015.

C4. XPS

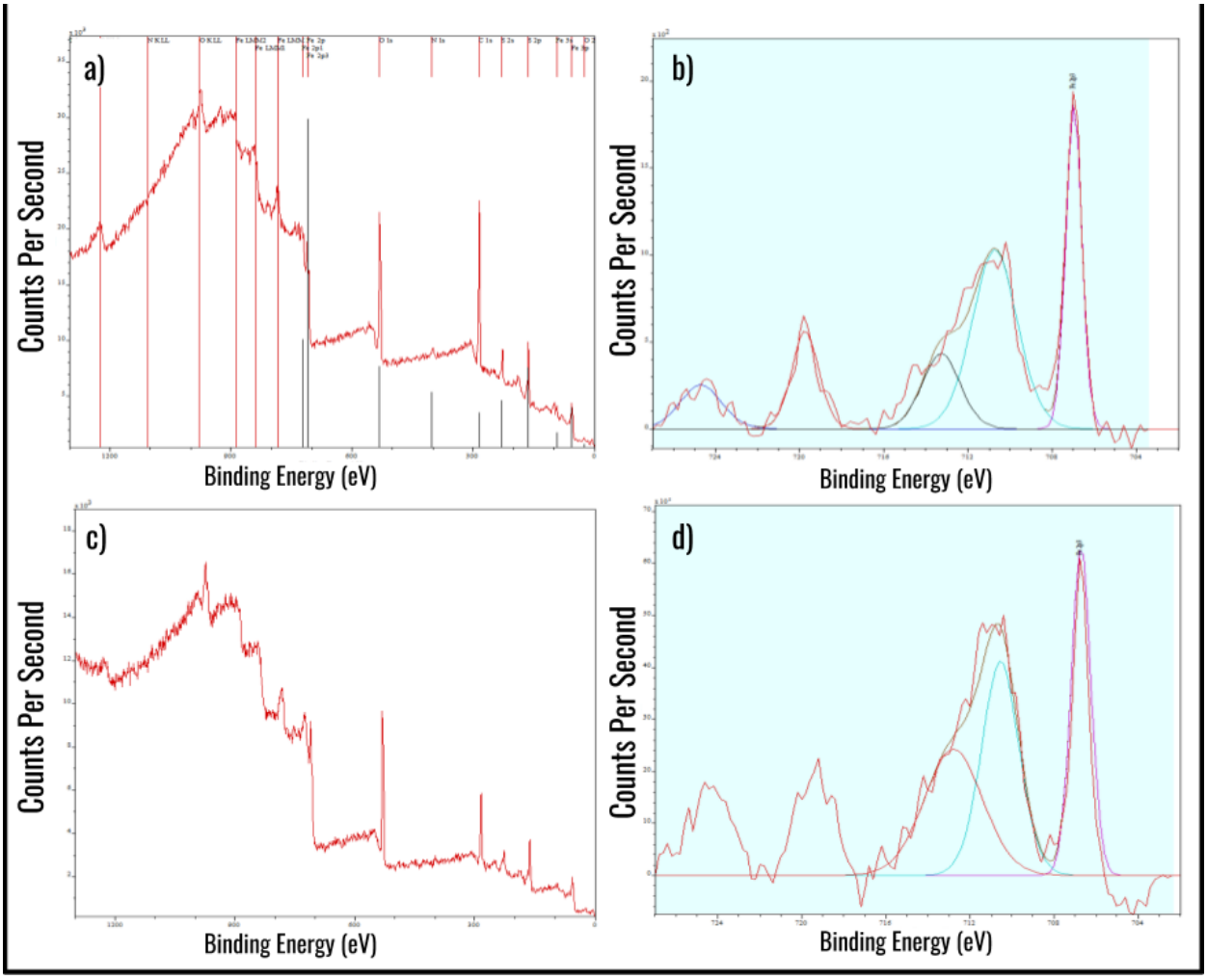

Figure C.11: XPS of pyrite nanoparticles. A) the general survey of the pyrite sample with only native ligands present. B) native ligands with the iron 2p3 peak examined separately. C)treated particles general survey. D) treated particles iron 2p3 peak. The increase of the magnitude of the peak at 712eV is indicative of more iron(III) in the sample.

C5. XRD

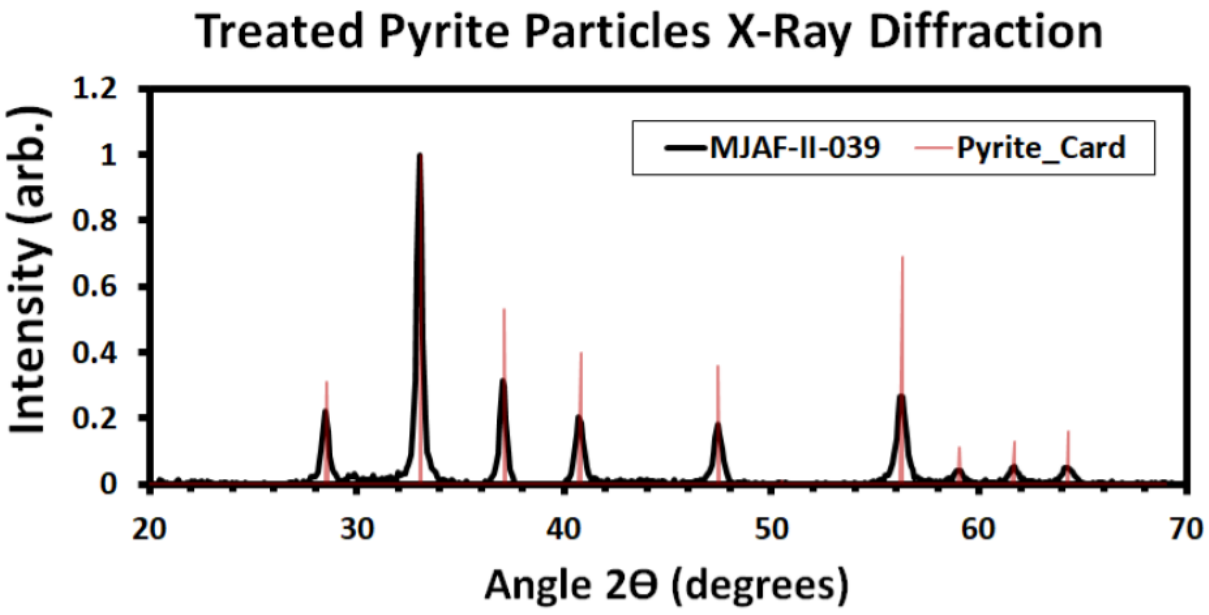

Figure C.12: X-ray diffraction of treated particles. JCPDS-PDF #42-1340